Hydrogenation of monolayer graphene in the diamond anvil cell and supercritical phenomena in methane

Dean Smith

School of Computing, Science & Engineering
College of Science & Technology
University of Salford, Salford, UK

A thesis submitted in partial fulfilment of the requirements of the degree of doctor of philosophy, January 2016

In loving memory of Barbara Smith

Table of contents

List of figures

Acknowledgements

First and foremost, I would like to express my gratitude to my supervisor, John Proctor, for the opportunity to partake in three years of exciting and challenging experiments. John was kind enough to include me in the move from University of Hull to University of Salford, a move which has benefited me both professionally and personally.

Diamond anvil cells used throughout this thesis are the product of the expert craftsmanship of Nigel Parkin at University of Hull and Mike Clegg at University of Salford. Graphene samples used throughout this thesis were manufactured and provided to us by Yong-Jin Kim and Kostya Novoselov at University of Manchester.

All of the staff at the University of Hull Physics & Mathematics department and in the Physics department of the University of Salford. For making my move from Hull to Salford seamless, Ian Morrison, and for making it enjoyable and welcoming, Iain Crowe and Matthew Halsall at University of Manchester's Photon Science Institute.

The work presented in this thesis would not have been possible without the generosity of Ross Howie and Eugene Gregoryanz at the Centre for Science at Extreme Conditions, University of Edinburgh, Vladimir Vishnyakov of University at Huddersfield, Chris Muryn at University of Manchester and Paraskevas Parisiades at the ID27 beamline, ESRF.

My PhD peers, and those that I have had the pleasure of sharing workspaces with: Nick Appleyard, Slobodan Čičić, Anthony Edwards, Mark Lundie, Addison Marshall, Alex Marshall, Jacek Miłoszewski, Beth Newton, Jonny Saul, Cristina Simionescu, Simon Steele, Tom Walsh and my ever-dependable friends, Joseph Medlam, Daniel Naylor, Jed Salisbury and Stanley Yau.

Everybody at the University of Hull Ice Hogs and Universities of Manchester Metrostars ice hockey clubs.

And, of course, the family who have loved and supported me throughout the past three years in research and twenty-five years in life: Mam, Dad and Lee.

Declaration

This thesis has been written in full by Dean Smith (the author) and contains only experimental work that has been performed by the author, with the necessary assistance of Dr John Proctor and those collaborators thanked on page xii. The thesis has been prepared in full by the author, with proof-reading provided by Dr John Proctor.

The nature of experiments presented in Chapter 6 is such that not all data may have been directly collected by the author, X-ray diffraction experiments were performed as part of a group over a number of days using a shift system at the European Synchrotron Radiation Facility. The experiment detailed in § 6.3.1 was performed by Daniel Eden under the supervision of and with the assistance of the author. The analyses of all data presented in this thesis was performed explicitly by the author, including those in § 6.3.1.

Experiments detailed in Chapter 5 of this thesis have been published by the author: D Smith *et al.*, "Hydrogenation of Graphene by Reaction at High Pressure and High Temperature", *ACS Nano* **9**, 8279 (2015).

Abstract

Functionalisation with hydrogen could allow exploitation of the remarkable electronic properties of graphene by creating tuneable electronic band gaps as well as offering access to its incredibly high surface area-to-volume ratio for uses in advanced materials by opening pathways to conventional organic chemistry on the material. While partially-hydrogenated graphene is regularly produced and its properties studied, the current methods of producing the material – which typically employ bombarding graphene with atomised hydrogen – have not yet shown the potential to synthesise fully-hydrogenated graphene, termed *graphane*.

This thesis describes an alternative method of hydrogenating graphene by heating the material in an atmosphere of molecular hydrogen under high pressure (2.6 – 6.5 GPa) in a diamond anvil cell. The hydrogen content of functionalised samples can be estimated by observing the Raman spectrum and such analysis suggests that the diamond anvil cell method currently hydrogenates samples to an extent that is competitive with existing methods. By tailoring the sample architecture to allow hydrogen direct access to both sides of a graphene crystal, it is feasible that the diamond anvil cell method of hydrogenation could be used to synthesise the first graphane crystal.

Also presented in this thesis is a series of experiments probing methane in the supercritical region of its pressure-temperature phase diagram, combining Raman spectroscopy and direct structural measurements through X-ray diffraction. At 298K, we observe discontinuous changes in the vibrational Raman spectrum of methane which are not accompanied by a change in density. This phenomena may be explained by a crossing of the recently-theorised *Frenkel line* or by critical point proximity effects described by Widom in the 1960s. The Raman discontinuity is not observed at 523 K, suggesting that alternative methods must be employed to conclusively determine the presence (or absence) of the Frenkel line.

Chapter 1. Introduction

1.1. Hydrogenation of graphene

The recent discovery of graphene – a single layer of hexagonally(sp^2)-bonded carbon atoms forming a large two-dimensional crystal – has attracted interest in the material both in the lab for its insight into fundamental quantum mechanics (Novoselov 2007, Nair 2008, Dean 2013) and in industry for its remarkable electronic and mechanical properties (Novoselov 2012, Lee 2008). The impact of graphene on 21st century science is put into perspective by the awarding of the Nobel Prize in Physics to Kostya Novoselov and Andre Geim in 2010 for its discovery and by the announcement of the G*raphene Flagship* project to fund development of the material for science and technology, worth €1billion in funding directly from the European Union, in 2013 – both accolades occurring within a decade of the first measurements on the material in 2004 (Novoselov 2004).

Graphene can be considered a basic building block for graphitic materials of all dimensionalities. From Figure 1.1, we can see that two-dimensional graphene sheets can be rolled to form one-dimensional carbon nanotubes or zero-dimensional buckminsterfullerene molecules, or they can be stacked to create three-dimensional graphite (Geim 2007). It is also expected to react with hydrogen to form hexagonally-bonded monolayers of sp^3 carbon, or *graphane*.

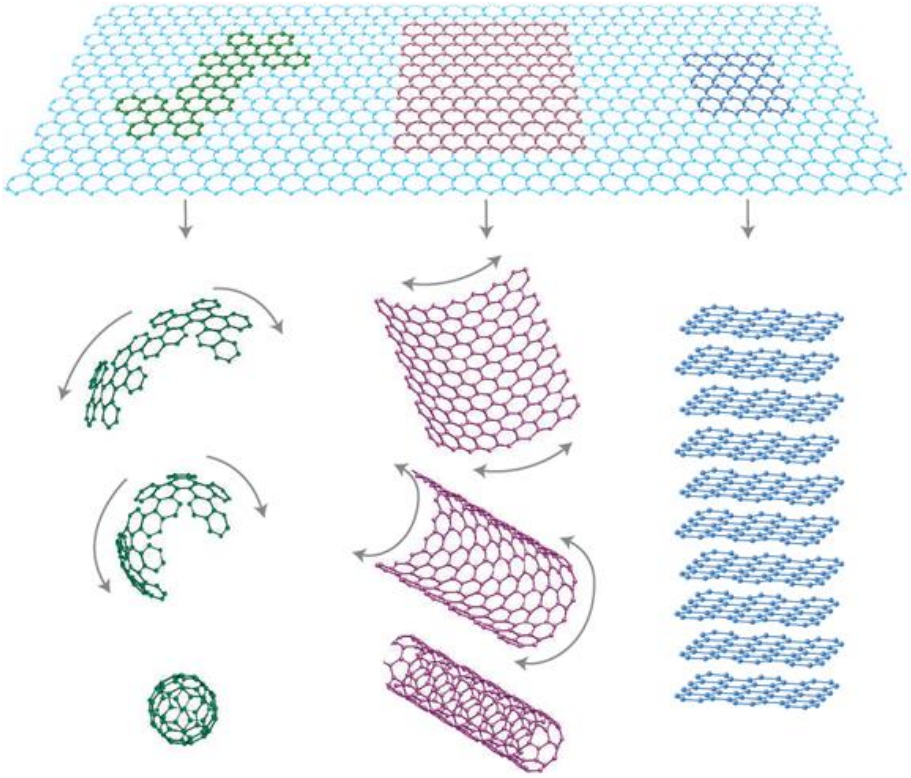

Figure 1.1: Graphene is a building block for carbon materials, it can be rolled into buckminsterfullerene molecules or carbon nanotubes, or it can be stacked to create graphite (Geim 2007).

In order to modify its band structure, graphene has been partially hydrogenated (Elias 2009). Hydrogenated graphene becomes insulating at high hydrogen coverage, but the size of its band gap can be tailored by controlling the levels of hydrogenation (Balog 2010), demonstrating how the material could be useful for creating circuits directly onto the graphene lattice (Novoselov 2009). In spite of its calculated stability (Sofo 2007), a method to synthesise fully-hydrogenated graphene has not yet been developed, existing methods only achieve low levels of hydrogen coverage.

Half a century prior to the discovery of graphene, high pressure and high temperature conditions were utilised in the enormous heated presses employed by 20th century scientists at General Electric to aid the conversion of planar sp^2 into tetrahedral sp^3 carbon when they successfully synthesised man-made diamond for the first time from graphite seeds (Bovenkerk 1959). More recently, C_{60} molecules and glassy carbon have been converted to nanocrystalline diamond under high pressure (Regueiro 1992, Dubrovinsky 2012). By acknowledging these phenomena, it seems

reasonable to expect that compressing graphene to high pressures under high temperature in the presence of hydrogen should facilitate the conversion of purely sp^2 bonded graphene into its sp^3 bonded counterpart graphane.

The motivation of the work presented in this thesis is to design a method whereby graphene can be reacted with molecular hydrogen in a diamond anvil cell using a combination of high pressure and high temperature to form hydrogenated graphene. Unless stated otherwise, the term *graphene* throughout this thesis refers to pristine, monolayer graphene. Similarly, *graphane* refers only to fully-hydrogenated graphene with stoichiometry CH – *i.e.* a hydrogen atom attached to every carbon atom in the lattice. When discussing partially-hydrogenated graphene, *graphone* is sometimes used in the literature (Kvashin 2014), but *hydrogenated graphene* will be used throughout this thesis.

1.2. The Frenkel line

The accepted understanding of fluids has been challenged in recent years by a new model of liquids (Brazhkin 2012) based on groundwork by Soviet scientist Yakov Frenkel detailed in his textbook, "Kinetic Theory of Liquids" (Frenkel 1946). In particular, the Frenkel-inspired model predicts physical changes between two fluid states beyond the critical point.

Liquids, gases and supercritical fluids are defined on the pressure-temperature phase diagram (Figure 1.2a) through the van der Waals equation of state. In order to account for the potential energy between particles in a gas, 19th century scientist Johannes van der Waals made corrections to the existing ideal gas model, leading to the van der Waals equation of state:

$$\left[P + a\left(\frac{N}{V}\right)^2\right]\left(V - Nb\right) = Nk_{\mathrm{B}}T \qquad 1.1$$

Where N is the number of particles, k_{B} is the Boltzmann constant and a,b are the van der Waals constants, specific to different materials (Baierlein 1999). The van der Waals equation predicts an oscillation in PV isotherms (Figure 1.2b), which

converges with increasing temperature until forming a critical point at some temperature T_C. The oscillations in $T < T_C$ isotherms appear to predict three stable volumes and a negative compressibility over a range of pressures, which are not observed in a real system. Real materials instead follow the coexistence line as a result of corrections by Maxwell (Maxwell 1875), and an isothermal increase in pressure below T_C exhibits a sudden decrease in volume, *i.e.* a first-order phase transition between liquid and gas which forms the boiling line (Figure 1.2b).

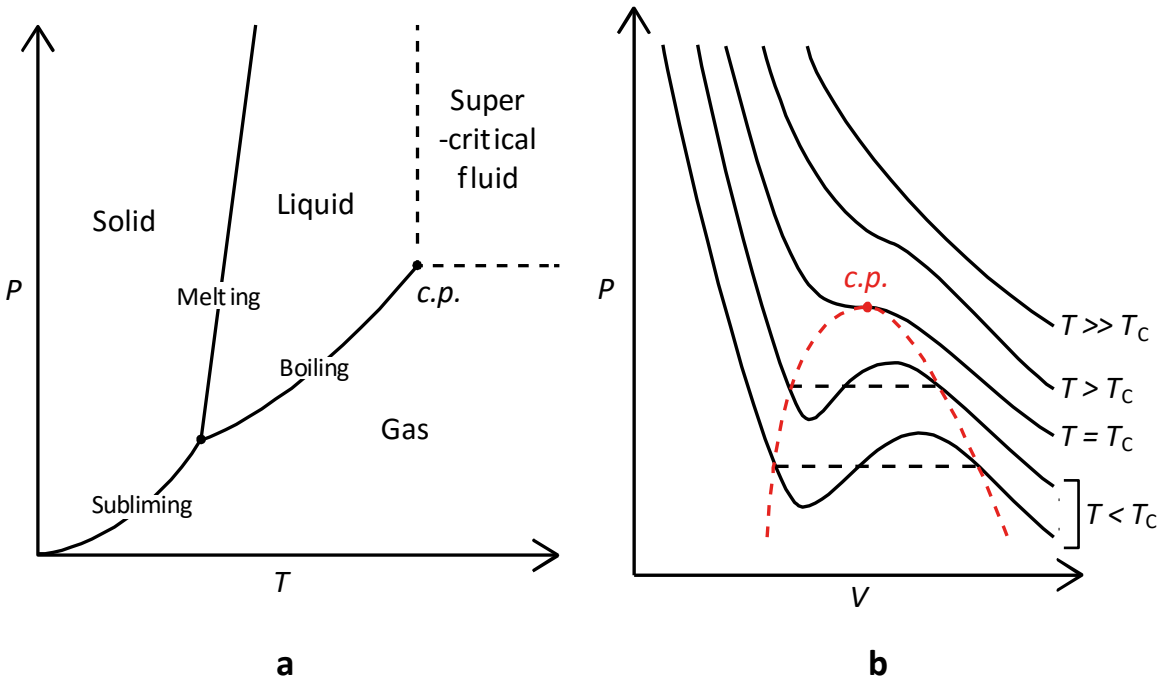

Figure 1.2: (**a**) Example of a pressure-temperature phase diagram, with a critical point *c.p.* (**b**) Isotherms of the van der Waals equation of state. Red dot locates the critical point, red dashed line the spinodal line and black dashed line signifies coexistence between liquid and gas.

Above T_C, the oscillation disappears and no transition between liquid and gas is observed. Here, the material enters the supercritical fluid state, where classically there exists no distinction between liquid and gaseous states. However, the new Frenkel-based model considers particle motion in liquids to be a duality of solid-like and gas-like dynamics (Trachenko 2013), and predicts certain pressure and temperature conditions under which a liquid tends more towards "gas-like" or "solid-like" behaviours, predicting a discontinuous crossover which is termed the *Frenkel line* (Brazhkin 2012).

Supercritical fluids find common use in science and technology. Supercritical methanol provides a catalyst-free method of esterifying vegetable oils into biodiesel for fuel engines (Fukuda 2001), while supercritical water allows pyrolysis of wet biofuels to extract hydrogen more effectively than traditional pyrolysis (Demirbas 2007). Carbon dioxide has a critical temperature close to ambient temperature (Linstrom 2011), opening up the potential for supercritical CO_2 to be used as a solvent in place of conventional chemistry lab solvents, already utilised in pharmaceutical processes (Subramaniam 1997), with a more favourable environmental impact (Beckman 2003). It is also supercritical carbon dioxide which makes up the majority of the atmosphere of our neighbour planet, Venus (Bolmatov 2014). A proper understanding of the supercritical fluid state – or states – is thus important for developing our collective understanding of planetary sciences and potentially useful in refining green technologies.

To describe the two predicted liquid states at either side of the Frenkel line, far beyond the critical point, we adopt the terminologies "solid-like"/"gas-like" or rigid/non-rigid fluid.

1.3. Thesis outline

Including this introductory chapter, this thesis will comprise 7 chapters covering the use of a heated diamond anvil cell in both the initiation of the chemical reaction between graphene and hydrogen and the probing of methane in its supercritical region in search of the Frenkel line.

Chapter 2 will provide an introduction to the properties of graphene which have been determined since its experimental discovery in 2004. In particular, § 2.2 will discuss the increased availability of graphene to researchers and technologists *via* the development of large-scale synthesis methods. § 2.3 will outline the potential uses of graphene derivatives – highlighting important experimental findings made since the discovery of graphene on its derivatives and their properties.

Chapter 3 will discuss Raman spectroscopy and its usefulness in determining structure and bonding in graphene and derivatives. §§ 3.2 and 3.3 in particular hope

to give a detailed overview of how changes in the Raman spectrum of the material can be used to qualitatively judge changes due to functionalisation and begin to quantify the content of adatoms.

An introduction to experimental techniques at high pressure and high temperature in a diamond anvil cell will be provided in Chapter 4. In particular, issues with measuring pressure at relatively low diamond anvil pressure and elevated temperatures using popular methods will be addressed and alternatives suggested in § 4.2.

Results from experiments on graphene and hydrogen at high pressure and high temperature will be presented in Chapter 5, detailing a proof of concept that hydrogenated graphene will form readily from graphene and molecular hydrogen at sufficient pressure and temperature and exploring the extent and rate of the reaction at various pressure-temperature combinations and the stability of the hydrogenated graphene samples produced.

The results of high pressure experiments performed on supercritical methane will be presented in Chapter 6, following an introduction to the microscopic model behind the Frenkel line and its macroscopic predictions in § 6.1 and a brief discussion of the fluid X-ray diffraction capabilities of the European Synchrotron Radiation Facility in § 6.2.

Chapter 7 will provide an overview of the conclusions that can be drawn from experiments on graphene under compression in hydrogen (§ 7.1) and discuss the necessary steps to be taken in order to further understand hydrogenated graphene samples prepared by this method and extend the hydrogen content towards synthesis of graphane. In § 7.2, the presented results of compression of methane above its critical temperature will be discussed and experiments proposed which could provide confirmation or contradiction of the Frenkel line theory.

Chapter 2. Synthesis of graphene and functionalised graphene

2.1. Realisation of graphene

The graphite structure comprising stacked sheets of flat, hexagonally-bonded carbon has been known since the early 20th century (Bernal 1924), and models of the electronic structure of an individual layer of graphite have been formulated since the 1940s (Wallace 1947, McClure 1957). In his derivation of the band structure of graphene, P R Wallace predicted that a single layer of graphite has semimetallic properties, with a linear dispersion relation close to the Fermi level that varies according to $\boldsymbol{E} \approx v_{\mathrm{F}}\boldsymbol{k}$. Here, v_{F} is the *Fermi velocity* ($v_{\mathrm{F}} \approx 10^6$ ms^{-1}) which is independent of energy and momentum – *i.e.* it acts as a "speed of light" for charge carriers in graphene (Wallace 1947, Castro Neto 2009).

Single planes of graphitic carbon were successfully isolated from graphite by Novoselov and Geim in 2004 (Novoselov 2004) and given the name *graphene*, following naming conventions from organic chemistry (Boehm 1986). Novoselov *et al.* experimentally observed the semimetal or zero band-gap semiconductor nature of single- and few-layer graphene that had been predicted by Wallace and subsequent models (Castro Neto 2009) for the first time (Novoselov 2004). The group went on to confirm that charge carriers in graphene behave as *massless Dirac fermions*, such that their energy is proportional to their momentum as predicted, and made empirical measurements of the Fermi velocity (Novoselov 2005). The massless nature of its electrons and the chemical and physical stability of graphene – that allow it resistance

against defects – can result in ballistic carrier transport over distances up to 1 µm (Castro Neto 2009).

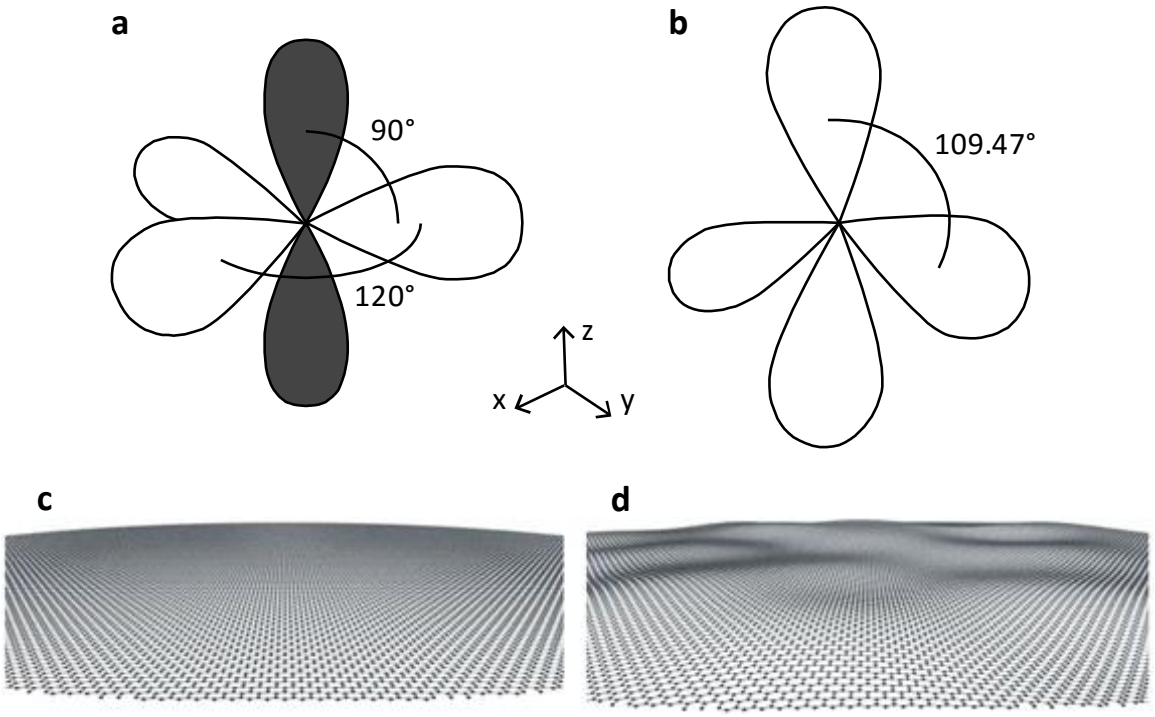

Figure 2.1: (**a**) sp^2 hybridised molecular orbitals, grey shaded orbitals are the unhybridised p_z orbitals. (**b**) sp^3 hybridised molecular orbitals. (**c**,**d**) Visualisations of ideal and real graphene landscapes. The nano- and microscopic corrugation of the graphene sheet allows freestanding regions to be stable even when samples are only partially supported by a substrate (Meyer 2007).

Figure 2.1 shows two hybridised atomic orbitals which the electrons in carbon commonly occupy when forming bonds in organic molecules or in bulk carbon. sp^2 orbitals are formed by a combination of the 2*s* and two of the 2*p* atomic orbitals (nominally $2p_x$ and $2p_y$), leaving the third *p* orbital ($2p_z$) unchanged (grey orbital in Figure 2.1a) – resulting in a set of three sp^2 orbitals forming a plane. Through overlapping of sp^2 hybridised orbitals, carbon atoms form σ bonds to form hexagonal or pentagonal aromatic rings, as in the molecule benzene or its two-dimensional polymer graphene, while the overlapping of the p_z orbitals creates a weaker π bond. In sp^3 hybridisation, all of the 2*p* orbitals are hybridised, resulting in a tetrahedral distribution of orbitals which is seen in the bonding of methane molecule or the crystal structure of diamond.

Atomic-scale observations made on graphene deposited onto silicon dioxide substrates using scanning tunnelling microscopy (STM) (Ishigami 2007) and on quasi-freestanding graphene using transmission electron microscopy (TEM) coupled with electron diffraction measurements (Meyer 2007) showed that samples feature long-range, smooth ripples. It is suggested that these ripples are an integral component of the crystal structure of graphene which allow it stability in spite of its atomic thickness (Fasolino 2007, Meyer 2007). Due to rippling effects in graphene (Figure 2.1d), it is convenient to consider the bonding of the material not as pure sp^2, but to comprise a very small sp^3 contribution. This can be written shorthand as $sp^{2+\eta}$ ($0 \leq \eta \leq 1$), where η represents the degree of curvature. This is seen already in carbon nanotubes or buckminsterfullerene molecules, which can be thought of as graphene "rolled up" (Figure 1.1) (Saito 2004).

Mechanically, the Young's modulus of graphene places it alongside other carbon allotropes such as graphite and carbon nanotubes as one of the strongest materials measured (Lee 2008), which has spurred research into graphene-based composite materials that benefit from the mechanical strength of monolayer graphene and nanographite (Potts 2011). Graphene has been subject to tensile uniaxial strain (Mohiuddin 2009), compressive biaxial strain in a diamond anvil cell (Proctor 2009, Filintoglou 2013) and both tensile and compressive biaxial strain on a soft substrate (Ding 2010), with all experiments in agreement that the Grüneisen parameters defining the frequency of Raman-active phonon modes in relation to lattice volume of graphene – and thus its elastic properties – closely resemble those for graphite.

The unique ballistic electronic transport properties of graphene make it a highly attractive replacement for current electronic materials such as silicon, and when coupled with its optical transparency a desirable alternative to the fragile and expensive indium tin oxide which had previously dominated research into next-generation photovoltaics (Mattevi 2010). A complete review of the potential uses of graphene that are currently being explored is not within the scope of this thesis, the most recent "roadmap" for graphene spans over 200 pages and features contributions from 64 authors from around the globe (Ferrari 2015), and discusses the need for a controllable band gap in graphene to properly access its electronic capabilities. At present band gaps in graphene are commonly opened by synthesising graphene

nanoribbons (Bai 2010), where the gap size can be tailored according to the width of the nanoribbon (Han 2007), but there is interest in controlled functionalisation as a method of opening tailored band gaps (Balog 2010, Haberer 2010).

2.2. Synthesis of graphene

The samples produced by Novoselov *et al.* for the first ever study of graphene were produced using repeated mechanical separation of high-quality graphite samples using adhesive tape and deposition onto a silicon substrate with a 300 nm silicon dioxide layer (Novoselov 2004 and supplementary information) – a process that has come to be known as *micromechanical cleavage* or the "scotch tape method". This substrate choice is important as it allows thin graphite, few-layer or monolayer graphene samples to be identified though optical microscopy though interference colour changes caused by the reflection through the transparent SiO_2 layer (Novoselov 2005).

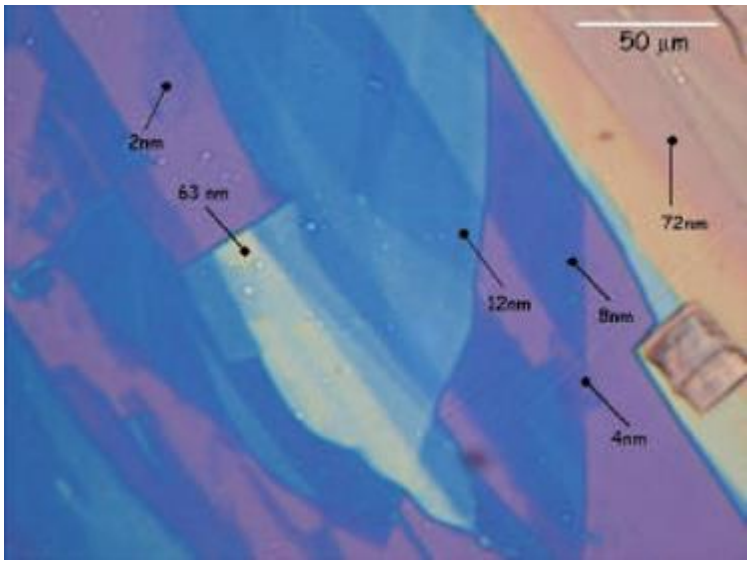

Figure 2.2: Interference colour changes in reflected light from a Si-(300 nm)SiO_2 surface due to mechanically-cleaved graphite and graphene. Yellow regions show thicker graphite, while pale purple regions (top left) show thinner graphene (Novoselov 2004, supplementary information).

Figure 2.2 shows thin graphitic carbon deposited on a Si-SiO_2 substrate using the scotch tape method and the effects of thickness on their colour. Optical microscopy can be supplemented with Raman spectroscopy measurements on thin regions to confirm monolayers. A discussion of the Raman spectrum of graphene and its changes with increasing layer number can be found in § 3.2. Since the first isolation of graphene *via* this method, significant advances have been made in the production of large-scale, high-quality monolayer graphene samples. While micromechanical cleavage is still a viable and utilised option to produce high-quality graphene (Ansell 2015), other synthesis methods are now viable.

Epitaxial growth on silicon carbide has been implemented for growing thin graphite for decades (Berger 2004, de Heer 2007). Physically, the process occurs as the silicon in SiC sublimes at high temperature, and the remaining carbon is annealed into sp^2 layers ("graphitisation", see Figure 2.6, § 2.3). Whilst growing graphene on the carbon face of SiC and increasing the number of layers grown can see improvements in the electronic properties (de Heer 2007, Mattevi 2011), the structural quality of epitaxially-grown graphene as determined by Raman spectroscopy (§§ 3.2 and 3.3) does not match mechanically-cleaved graphene, especially after transfer to a different substrate (Ni 2008, Ferralis 2010).

Synthesis techniques are still hotly researched (Geng 2015) in hopes of reproducibly creating large-scale single crystals of monolayer graphene and improving batch processing of polycrystalline graphene. Existing methods include growth on metal surfaces by segregation of carbon atoms from a metallic host and the graphitisation at high temperatures on the wafer-scale (Liu 2011), which can also be used to grow layered heterostructures of graphene with other two-dimensional materials (Zhang 2015), arc discharge of graphite electrodes (Subrahmanyam 2009, Levchenko 2010) and plasma "unzipping" of carbon nanotubes to create semiconducting nanoribbons of mono- and few-layer graphene (Jiao 2009).

2.2.1. Chemical vapour deposition growth of graphene

Of the alternatives to mechanical cleavage, chemical vapour deposition (CVD) of carbon onto catalytic metal substrates is the most wide-spread method of producing

large-scale samples of monolayer graphene. Samples grown on metal are able to be transferred in large areas by inexpensive and simple lithographic procedures and inexpensive metals such as copper or nickel are capable of catalysing the growth of graphene (Mattevi 2010), giving CVD a clear-cut advantage over epitaxial growth on expensive SiC, where sophisticated techniques are required to transfer samples and samples suffer damage (Unarunotai 2009).

Recently, researchers from Sony Corporation have used chemical vapour deposition onto copper substrates to grow high-quality monolayer graphene at industrial proportions, demonstrating sheets of CVD-grown polycrystalline graphene transferred onto epoxy sheets 100 m in length (Kobayashi 2013). By allowing the natural oxide layer to remain on copper substrates to inhibit their catalytic activity – and thus the rate of formation of new nucleation sites – single crystal samples of graphene can reach areas of 16 mm^2 (Figure 2.3a) (Zhou 2013).

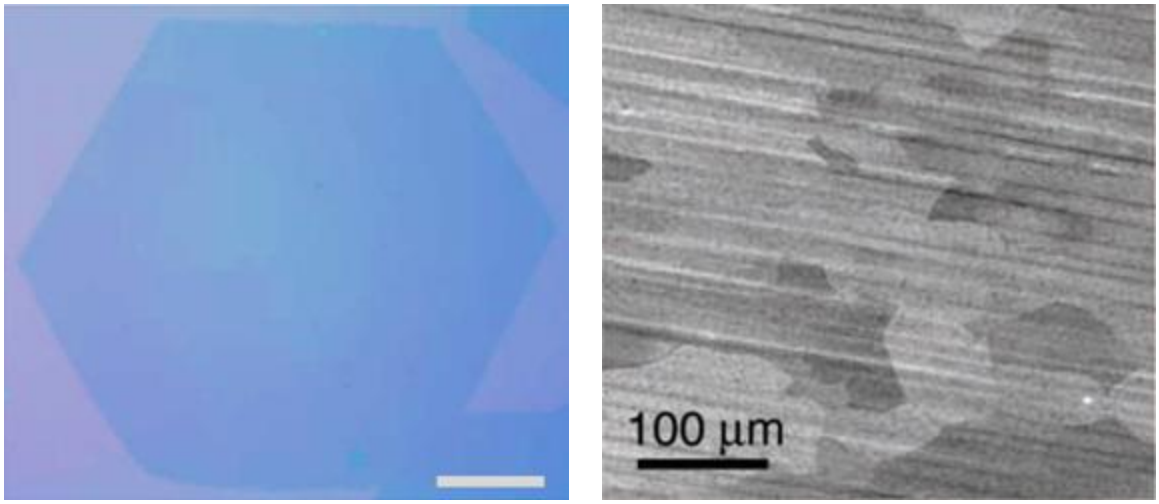

Figure 2.3: Microscope images of CVD-grown graphene on copper. (**a**) 5 mm graphene single crystal formed by CVD with severely limited nucleation sites, scale bar is 1 mm (Zhou 2013). (**b**) SEM image showing crystals of monolayer graphene roughly 100 µm in size covering a copper substrate after being grown by CVD using methane (Li 2009).

Experiments detailed in this thesis were performed using monolayer graphene samples grown by CVD onto copper substrates using high temperature decomposition of methane (Li 2009, Mattevi 2010), provided by colleagues at

University of Manchester. Our samples resemble Figure 2.3b, with graphene crystals of the order of 100-500 μm completely covering both sides of an 8 μm thick substrate of copper foil.

2.3. Functionalisation of graphene

Graphene is remarkably chemically inert. Carbon atoms in pristine graphene will form bonds with oxygen (Pei 2012), chlorine (Li 2011), fluorine (Nair 2010) or hydrogen (Elias 2009). While oxygen bonds very readily with graphene, its two valence electrons form bonds with two carbon atoms in the lattice which causes structural damage, and can form double bonds with carbon with the creation of a dislocation in lattice, thus the quality of graphene oxide is poor (Eigler 2013). Halogens, especially fluorine, form bonds with graphene while preserving the hexagonal structure (Leenaerts 2010), but the bonds are too strong to be easily broken (Nair 2010). We turn our attention, then, to hydrogen.

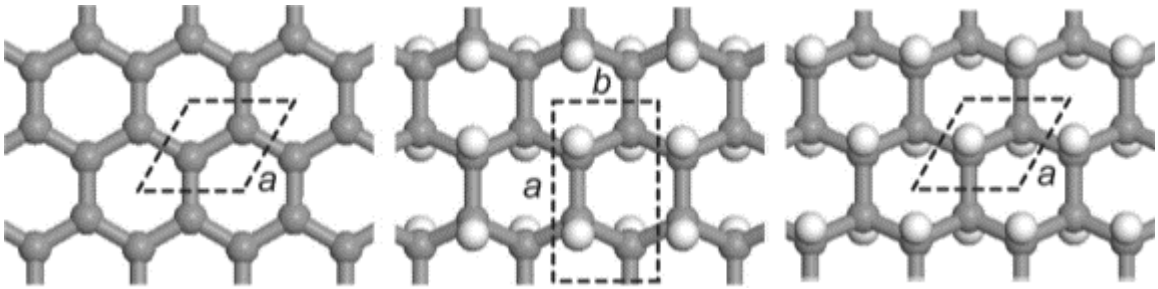

Figure 2.4: Atomic structures of (**a**) graphene, (**b**) boat graphane and (**c**) chair graphane, with unit cells marked by dashed lines (Flores 2009).

The stability of fully-hydrogenated graphene, or *graphane*, was determined by Sofo *et al.*, who suggested that individual hydrogen atoms can sit on alternating sides of the graphene sheet to form "boat" graphane or in pairs to form "chair" graphane – both formations were found to be stable (Sofo 2007). These studies have been reinforced since, with additional formations of graphane becoming more stable at high pressure (Wen 2011).

Electronically, Sofo *et al.* predict that graphane is insulating (Sofo 2007). For lower levels of hydrogenation, however, numerous groups suggest smaller band gaps that depend on the hydrogen content – allowing the potential for synthesis of fine-tuned band gaps by controlling the extent of hydrogenation (Balog 2010, Chandrachud 2010, Haberer 2010, Gao 2011). An interesting result from calculations by Savini *et al.* suggests that, with subsequent doping, partially- and fully-hydrogenated graphene could become superconducting at liquid nitrogen temperatures (Savini 2010).

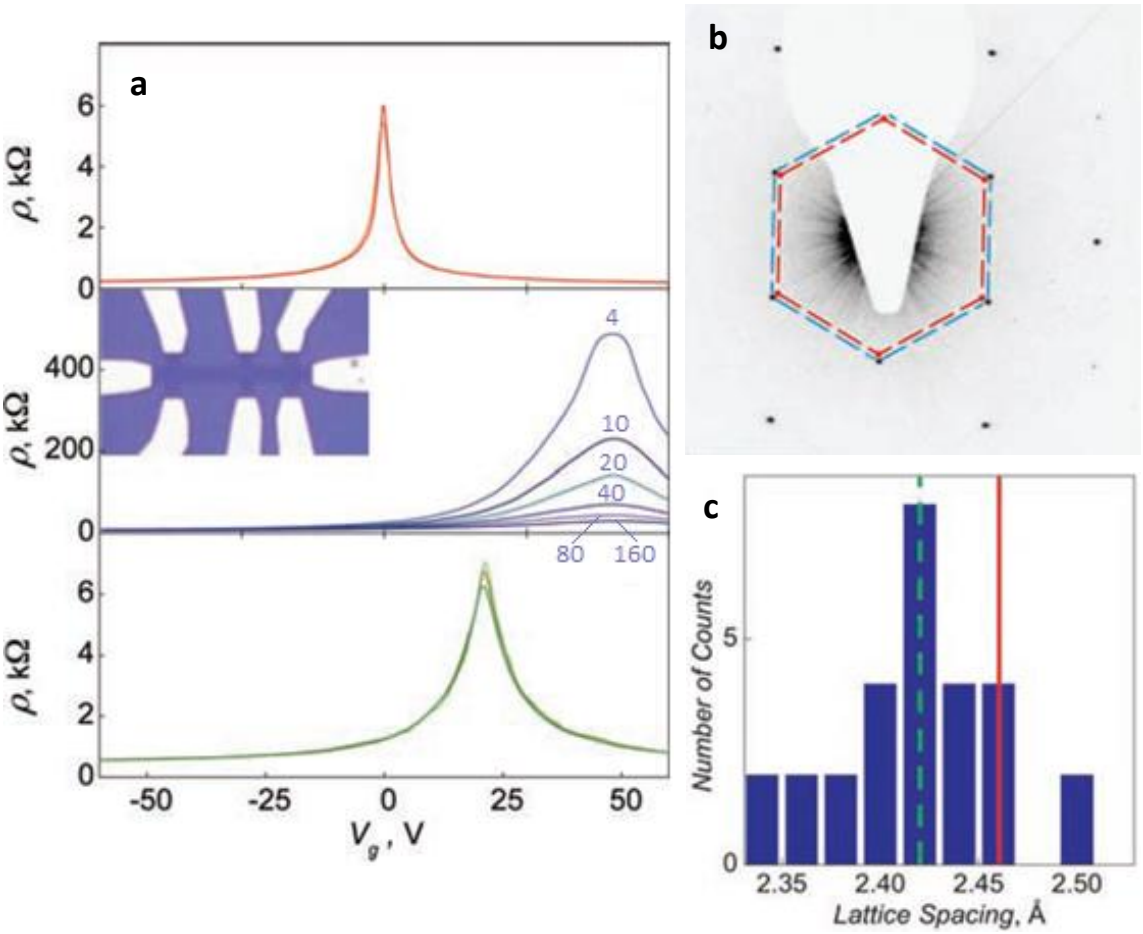

Figure 2.5: Changes in electronic and structural properties in graphene upon partial hydrogenation. (**a**) Electric field effect in graphene develops a strong temperature dependence upon hydrogenation (middle blue curves, temperatures in K above curves) compared with pristine and dehydrogenated graphene (top red and bottom green curves respectively) (inset: architecture of graphene Hall bar device), (**b**,**c**) Lattice parameter changes upon hydrogenation, red lines represent the lattice parameter of pristine graphene, blue and green lines show measurements on hydrogenated graphene (Elias 2009).

Evidence that graphane could be synthesised in the lab was first provided by Elias *et al.*, who exposed graphene to hydrogen plasma and noted changes in its electronic and structural properties (Elias 2009). Figure 2.5a shows the electric field effect of pristine, hydrogenated and dehydrogenated graphene on a similar device to that used in the first study on graphene (Novoselov 2004) after exposure to hydrogen. The electric field effect, first measured by Novoselov *et al.*, is temperature independent in pristine graphene, but develops a strong temperature dependence with hydrogenation – sheet resistance increases by a factor of 100 and charge carrier mobility was reported to decrease by four orders of magnitude when hydrogen is added (Elias 2009). The extent of the effect on sheet resistance is seen elsewhere to be a function of the extent of hydrogenation (Burgess 2011).

Through electron diffraction, Elias *et al.* were able to measure the in-plane lattice parameters of their partially-hydrogenated samples when prepared as a membrane and hydrogenated from both sides (Figure 2.5b and c). In spite of predictions to the contrary (Sofo 2007, Leenaerts 2010) – indeed, even simple calculations based on known C-H and C-C bond lengths from other hydrocarbons suggest that the in-plane lattice parameter should grow – the measurements show an overall decrease. The only existing discussion of this phenomenon in the literature considers that the small number of expanded hydrogenated regions are collectively compressing the remaining pristine graphene, since the hydrogen coverage is incomplete (Bangert 2010).

A crucial result of the study by Elias *et al.* is that it is possible to remove the hydrogen from partially-hydrogenated graphene using thermal annealing at 450°C, whereupon the electronic properties and structure of pristine graphene return (Elias 2009), whereas structural annealing of pure carbon into sp^2 layered sheets (*graphitisation*) does not commence until temperatures exceeding 500°C (Figure 2.6) (Saito 2004). Thus, the thermal removal of hydrogen from hydrogenated graphene acts as conclusive evidence that the changes in electronic and structural properties were due to hydrogen bonded to the graphene, and not due to other structural damage to the lattice. Thermal dehydrogenation of hydrogenated graphene is a widespread method of confirming hydrogenation, in some cases, hydrogen is seen to leave hydrogenated graphene at temperatures as low as 75°C (Luo 2009).

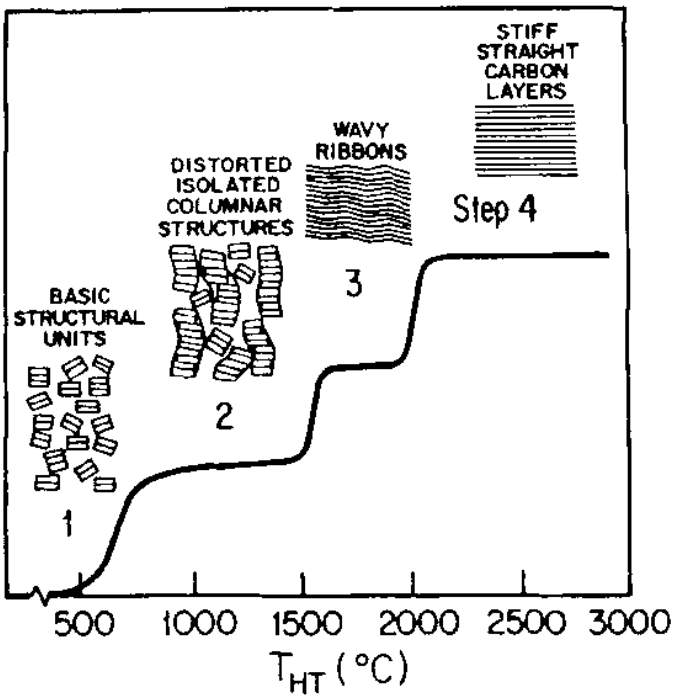

Figure 2.6: Stages of *graphitisation* of carbon – the structural rearrangement of carbon into sp^2 layered sheets with temperature annealing (Saito 2004).

Reports that the hydrogenated graphene can be decomposed by heating to such low temperatures contrasts with the conventional chemistry of the C-H bond, otherwise recognised as highly stable. In order to explain this, it is important to consider the environment surrounding the C-H bonds and the effects that this might have on the bond strength. For example, each of the sp^3-*s* C-H bonds in methane is able to exist at its optimum length and angle since the carbon atom is bonded only to three other hydrogen atoms – the lightest atom. As a result, this bond is not seen to break completely until temperatures up to 1200 K (Lenz-Solomun 1994). In the case of hydrogen bonding to graphene, the hydrogen atoms bond to a tertiary carbon atom which is in turn bonded to three tertiary carbon atoms, *ad infinitum*, to form a large, rigid two-dimensional crystal or macromolecule. The stiff carbon skeleton of graphene is unlikely to deform perfectly to sp^3 in order to facilitate the new C-H bonds, and the system will be under considerable strain. This discrepancy in bond angles compared with the perfect case (*i.e.* $\eta < 1$ rather than $\eta = 1$) likely leads to a severe reduction in the bond strength.

A useful comparison to make is with the C-H bond in buckminsterfullerene hydrogenated to saturation ($C_{60}H_{60}$), where the C-H bond energy is reduced

considerably compared with methane (Bakowies 1992), though it is important to acknowledge that even $C_{60}H_{60}$ – an ordered molecule with constant η – is under less strain than we would expect in partially-hydrogenated graphene – where we have long- and short-range variations in η.

The observations that the reaction between graphene and hydrogen is reversible also demonstrate the feasibility of carbon-based materials in solid-state hydrogen storage, where there is a need to reversibly bond hydrogen to the lightest element(s) possible to maximize hydrogen storage capacity by weight. Lithium is an unsuitable candidate since lithium hydride will not decompose until temperatures approaching 1000°C (Johnson 2002) and due to the volatility of pure lithium with water, while beryllium is both rare and toxic and boranes (BH_3 and B_2H_6) are gaseous at ambient conditions. A proper understanding of, and ability to control, the reaction between pristine graphene and hydrogen will therefore be critical in the development of carbon-based solid state hydrogen storage materials – especially since fully-hydrogenated graphane has not yet been synthesised, and the relationship between hydrogen content and reversibility is not known for higher hydrogen content.

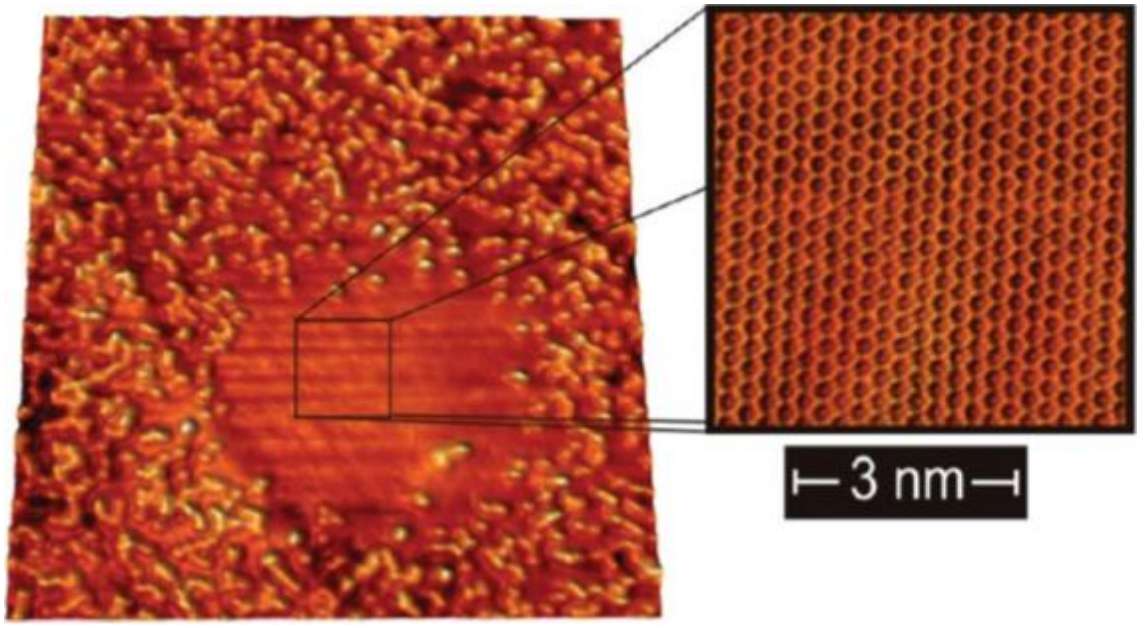

Figure 2.7: Atomic-scale STM images of graphene grown epitaxially on SiC and hydrogenated with atomised hydrogen. The hexagonal structure of pristine graphene is shown to reappear when hydrogen is removed from the surface using electronic field-stimulated desorption (Sessi 2009).

The reversibility has also been demonstrated by Sessi *et al.*, accompanied by impressive scanning tunnelling microscope (STM) images (Figure 2.7). Samples could be selectively dehydrogenated by applying a bias between the STM tip and hydrogenated graphene with the precision to form nanometre-scale features, within which the electronic properties of pristine graphene are observed to return (Sessi 2009). Selective dehydrogenation of hydrogenated graphene has also been performed by Wang *et al.*, who developed a plasma-enhanced CVD method to grow hydrogenated graphene directly, and use thermal annealing or irradiation with a laser to create pristine graphene features on the micrometre scale (Wang 2010). The high levels of control over the dehydrogenation of insulating hydrogenated graphene presents an alternative method through which the functionalised material can be used to synthesise tailored band gaps – through patterning of graphene nanoribbons into hydrogenated regions.

With further functionalisation of graphene by replacing hydrogen atoms with other functional groups, the effectively infinite surface area-to-volume ratio of graphene could be exploited for fast and effective drug molecule carriers in biomedicine (Yang 2013) and bio-sensors (Kuila 2011), and improvements in the bonding between graphene and host materials in composite materials could see improvements of their mechanical properties (Potts 2011).

2.4. Functionalised nanographite

A common approach to producing large batches of hydrogenated graphene is a top-down approach employing the wet chemistry method known as Birch reduction onto either graphite or graphite oxide. This process utilises an alkali metal (typically lithium or sodium (Yang 2012, Eng 2013)) which forms a salt in a solution of ammonia to act as an electron source, and an alcohol to act as a proton source (Birch 1944). The reaction then takes place over two stages, the salt provides the graphite with electrons to form local anionic sites, which draw protons from the alcohol to form hydrogenated groups on the lattice (Pumera 2013).

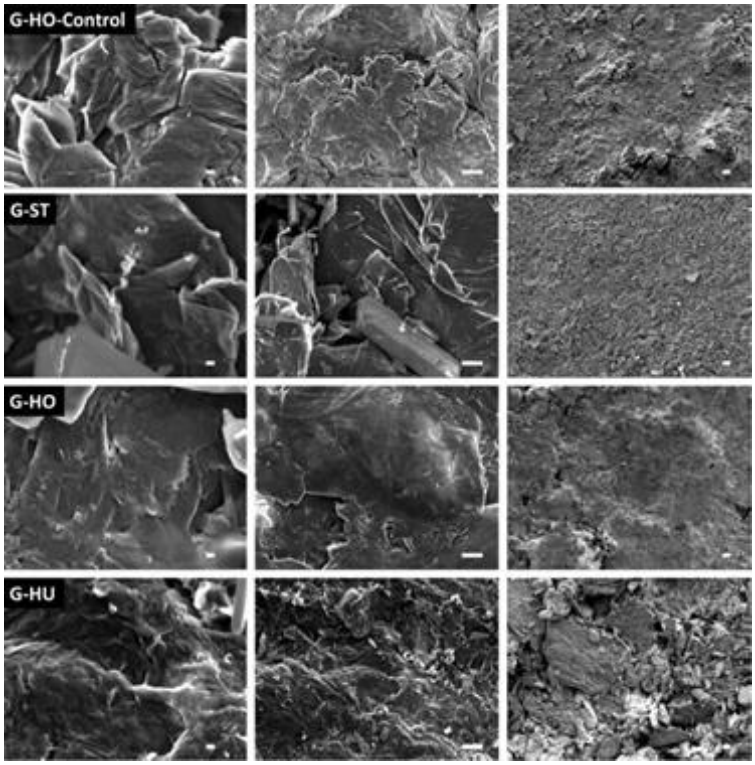

Figure 2.8: SEM images of hydrogenated graphene samples produced by Birch reduction of graphite oxide. Scale bars are 0.1, 1 and 10 μm in columns left to right (Eng 2013).

Figure 2.8 shows the product of Birch reduction of graphite oxide: a powder comprising three-dimensional particles of graphitic carbon on the nanometre scale, with structural defects caused by damage to the sp^2 sheets as a result of oxygen atoms bonding to the lattice in two locations during the oxidation stage. The presence of defects is well-known (Bagri 2010) and it is possible that a large proportion of the hydrogen content is bonded to existing defects and not pristine lattices. It is important to point out that monolayer graphene is unable to exist without at least partial support from a substrate at temperatures above 0 K without out-of-plane phonons causing it to "melt" into amorphous 3D carbon (Meyer 2007), making it possible to conclude that such suspensions do not contain monolayer graphene. While such samples are widely published as hydrogenated graphene or even graphane in the literature (Sofer 2015), their defective, three-dimensional nature does not qualify them for comparison with samples of functionalised monolayer graphene.

Chapter 3. Raman spectroscopy

3.1. Raman spectroscopy

A small proportion of the light incident on a material is scattered inelastically in processes which either generate or annihilate vibrational and rotational modes in a molecule or phonons in a crystal. The processes are called Stokes and anti-Stokes Raman processes for generation and annihilation respectively, and – since energy is conserved – give rise to:

$$E_{\text{scattered}} = E_0 \pm E_{\text{m}} \tag{3.1}$$

Classically, when light is incident on a material, its electric field component $\boldsymbol{E}$ creates an induced dipole moment $\boldsymbol{\mu}$, which depends on the polarisability of the material α *via*:

$$\boldsymbol{\mu} = \alpha \boldsymbol{E} \tag{3.2}$$

Due to intrinsic motions m (*i.e.* vibrations, rotations or phonons) of the material, its polarisability oscillates and can be expressed in terms of a static polarizability α_0 and a time-dependent term with magnitude α_{m} and frequency ν_{m} as:

$$\alpha = \alpha_0 + \alpha_{\text{m}} \cos\left(2\pi\nu_{\text{m}} t\right)$$

And 3.2 becomes:

$$\boldsymbol{\mu} = \alpha_0 \boldsymbol{E} + \alpha_{\text{m}} \boldsymbol{E} \cos\left(2\pi\nu_{\text{m}} t\right) \tag{3.3}$$

The electric field component of the incident light varies with a frequency ν_0 according to:

$$\boldsymbol{E} = \boldsymbol{E}_0 \cos\left(2\pi\nu_0 t\right) \tag{3.4}$$

Combining equations 3.3 and 3.4, we have:

$$\boldsymbol{\mu} = \alpha_0 \boldsymbol{E}_0 \cos\left(2\pi\nu_0 t\right) + \alpha_{\mathrm{m}} \boldsymbol{E}_0 \cos\left(2\pi\nu_{\mathrm{m}} t\right)\cos\left(2\pi\nu_0 t\right)$$

By employing trigonometric identities, the induced dipole moment due to incident electromagnetic radiation can be rewritten as:

$$\boldsymbol{\mu} = \alpha_0 \boldsymbol{E}_0 \cos\left(2\pi\nu_0 t\right) + \frac{1}{2}\alpha_0 \boldsymbol{E}_0 \cos\left[2\pi\left(\nu_0 - \nu_{\mathrm{m}}\right)t\right] + \frac{1}{2}\alpha_0 \boldsymbol{E}_0 \cos\left[2\pi\left(\nu_0 + \nu_{\mathrm{m}}\right)t\right] \tag{3.5}$$

The oscillating charge due to this induced dipole moment thus re-emits radiation at three frequencies according to each of the terms in equation 3.5. The first term relates to the elastic Rayleigh scattering process, where the scattered light has same frequency as the incident light. The second and third term correspond to inelastic Raman scattered light, where the frequency of the scattered light is altered when some of the incident energy is used to create (the second term – Stokes scattering) or annihilate (the third term – anti-Stokes scattering) a vibration in a molecule or a lattice phonon in a crystal (Moore 1983).

A quantum mechanical treatment of Raman scattering processes is aided by the energy level diagram in Figure 3.1, a visual representation of equation 3.1 which shows the transitions into a virtual, unstable energy state due to the interaction with the incident photon and the re-emission of a photon due to Rayleigh and Raman processes.

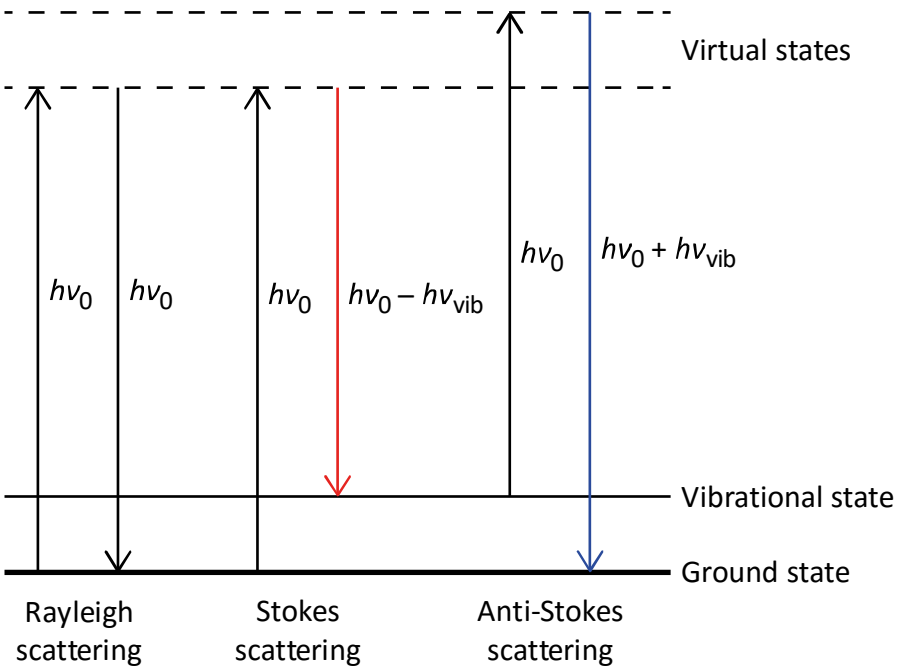

Figure 3.1: Energy level representation of light scattering processes, displaying the excitation of a material into some virtual energy state by the incident photon, from which it decays to produce the scattered photon.

Fermi's golden rule from perturbation theory gives the probability of a transition occurring between two states, initial i and final f, with wavefunctions $\psi_{i,f}$ (Moore 1983). The probability is expressed as the transition dipole moment $\boldsymbol{p}$:

$$\boldsymbol{p} = \langle \psi_f | \boldsymbol{\mu} | \psi_i \rangle$$

Through equation 3.2, the transition moment can be written in terms of the incident electric field and the polarisability of the material:

$$\boldsymbol{p} = \boldsymbol{E} \langle \psi_f | \alpha | \psi_i \rangle \qquad 3.6$$

We can assume that the wavefunctions $\psi_{i,f}$ are orthogonal, and as such, equation 3.6 acts as a selection rule for Raman scattering as it dictates that the transitions shown in Figure 3.1 lead to a non-zero induced dipole moment only when they create a change in the polarisability α of the material (Moore 1983, Hollas 1996). This selective property makes Raman spectroscopy a powerful tool for observing the structural properties of a material, since only specific phonons and molecular vibrations are available to a lattice or molecule, based on its symmetry. It is also why we do not observe a Raman spectrum from metals, as the metallic bonding – where

valence electrons exist as a free gas surrounding a lattice of metal cations – means that the material is infinitely polarisable.

Following equation 3.1, it is conventional that Raman spectra are displayed in units of wavenumbers relative to the excitation energy, allowing for a direct measurement of the energy of the phonons or molecular vibrations which give rise to features in the spectrum.

3.2. Raman spectrum of graphene

Raman spectroscopy has a long history in structural analysis of carbon materials, with different allotropes of carbon displaying the same sets of features between 1000 and 3000 cm^{-1}, but their shapes, positions and relative intensities giving great insight into the material's structure on the atomic level – Figure 3.2 gives a range of examples of Raman spectra of bulk carbon and carbon nanomaterials.

The Raman spectrum of monolayer graphene was first measured by Ferrari *et al.* and its most prominent features are the sharp peak at ~1580 cm^{-1}, termed the G peak, and the more intense peak at ~2700 cm^{-1}, the 2D peak (Ferrari 2006), similar to the Raman spectrum of bulk graphite (Figure 3.2), which has been measured since the 1970s (Tuinstra 1970, Tsu 1978).

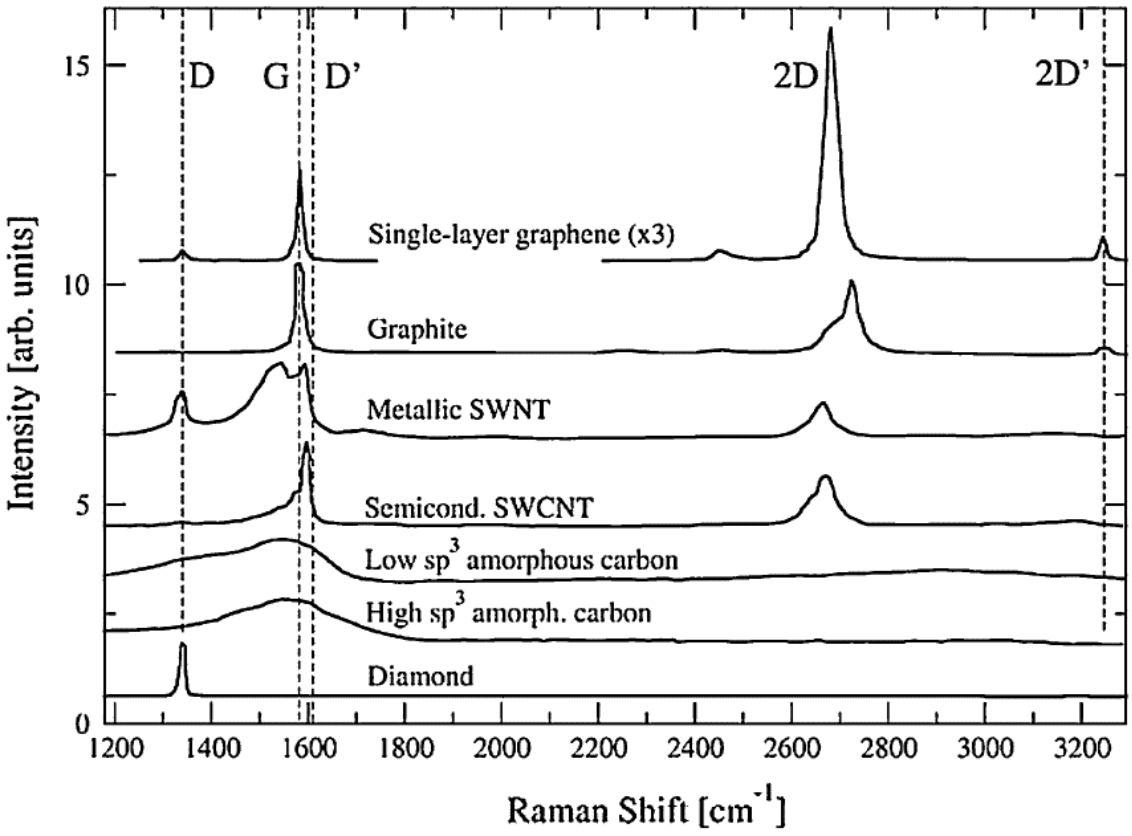

Figure 3.2: Raman spectra of various macroscopic and nano-scale carbon materials, each exhibiting some combination of "D" and "G" peaks (Ferralis 2010).

The G peak can be explained by standard group theory derivations of the normal modes for a single layer of graphene, which gives four normal modes (Tuinstra 1970, Reich 2004), of which the E_{2g} mode is the only Raman active mode. It is important to point out that the motion of the carbon atoms in the E_{2g} vibrational mode (see Figure 3.3) is a stretching motion between pairs of sp^2-bonded carbon atoms and does not require presence of aromatic rings for its activation, explaining its presence in amorphous carbon and linear chain molecules (Ferrari 2000).

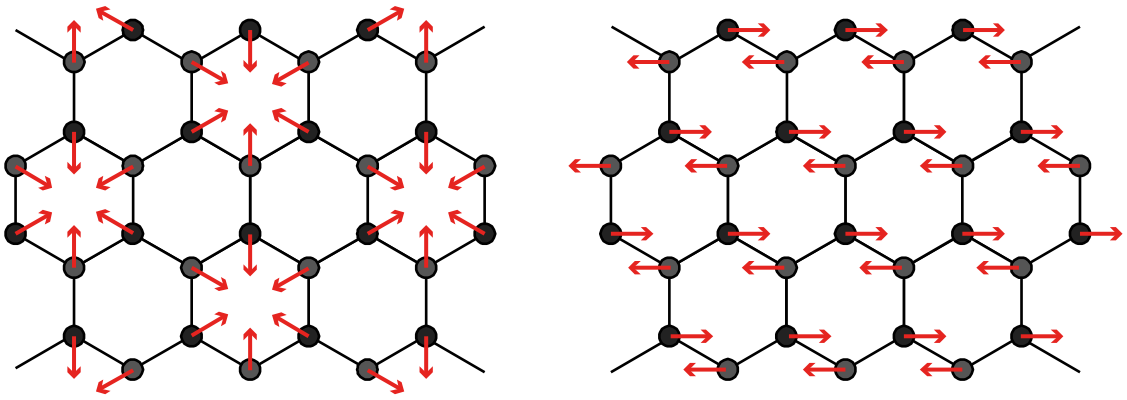

Figure 3.3: Visual representations of the motion of sp^2 bonded carbon atoms due to the A_{1g} and E_{2g} phonon modes, responsible for the D and G bands respectively in carbon Raman spectra.

The D peak in graphite was measured alongside the G peak in various graphitic materials by Tuinstra & Koenig, and the similarities between the D peak in defective graphite and the peak seen in diamond were immediately dispelled by noting discrepancies in the relative intensity and position of the peak (Tuinstra 1970). This is supported by the observation that the Raman scattering efficiency of sp^3 carbon in diamond is some 55 times smaller than that of planar sp^2 carbon, thus the small volumes of sp^3 carbon to be expected in high-quality graphite would not lead to a sizeable Raman peak (Wada 1980).

Instead, the D peak in pure graphite is explained by the finite particle size of graphite crystals caused by defects or edges. By considering the graphite crystallites as large but finite molecules, a new normal mode of vibration can be deduced, the A_{1g} phonon (Figure 3.3) which is not Raman active in an infinite crystal (Tuinstra 1970). Further confirmation that the D band in graphitic carbon is due to non-sp^2 defects can be sought by chemical modification of graphite, where reactants add defect sites to the lattice and the distance between defects becomes an effective crystallite size, Wang *et al.* showed that reactions with boron and oxygen produce a D peak identical to that observed near crystal edges (Wang 1990).

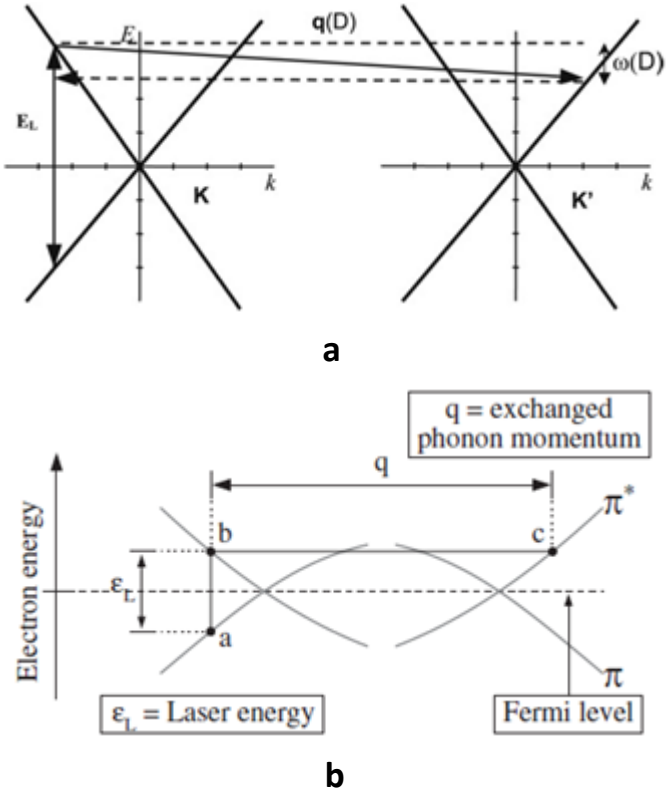

Figure 3.4: Intra-valley double resonance Raman scattering processes in sp^2 carbon which lead to (**a**) the D peak through defect scattering (Ferrari 2007) and (**b**) the 2D peak in pristine graphene and graphite (Ferrari 2006).

Unusually, the D peak in carbon exhibits a dispersion with excitation energy which Thomsen & Reich explain to be a result of a double resonance process shown in Figure 3.4a, whereby electrons are scattered between the bands of the linear phonon dispersion near the K and K' points of graphite and then elastically scattered by defects or edges (Thomsen 2000, Ferrari 2007). A similar, but intra-valley, scattering process can occur between the branches near the Γ point, giving rise to the D' peak around 1620 cm^{-1} in defective sp^2 carbon (Ferrari 2007). By showing, alongside data from Vidano *et al.*, that the 2D peak at ~2700 cm^{-1} – then often termed G' – has a dispersion which is double that for the D peak, Wang *et al.* deduced that the 2D peak is the second overtone of the D peak (Vidano 1981, Wang 1990).

It is interesting, then, that we are able to see a 2D peak in pristine graphene and graphite, without the defects which activate the D peak. Ferrari *et al.* attribute the 2D peak to a double resonance process comprising two phonons at the K and K' points with equal and opposite momentum – arrow q in Figure 3.4b (Ferrari 2006). This two-

phonon process does not require defects, and thus the 2D peak is observed in pristine graphene and graphite (Ferrari 2013).

Ferrari *et al.* describe the same double resonance process for bilayer graphene, where the electronic properties are changed due to interactions between the two layers, causing the π and π* branches of the electronic dispersion to split (Ferrari 2006, Piscanec 2007). This leads to a 2D peak in bilayer graphene comprising four components, visible in the fitting of the 2D peak in Figure 3.5b (Graf 2007). The evolution of the 2D peak with number of atomic layers of graphene (Figure 3.5) clearly distinguishes monolayer and bilayer graphene samples from thicker nanographites and bulk graphite.

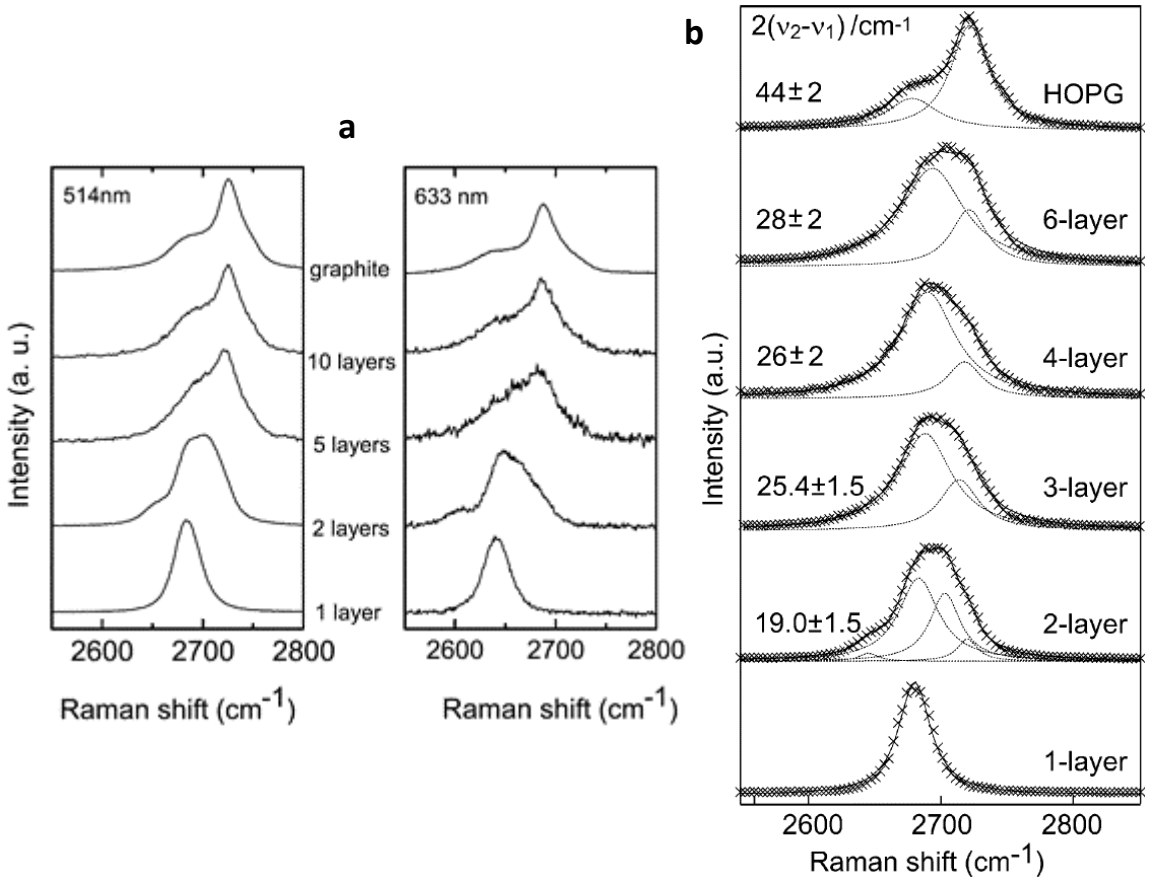

Figure 3.5: Change in the shape of the 2D peak of sp^2 carbon with the number of layers, from a single sharp peak in monolayer graphene to a broad doublet in bulk graphite. (a) Note the shift in position and difference in shape of the 2D band with changing excitation frequency (Ferrari 2006), (b) Note the increased splitting of the components (numbers left) of the 2D peak with increasing layers (Graf 2007).

The drastic change in 2D peak shape shown in Figure 3.5 allows easy identification of monolayer graphene. This can be supported by a calibration of the G peak frequency ω_G, which varies with the number of layers n according to:

$$\omega_G = 1581.6 + \frac{11}{\left(1 + n^{1.6}\right)}$$

Which gives an expected G peak position of 1588.1 cm^{-1} for monolayer graphene (Wang 2008).

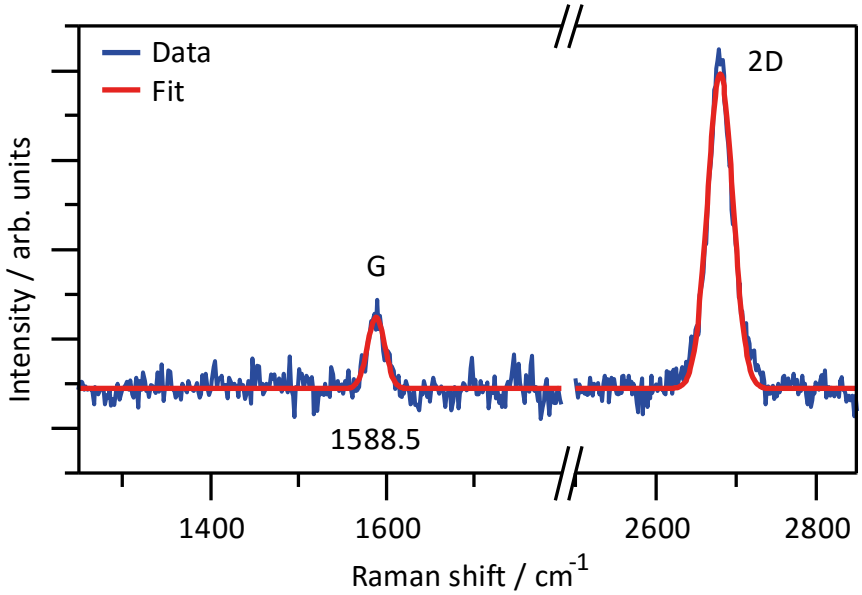

Figure 3.6: Representative Raman spectrum of graphene samples grown on copper substrates used throughout this work presented with fitted peaks from MagicPlot Student software. Confirmation that the samples are monolayer comes from the position of the G peak (Wang 2008) and the shape of the 2D peak (Ferrari 2006).

An example of the Raman spectrum of graphene samples used throughout this thesis is shown in Figure 3.6 (details on spectrometer arrangement can be found in § 3.5), with no indication of D peak activity suggesting defect-free sp^2 carbon. The 2D peak is clearly symmetrical and can be fitted with a Gaussian peak, and the measured G peak frequency is within 0.4 cm^{-1} of the expected value from calculations, both confirming the monolayer nature of the samples.

3.3. Raman analysis of modified graphene

Due to the small sample sizes and necessity of a substrate material for graphene, the accuracy of traditional methods for chemical analysis such as mass spectrometry or combustible element analysis is hindered. However, modification of graphene brings about important changes in its Raman spectrum due to the change in its structure – the most striking of which is the development of the D peak.

The D peak, as discussed in § 3.2, is related to disorder in graphitic carbon. The relationship between its intensity and crystallite size in graphite has been known since the recording of the graphite Raman spectrum by Tuinstra & Koenig, who noted the intensity ratio I_D/I_G is linear with the inverse of the crystallite size L_D (Tuinstra 1970). The relationship was more recently studied at a variety of wavelengths and with L_D measured accurately, using both STM imaging and X-ray diffraction Scherrer broadening, on a range of samples by Cançado *et al.*, who determine a general relationship between L_D and I_D/I_G (Cançado 2006):

$$L_D = 2.4 \times 10^{10} \lambda^4 \left(\frac{I_D}{I_G} \right)^{-1} \qquad 3.7$$

However, the Cançado study uses a minimum crystallite size of 20 nm. Expansion of the relationship below 20 nm has been performed by Lucchese *et al.*, who show the evolution of the Raman spectrum of graphite upon deliberate generation of defects in the lattice caused by bombardment with Ar^+ ions (Lucchese 2010). Atomic resolution STM images are used to determine defects per unit area, and thus their average spacing L_D, which is plotted against the Raman intensity ratio I_D/I_G in Figure 3.7 – which shows a peak in the relative D peak intensity at around L_D = 4 nm.

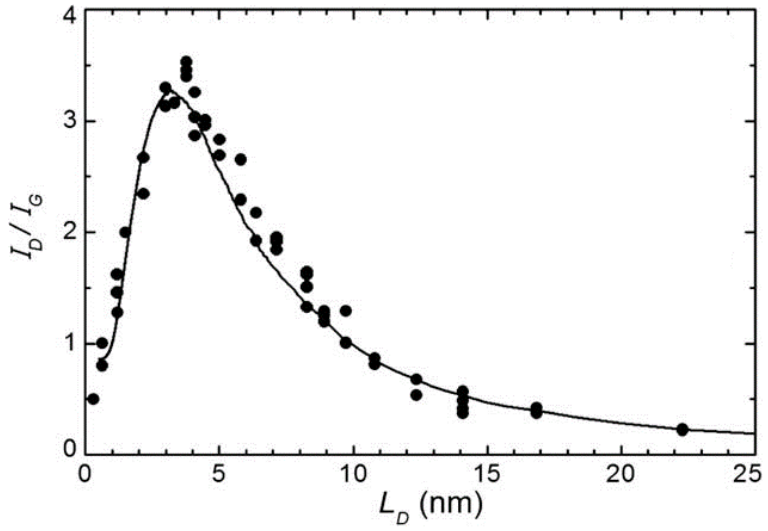

Figure 3.7: Behaviour of D to G peak intensity ratio I_D/I_G as a function of reducing spacing L_D between defects (λ = 514.5 nm) (Lucchese 2010).

We expect an equivalent change in the Raman spectrum when modifying graphene through chemical reactions with adatoms, and increasing the concentration of adatoms is equivalent to reducing L_D. The covalent bond formed between the carbon in the graphene lattice and the adatom will force the carbon atom to give up its π bonding with its nearest neighbours in place of an out-of-plane σ bond, ideally changing the bonding of that carbon atom from sp^2 to sp^3 – though more realistically, due to the stiffness of the graphene sheet, increasing the η value of the $sp^{2+\eta}$ bonding of the atom. These sp^3-like, high η locations behave as defects on the otherwise sp^2-like, low η lattice – effectively breaking the graphene into smaller domains with average size L_D related to the density of defects.

By exposing graphene to fluorine generated by decomposition of xenon difluoride (XeF_2), Nair *et al*. have observed the synthesis and recorded electronic, structural and mechanical properties of partially-fluorinated graphene and fully-fluorinated fluorographene (Nair 2010). Their spectra are displayed alongside the spectra by Lucchese *et al.* to demonstrate the similarities in Raman spectra of functionalised and disordered graphene in Figure 3.8.

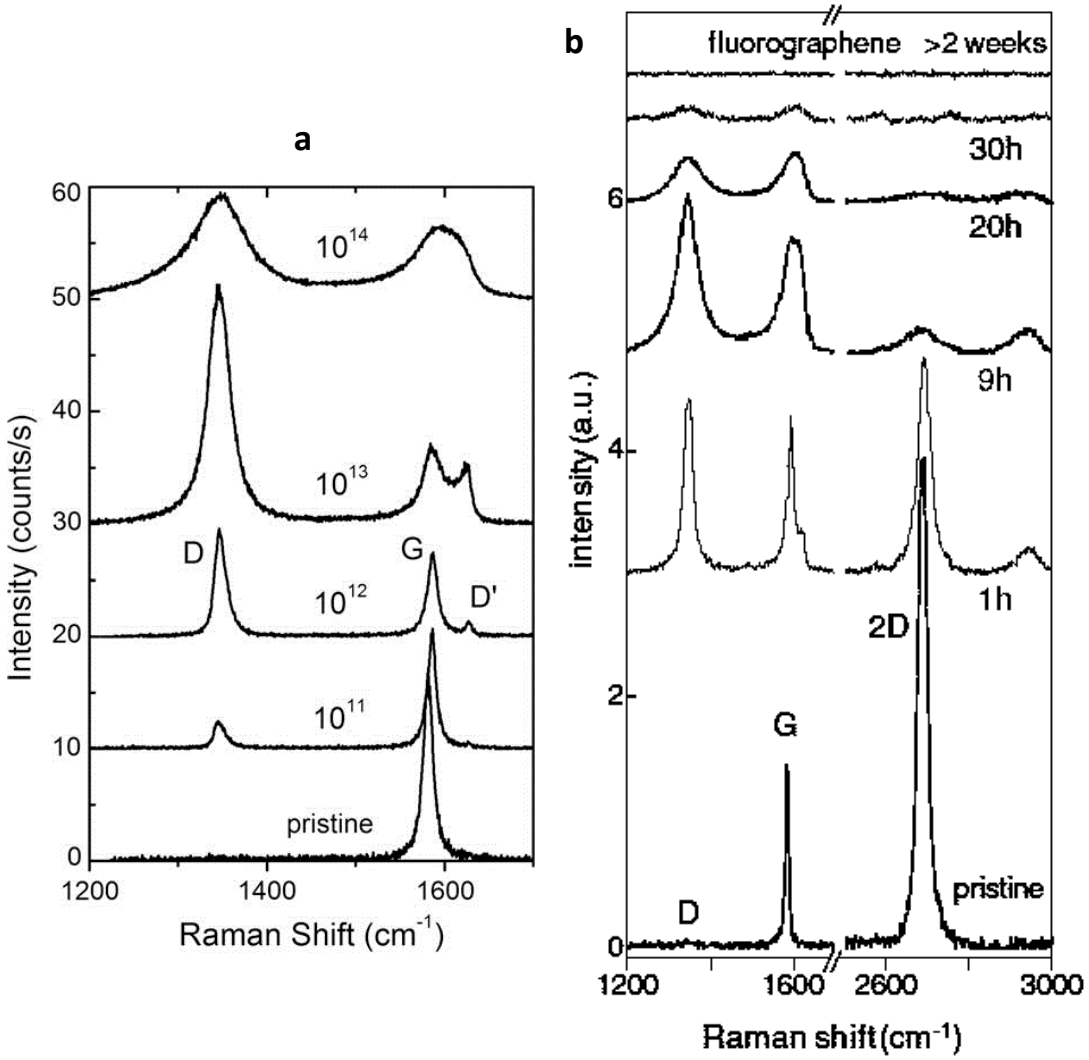

Figure 3.8: Evolution of Raman spectrum of graphene with increasing defects or adatoms. (**a**) Changes in Raman spectrum of graphene from pristine graphene to highly disordered graphene after bombardment with ions, ion dose (Ar^+/cm^2) is shown above spectra (Lucchese 2010), (**b**) Changes in Raman spectrum of graphene upon gradual fluorination (exposure to XeF_2 shown above spectra) (Nair 2010).

Importantly, the spectra in Figure 3.8b also show the expectations for fully-functionalised graphene – *i.e.* when bonding becomes completely sp^3-like. In such cases, we expect an unobservable Raman spectrum at all frequencies, as the scattering cross-sections from sp^3 carbon is sufficiently small as to only be measurable in bulk samples of sp^3 carbon, such as diamond.

Thus, by using the information made available from the studies on the deliberate destruction and the complete fluorination of monolayer graphene, shown in

Figure 3.8, it is possible to define three stages of functionalisation of monolayer graphene based on changes in its Raman spectrum:

- **Stage I – low levels of functionalisation**
  - Introduction of disorder-related Raman peaks D, D', and D+D'.
  - I_D/I_G increases with increasing functionalisation to a maximum value.
  - I_{2D}/I_G decreases.
- **Stage II – high levels of functionalisation**
  - Raman peaks broaden and soften with decreasing L_D.
  - I_D/I_G decreases to roughly 1.
  - 2D peak begins to disappear.
- **Stage III – fully-functionalised graphene**
  - Complete disappearance of Raman spectrum at all frequencies.

The nature of the G peak intensity, and thus I_D/I_G, to depend on excitation wavelength (Wang 1990, Cançado 2007) makes an absolute measurement of the average defect spacing L_D determined using equation 3.7 alongside a visual inspection of the spectrum using the criteria above a complete measurement of modification extent in graphene samples (Cançado 2006).

3.4. Experimental hydrogenated graphene

As discussed in § 2.3, the first hydrogenation of monolayer graphene was achieved by Elias *et al.*, who hydrogenated graphene with atomised hydrogen and recorded electronic properties of hydrogenated graphene and structural properties in the form of electron diffraction patterns and Raman spectra – shown in Figure 3.9 (Elias 2009). Elias noted enhancement of the defect-activated D, D' and D+D' peaks with hydrogenation and were able to enhance them further by preparing samples as a membrane, allowing the hydrogen access to the lattice from both sides. Crucially, the D peak in hydrogenated samples was seen to disappear after a thermal annealing significantly below the graphitisation temperature of carbon – *i.e.* below temperatures required to structurally anneal graphene – to reproduce the Raman spectrum of

pristine graphene (green spectra in Figure 3.9), giving evidence that the changes in the Raman spectrum were due to hydrogen bonded to the lattice.

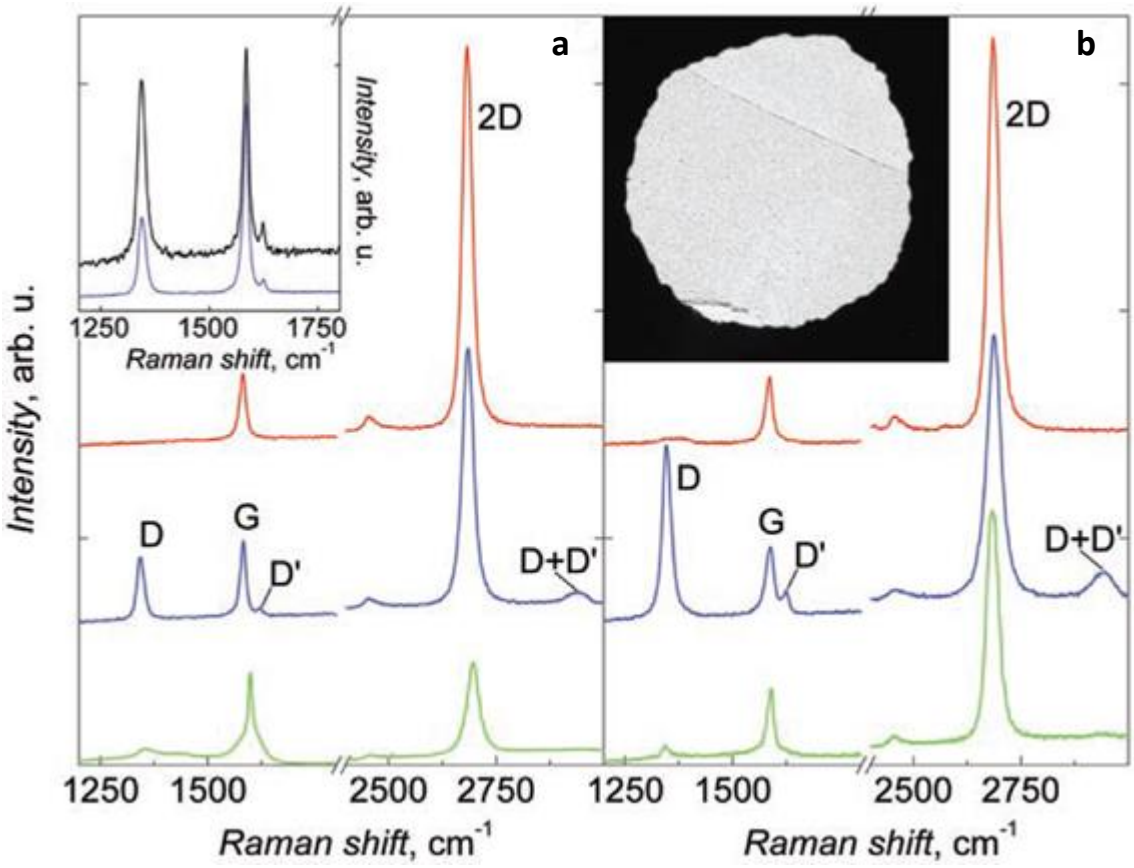

Figure 3.9: Hydrogenation of graphene by Elias *et al.* (**a**) Single-sided hydrogenation of graphene shows D peak and related defect peaks begin to appear in the Raman spectrum. (**b**) Graphene samples prepared as a membrane (photograph in right inset) show higher levels of hydrogenation overall and (left inset) after one hour of simultaneous exposure. Blue spectra are graphene after hydrogenation, red and green spectra are pristine graphene before hydrogenation and after annealing respectively (Elias 2009).

Following Elias *et al.*, the use of atomised hydrogen to make samples of hydrogenated graphene has become widespread in plasma-enhanced CVD chambers (Luo 2009, Burgess 2011, Matis 2012, Balog 2013) or with atomising guns (Balog 2009, Sessi 2009, Balog 2013, Guillemette 2013, Guillemette 2014). A range of recorded hydrogenated graphene Raman spectra by exposure to atomic hydrogen are collected in Figure 3.10.

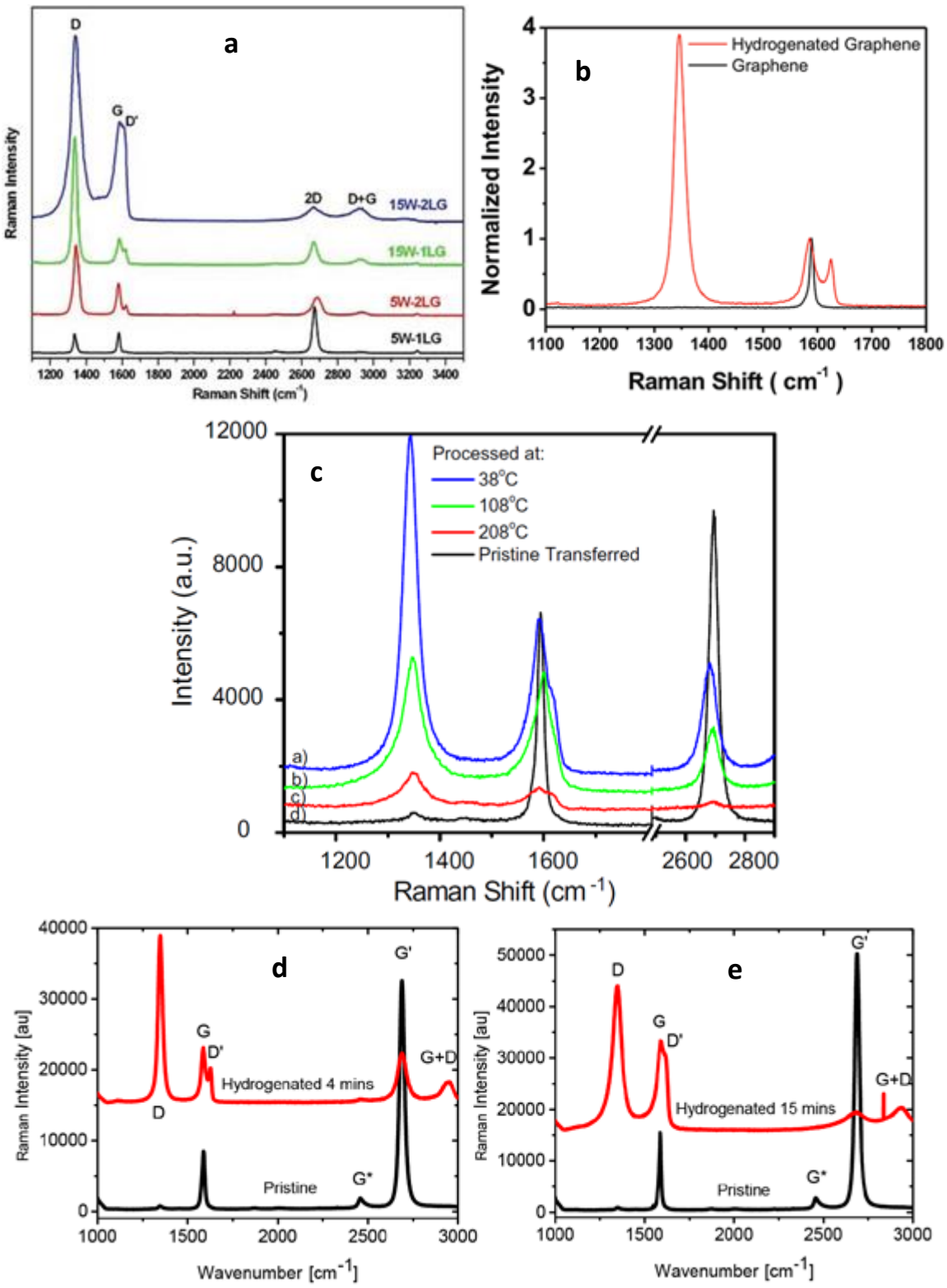

Figure 3.10: Raman spectra of hydrogenated graphene sample from the literature, prepared by (**a**,**b**,**c**) exposing graphene to hydrogen plasma in a plasma enhanced CVD chamber by (Luo 2009), (Matis 2012) and (Burgess 2011) respectively. (**d**,**e**) Hydrogenated graphene prepared by bombarding with hydrogen from an atomising gun (Guillemette 2014).

It is striking that the spectra shown in Figure 3.10c at high substrate temperatures resemble very low-L_D Stage II functionalised graphene (similar to 20 hours spectrum in Figure 3.8b), and yet Burgess *et al.* dismiss them as damaged due to their experimental procedures and do not use them for electronic measurements – this conclusion was supported by an inability to thermally anneal away the D peak in a sample with a spectrum resembling high-L_D Stage II (9 hour spectrum in in Figure 3.8b) (Burgess 2011). Their suggestion that above a measured I_D/I_G value of 2, the spectra resembles disordered graphene and not hydrogenated graphene allowed the conclusion that an I_D/I_G = 2 corresponds to a hydrogen coverage of ~10 at. %, based on calculations by Xiang *et al.* which suggest that single-sided hydrogenated graphene becomes unstable at 10 at. % coverage (Xiang 2010). Note that spectra in Figure 3.10d for longer exposures resemble high-L_D Stage II hydrogenated graphene. These samples were not subject to any documented annealing attempt (Guillemette 2014).

The attribution of Stage II-like appearance and subsequent inability to anneal away defects due to the physical damage to the graphene by high energy hydrogen atoms is also noted by Luo *et al.* (Luo 2009). The authors illustrate the sensitivity of their experimental procedure by showing hydrogenated and annealed Raman spectra for graphene subject to hydrogen plasma for 9 and 11 minutes on the same graph, where an 11 minute exposure lead to a defective spectra that was not reversible through annealing.

The explanation offered by both Luo *et al.* and Burgess *et al.* is that hydrogen plasmas are able to etch a graphene lattice, which is supported by the observation of CH_2 groups in the IR spectrum of single-walled carbon nanotubes using the same process (Zhang 2006) which form at the edges of etched sites. Both papers suggest a saturation in the hydrogenation extent, beyond which further treatment only causes physical defects, which suggests that hydrogenation by exposure to atomic hydrogen is not a strong candidate for synthesising fully-hydrogenated monolayer graphane. These points, alongside the observation by Nair *et al.* that higher-stage fluorinated graphene was not seen to be fully reversible by annealing in any case (Nair 2010), suggest that other analysis methods are necessary to gain conclusive insight on graphene functionalised to higher extents, such as direct imaging by STM (Sessi 2009).

3.5. In-house Raman spectroscopy

At University of Salford, we use a Raman spectrometer in the backscattering configuration employing a HORIBA Jobin Yvon iHR320 spectrometer fitted with 300 and 1200 lines/cm diffraction gratings, which images diffracted light onto a liquid nitrogen-cooled HORIBA Jobin Yvon Symphony CCD. Figure 3.11 shows the arrangement of optical components that comprise the spectrometer.

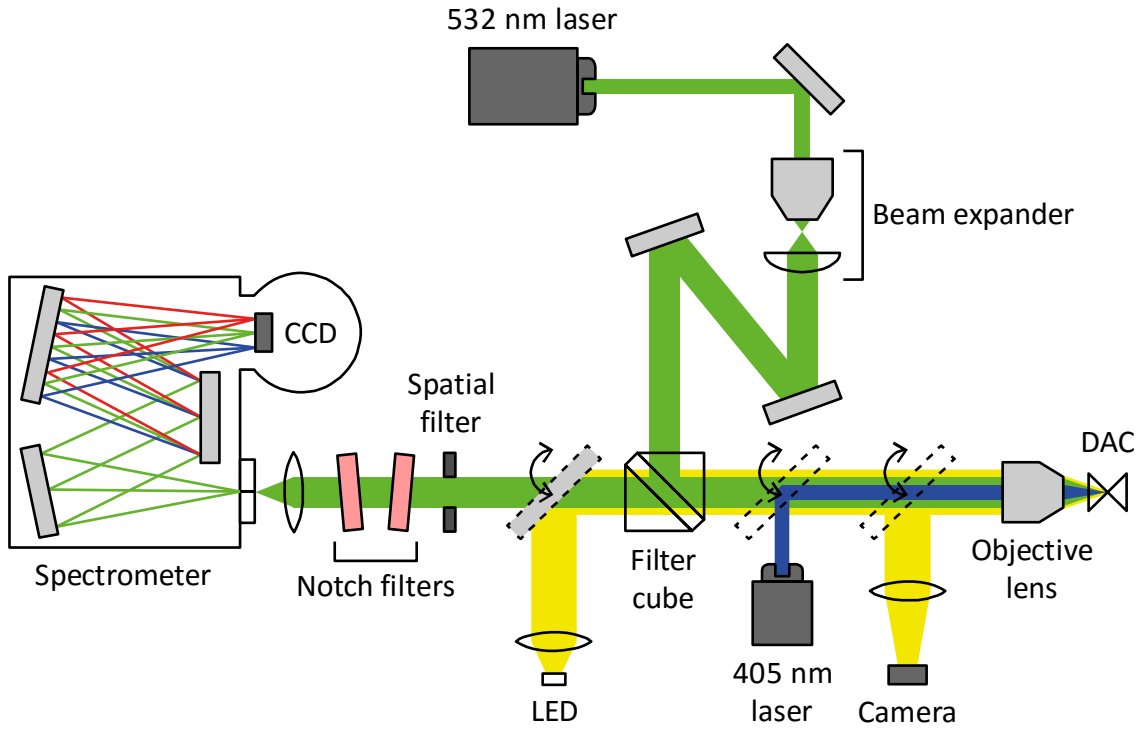

Figure 3.11: Arrangement of Raman spectrometer. Dashed lines show the mirror (grey) and beam splitters (empty) which can be used to introduce white light to image samples and blue laser light to excite photoluminescent pressure markers.

Light from a green solid state laser (532 nm, ~150 mW, Lasever Inc.) is directed through a beam expander comprising a short (f = 2.54 mm) focal length plano-convex lens and a Swift DIN40 objective lens (f = 0.65 mm) to produce a wide, collimated beam. The beam is then directed through a Kaiser Optics holographic narrow bandpass filter cube, where 99% of the light at the designated wavelength is diffracted by 90°. An objective lens focuses the light onto the sample – long focal length lenses can be used to perform Raman spectroscopy inside a diamond anvil cell (DAC).

At the collection end, a Kaiser Optics holographic notch filter and Kaiser Optics holographic SuperNotch-Plus filter are used to remove Rayleigh scattered and reflected light from the signal that has passed through the narrow bandpass filter. A convex lens (f = 75 mm) focuses the signal onto the slit entry of the spectrometer (typically 50 or 100 μm).

The dashed lines in Figure 3.11 show how white light can be introduced to allow the sample chamber of a diamond anvil cell to be imaged on a ThorLabs CMOS camera so that the laser can be navigated around the chamber, as well as how blue laser light can be introduced to excite fluorescent pressure markers (§ 4.2).

Chapter 4. Experiments at high pressure and high temperature

4.1. The heated diamond anvil high pressure cell

The incredible mechanical strength and hardness of diamond makes it an ideal material for anvils used to subject other materials to high pressure and its remarkable transparency over a wide range of electromagnetic frequencies – ranging from hard X-rays to infrared (Mildren 2013) – allows optical spectroscopy (Goncharov 2012) and X-ray diffraction (McMahon 2015) measurements to be made directly through the diamond anvil acting as a window. In combination with high temperature through resistive or laser heating (Gregoryanz 2004), diamond anvil cells are useful in experiments ranging from testing of materials' mechanical properties (Hanfland 1989) and pressure-temperature phase diagrams (Errandonea 2004), the synthesis of materials at extreme conditions (Lacam 1980, Scheler 2013) and in simulating the internal conditions of astronomical objects (Benedetti 1999, Petitgirard 2015).

During a DAC experiment, force applied externally to the cell is transferred to the wide back face (table) of the diamonds and then transformed down to the narrower front face (culet) to generate pressure. By the definition of pressure as force per unit area, it follows that diamonds with smaller culet faces are capable of reaching much higher pressures with only a small amount of external force applied. The practice of employing opposed anvils to reach high pressure was established long before the invention of the diamond anvil cell in the large tungsten carbide anvil presses used by P W Bridgman (Hazen 1999) to compress a monumental range of materials for the first time (Bridgman 1948), a technique which was later modified for the first synthesis of

manmade diamond (Bovenkerk 1959). With suitable tailoring of the geometry of the diamond anvils, DACs can be routinely use to achieve pressures in the Mbar range (Bell 1984, Howie 2015) and the novel introduction of a smaller, secondary anvil made of hard, nano-crystalline diamond fixed on the culet has recently seen pressures exceeding 7.5 Mbar achieved in a diamond anvil cell (Dubrovinsky 2012, Dubrovinsky 2015). For most experiments in this thesis, the diamonds employed were of a modified brilliant cut – designed to maximise the collection of backscattered light for optical spectroscopy measurements *in situ* through total internal reflection (Figure 4.1).

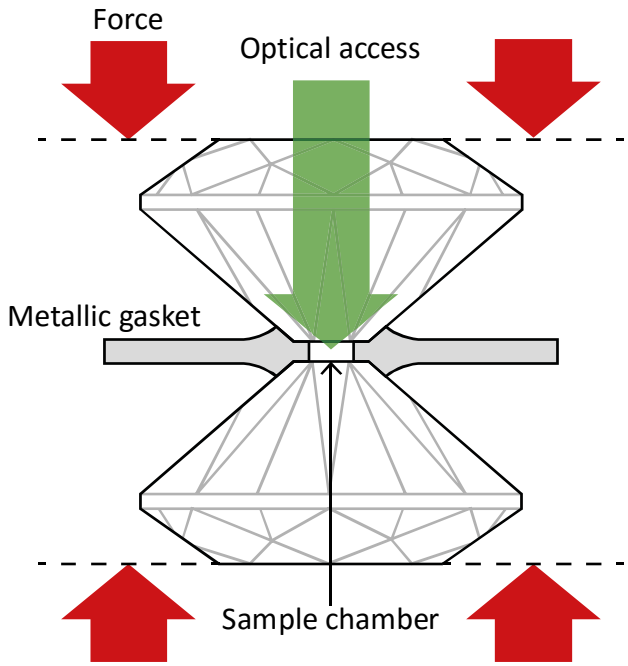

Figure 4.1: A diamond anvil cell arrangement featuring a pair of diamonds applying pressure to a pre-indented metallic gasket with sample chamber drilled through the indentation.

For the range of pressures of interest in this thesis, and thus the size of diamond culets required, sample chambers can be drilled using careful mechanical drilling or by spark erosion. The apparent ease of mechanical drilling is set back by both the tendency of finer drill bits to snap during drilling (often also at the expense of the gasket) and that even careful mechanical drilling leaves a burr – meaning that gaskets must be re-compressed and drilled numerous times to get a clean aperture. Spark erosion is performed on a spark eroder drill, which employs a micrometer barrel to move the gasket – submerged in paraffin oil – upwards towards a bit while applying

a large voltage between the two. As the bit approaches the gasket, the paraffin oil undergoes dielectric breakdown, causing sparks which remove material from the gasket. While slower, spark erosion has advantages over mechanical drilling in that positioning of the sample chamber is more accurate and the resulting aperture is cleaner.

Figure 4.2 shows photographs of the diamond anvil cells used in the experiments presented in this thesis. The room temperature (TE) cell has four slots around its body which house M4 screws sprung with Belleville washers for sensitive control over the pressure inside the cell. The high temperature (HT) cell has holes in the piston and cylinder that allow pressure to be applied using M5 screws, in accordance with the requirements for the cell to fit into the high pressure gas loading equipment at University of Edinburgh (see § 4.1.1). For greater control over the pressure, the load on the cell is transferred from the screws onto a lever arm vice during experiments.

For high temperature experiments, we employ a long piston-cylinder type DAC modified from the Mao-Bell design first used to reach 1 Mbar (Mao 1976), with a heating jacket placed around the cylinder. It is possible to see in Figure 4.2 the insulating cement on the top of the piston which holds in place a type K thermocouple placed inside the cell for a measurement of the temperature at the sample chamber. This thermocouple feeds back to a temperature control circuit that regulates the power supplied to a Watlow 120 V nozzle heater which acts as an external heating jacket to maintain a steady set temperature.

Typically, 0.1 carat diamonds with a 600 μm culet are employed. Through use of a set screw, the diamonds are kept a small distance (tens of μm) apart and their culets aligned. Small (~1 cm^2) plates of 200 μm-thick stainless steel are pre-indented to a thickness of typically 60-120 μm and sample chambers of 300 or 350 μm diameter are made in the centre of the indentation by either mechanical drilling or spark erosion.

Figure 4.2: Photographs of custom-made diamond anvil cells. (top) HT2, based on a Mao-Bell type piston-cylinder cell for use in combination with resistive heaters in experiments at combined high pressure and temperature. (bottom) TE3, a piston-cylinder cell suitable for experiments at ambient temperature.

Inside the cell, diamonds are glued to tungsten carbide seats with a step, such that the gap between the piston and cylinder bodies is sufficiently large to facilitate a second, smaller internal heater placed around the diamonds for experiments exceeding 1000 K, see Figure 4.3.

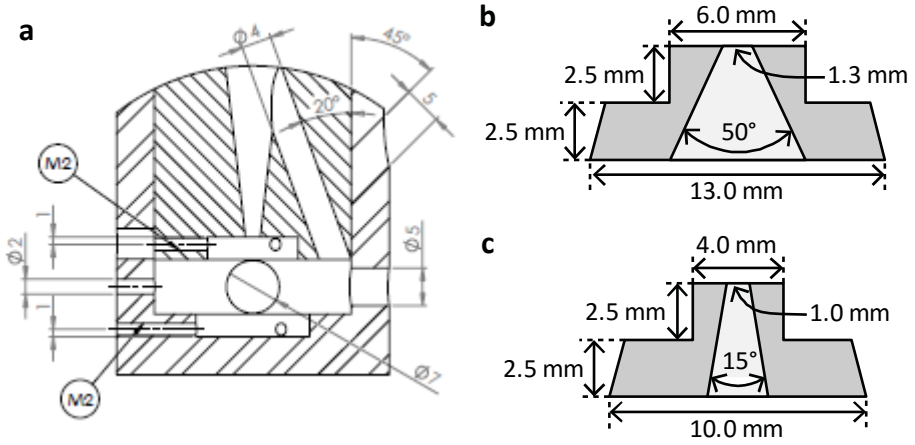

Figure 4.3: Internal design of the high temperature diamond anvil cell to facilitate an internal resistive heater. (**a**) The piston and cylinder as they appear when connected, showing the various entries that allow access to the alignment screws and viewing access to the diamonds, from original designs by Dr John Proctor. (**b**) Design of the cylinder seat to be used in experiments at high temperature – with wide opening for collecting backscattered light or diffracted X-rays. (**c**) Design of the piston seat.

4.1.1. High pressure gas loading of hydrogen into a diamond anvil cell

For experiments on hydrogenation of graphene in a DAC, we employ high pressure gas loading of hydrogen at University of Edinburgh. It is important to have hydrogen loaded at the highest a density possible to ensure that sufficient hydrogen is captured in the sample chamber to reduce the severity of the reduction in chamber size as fluid hydrogen is compressed to high pressures. There is also concern that hydrogen could be lost at higher pressures to diffusion into the gasket material surrounding the sample chamber, with iron hydride formed at 3.5 GPa (Badding 1991) and rhenium hydride above 5 GPa (Besedin 1998).

The high pressure gas loader at University of Edinburgh features a two-stage compressor. The first stage (*booster*) pump compresses the gas to 200 bar and feeds it

into the second (main) pump, where it is compressed as high as 2,000 bar inside a pressure vessel large enough to accommodate a DAC. Cells to be loaded with hydrogen are first calibrated such that a known amount of turns on the screws is required to bring the diamonds into contact with the gasket and then placed inside the pressure vessel. A system of gears connect the screws of the DAC to a wheel outside of the vessel so that the DAC can be closed in an atmosphere of 2,000 bar hydrogen (or deuterium), trapping enough gas in the sample chamber to reduce the amount by which the chamber shrinks as we raise the pressure to the gigapascal range.

Success of the loading is confirmed by looking for the hydrogen vibron in its Raman spectrum at around 4,000 cm^{-1} inside the sample chamber. For carriage back to University of Salford, hydrogen is solidified by compressing above 5.5 GPa (Mao 1979), and the phase change is further confirmed by the softening of the low-frequency roton modes (Howie 2013).

4.1.2. Loading diamond anvil cells with CH_4

To load a DAC with methane in such a way that sufficient methane is in the sample chamber to prevent large-scale collapsing of the chamber on pressure increase, we exploit methane's boiling temperature of 111 K (Gordon 1972) at ambient pressure and employ cryogenic loading methods.

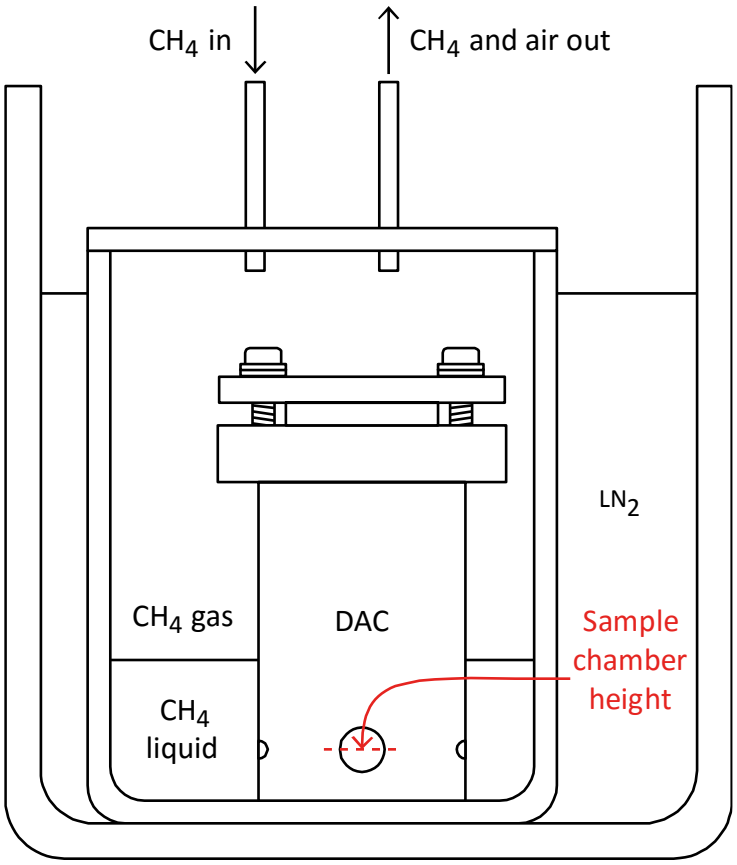

Figure 4.4: Cryogenic loading of methane into a HT-DAC. Liquid nitrogen cools the inner container until methane begins to condense and sufficient liquid methane has collect to fill the sample chamber, before the methane flow is stopped, inner chamber unsealed and the cell closed.

Figure 4.4 shows the method in which methane is loaded into a diamond anvil cell. In the same way as with hydrogen loadings (§ 4.1.1), cells are calibrated such that there is a known amount of turns required on the screws for the cell to close completely, and the cell is placed inside a container. The container for methane loadings is a sealable steel vessel with thick Perspex viewing window at the top, through which two copper pipes allow for the flow of methane through the vessel. The vessel is purged thoroughly with methane (CP grade, 99.5%, BOC) and submerged to its brim in liquid nitrogen. As the vessel cools below the boiling curve, methane starts to condense and liquid methane collects. When enough liquid methane has collected, the vessel is opened and the DAC closed before lifting out of the vessel.

Confirmation of successful loading comes from the presence of the methane vibron in its Raman spectrum at around 2,900 cm^{-1} (Hollas 1996) from inside the sample chamber.

4.2. Pressure measurement at high temperature

4.2.1. Ruby crystal

The photoluminescence of ruby crystals (aluminium oxide doped with chromium ions, Cr^{3+}:Al_2O_3) was famously exploited in the building of the first laser, stimulating red laser light at a pair of wavelengths R1 = 694.3 and R2 = 692.9 nm, caused by the excitation of chromium ions within the alumina lattice (Maiman 1960).

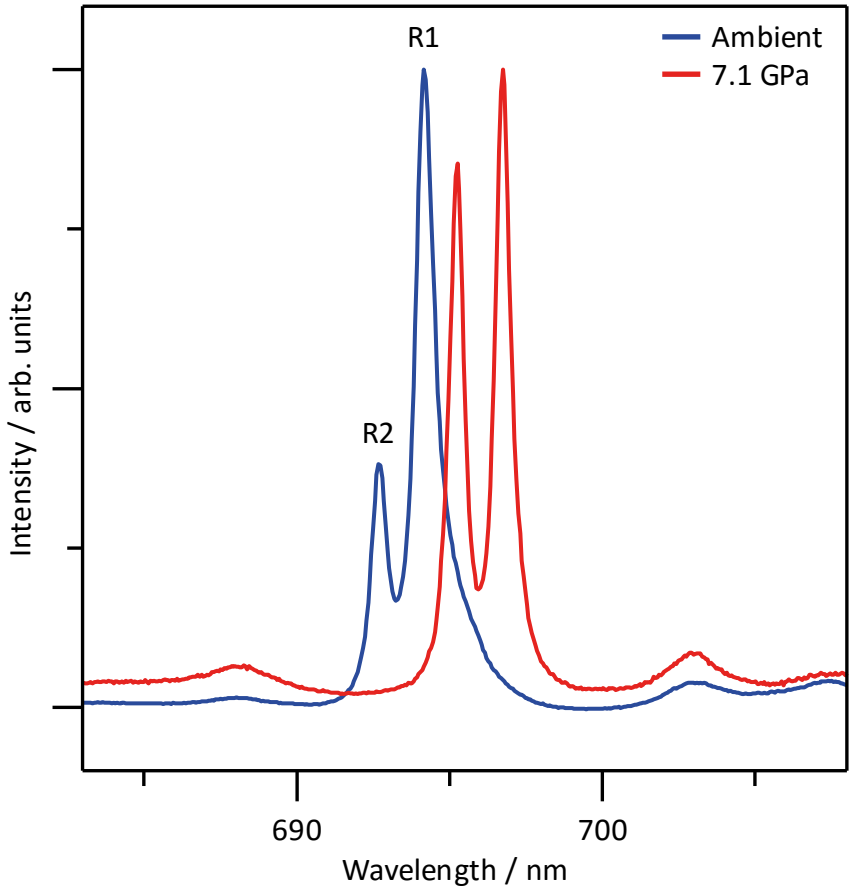

Figure 4.5: Pressure measurement using the photoluminescence spectrum of ruby crystal. (blue) Ambient pressure on a glass slide, (red) 7.1 GPa inside a DAC sample chamber.

Photoluminescence of ruby can be stimulated using focused laser light inside a DAC and, under compression, the redshift of R1 and R2 has been calibrated to provide an accurate scale of the pressure inside a sample chamber (Mao 1986). Meanwhile, the broadening of the peaks can be used as a gauge of hydrostaticity of the pressure inside the chamber (Piermarini 1973). For quasi-hydrostatic compression at room temperature, Mao *et al.* provide a pressure gauge for the R1 line:

$$P\left(\mathrm{GPa}\right)=\frac{A}{B}\left[\left(1+\frac{\Delta \mathrm{R1}}{\mathrm{R1}_0}\right)^B-1\right] \qquad 4.1$$

Where A = 1904 GPa and B = 7.665 (Mao 1986). This calibration has since become widely used in high pressure research – cited 2,034 times in articles recognised by the Thomson Reuters *Web of Science* as of October 2015.

Issues with the ruby fluorescence scale arise when temperature is elevated, however. The broadening and softening of the R1 and R2 peaks limits the use of ruby as a pressure scale at very high temperatures, a problem that has been well-known since the early days of its use (Block 1976), but perhaps the greater problem is the shift in R1 and R2 with changing temperature. A number of corrections to the Mao relationship have been offered which add a temperature-dependent term (Vos 1991, Ragan 1992) to or suggest a correction to the factor A (Rekhi 1999) in equation 4.1, but none are in agreement.

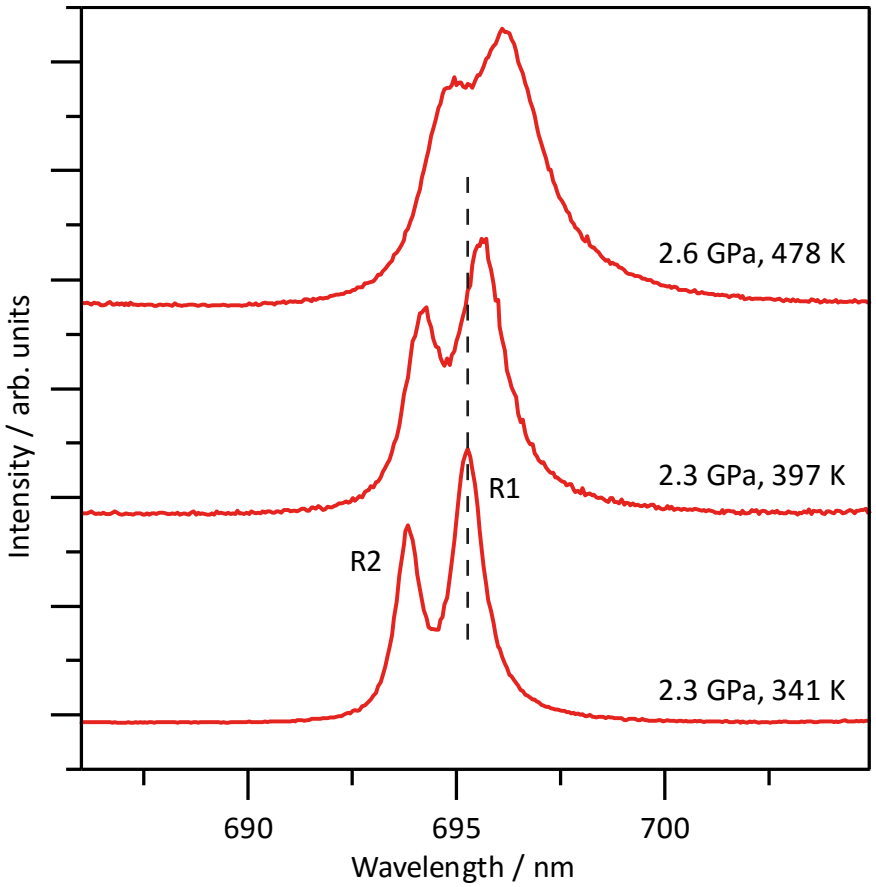

Figure 4.6: Photoluminescence spectra of ruby at upon increasing temperature with pressures shown as calculated after temperature calibration (Rekhi 1999). Dotted line illustrates the shift in ruby peaks with increasing temperature at constant pressure.

Experimental data showing the pressure inside the cell during hydrogenation of graphene in § 5.5 is shown in Figure 4.6. Note that, although the pressure measured inside the cell is the same, with ~50 K increase in temperature we observe a large (0.34 nm) redshift in the position of the R1 peak – comparable to the shift that would be generated by a pressure increase of 1 GPa (0.365 nm, from equation 4.1 at low pressure and (Piermarini 1975)). At higher temperatures still, the peaks become broad, adding another source of uncertainty to the immediate measurement of pressure during an experiment.

4.2.2. Diamond edge

The diamond anvils themselves can be used as a pressure scale, as the stress on the diamond lattice at the point of contact between the culet and the sample chamber (the *edge*) causes a shift of the Raman peak of diamond at 1333 cm^{-1} to higher frequencies. Use of the anvil itself as a pressure scale becomes important at extremely high pressures, where culet and sample chamber size restrict the use of a fluorescent crystal and photoluminescence from ruby crystal diminishes (Bell 1984).

By calibration against the equation of state of platinum to multi-megabar pressures, Akahama *et al.* have provided a relationship between the Raman frequency at the stressed diamond edge and pressure:

$$P\left(\mathrm{GPa}\right) = K_0 \frac{\Delta \mathrm{D}}{\mathrm{D}_0}\left[1 + \frac{1}{2}\left(K_0{}' - 1\right)\frac{\Delta \mathrm{D}}{\mathrm{D}_0}\right] \qquad 4.2$$

Where ΔD denotes the shift in the diamond Raman peak at the edge relative to the D_0 = 1333 cm^{-1} and K_0 and K_0' are 547 and 3.75 GPa respectively for uniaxial strain as is the case for the edge of the diamond anvil (Akahama 2006), while separate K_0 and K_0' values exist for diamond under hydrostatic compression *via* calibration with diamond microcrystals placed inside the sample chamber of the DAC (Kunc 2003, Dubrovinskaia 2010).

An example of diamond edge pressure scale used to a measure pressure inside a sample chamber containing deuterium up to 318 GPa is provided in Figure 4.7a, while Figure 4.7b shows the diamond edge at constant pressure upon cooling (Howie 2013). The temperature dependence of the diamond Raman mode has been explored (Huang 2010) and is small – approximately –0.03 cm^{-1}/K in the explored region.

The study by Huang *et al.* also goes some way towards calibrating the pressure response of the diamond Raman mode with increasing temperature, though pressure inside the chamber was measured using the ruby fluorescence scale, with which there are serious problems at high temperature (§ 4.2.1) and the temperature calibration used is not disclosed. In any case, a pressure scale for use at high temperature comprises two parts: the pressure shift at ambient temperature and the temperature shift at ambient temperature – which are considered to be independent of one another.

In the case of the diamond edge, the laboratory restraints on the resolution of any Raman spectrometer system along the beam axis mean that diamond some distance away from the edge is still excited by the laser and collected with the spectrum – *i.e.* the ambient pressure reference peak and the peak for pressure measurement are collected in the same spectrum (Figure 4.7 and Figure 4.8), negating the need to consider temperature-induced shifting.

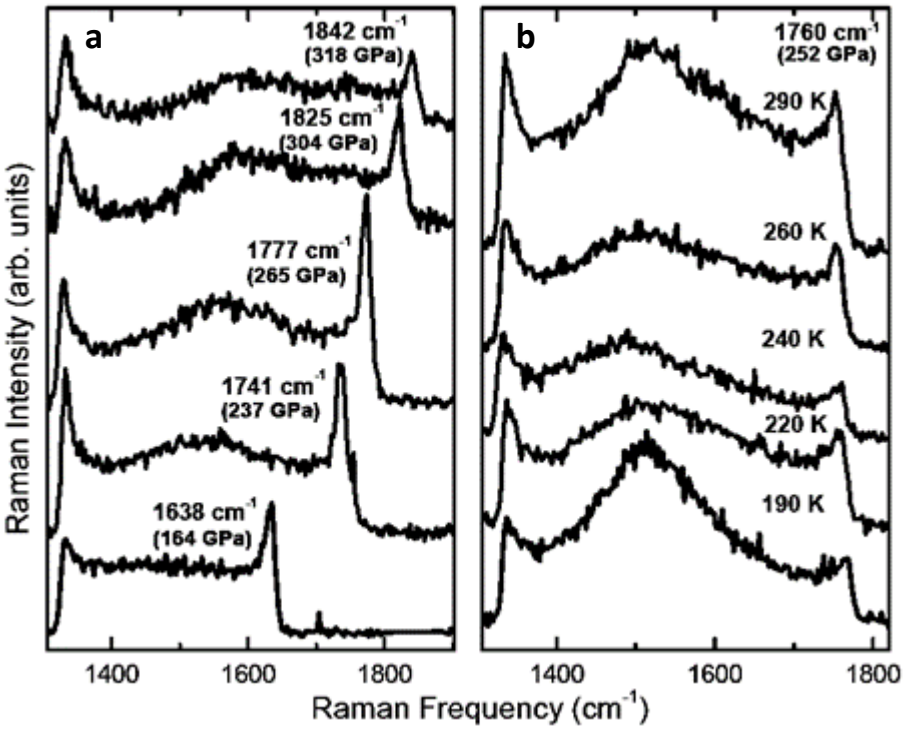

Figure 4.7: (**a**) Measurement of pressure inside a sample chamber containing hydrogen up to 318 GPa using the stressed culet of the diamond in contact with the sample chamber, (**b**) The spectra of the stressed diamond culet at 252 GPa upon cooling to 190 K (Howie 2013).

While pressure measurement with the diamond edge is at a disadvantage since it is not a measurement of pressure based on a material placed inside the sample chamber, one advantage of using the diamond edge to measure pressure inside a sample chamber is that it is possible to observe the stress-induced shifting of the diamond Raman peak at any location across the culet. In any DAC experiment, we expect pressure gradients across the sample chamber as the hydrostaticity of the pressure transmitting medium is altered with increasing pressure (Klotz 2009). The diamond edge splitting can be measured directly at the location of a sample – such as

a flake of graphene on copper in experiments on hydrogenation of graphene – to get a measurement of the pressure, where other pressure calibrants can be some distance away.

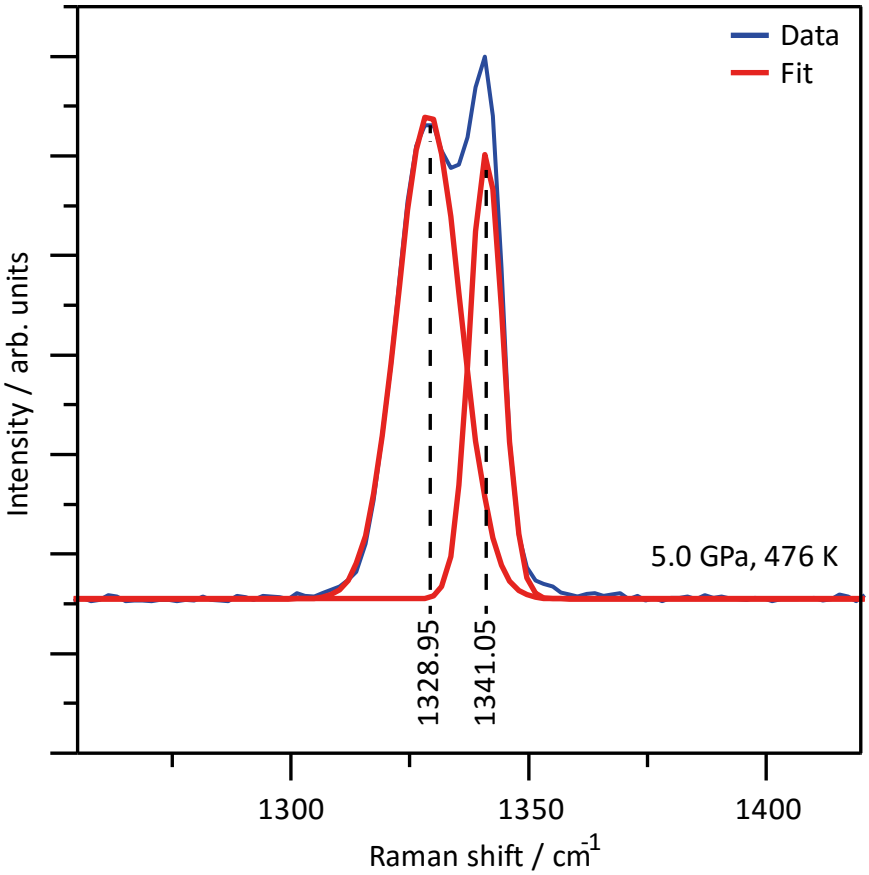

Figure 4.8: Stress-induced splitting of the diamond edge measuring 5.0 GPa at 476 K as determined by the difference in centre positions of two Gaussian curves fitted to the data in the MagicPlot software package.

Figure 4.8 shows the diamond edge splitting in the centre of a sample chamber filled with fluid molecular hydrogen at 476 K during an experiment on hydrogenation of graphene (§ 5.3). Red lines show the data fitted with MagicPlot fitting software as a pair of Gaussian curves with their calculated peak centres marked below the spectrum. According to equation 4.2 (Akahama 2006), the pressure here is 5.0 GPa.

4.2.3. Samarium-doped yttrium aluminium garnet (Sm:YAG)

As a solution to the reduced accuracy in pressure measurements with ruby crystal calibrant at high temperature due to its photoluminescence lines shifting with

temperature, an alternative has been proposed in the form of samarium-doped yttrium aluminium garnet ($Sm:Y_3Al_5O_{12}$, Sm:YAG) crystal. Early experiments on the development of the Sm:YAG pressure scale suggest a pressure response that is comparable to that of ruby and no significant dependence of the photoluminescence peak positions up to temperatures of 820 K (Hess 1992). Figure 4.9 shows the temperature dependence of 10 different Sm:YAG photoluminescence lines up to 982 K with very little shift in the positions of Y1 and Y2 due to temperature – the most common options as a foundation for a pressure scale due to their large intensity. The straight line fits in Figure 4.9 are in good agreement with the experimental data and provide a temperature shift -6.79×10^{-3} nm/K for the Y1 peak and -4.41×10^{-3} nm/K for Y2, two orders of magnitude smaller than the shifts due to pressure – 0.29 nm/GPa and 0.24 nm/GPa respectively in that study (Zhao 1998) and 0.31 nm/GPa and 0.30 nm/GPa in a more recent study (Goncharov 2005).

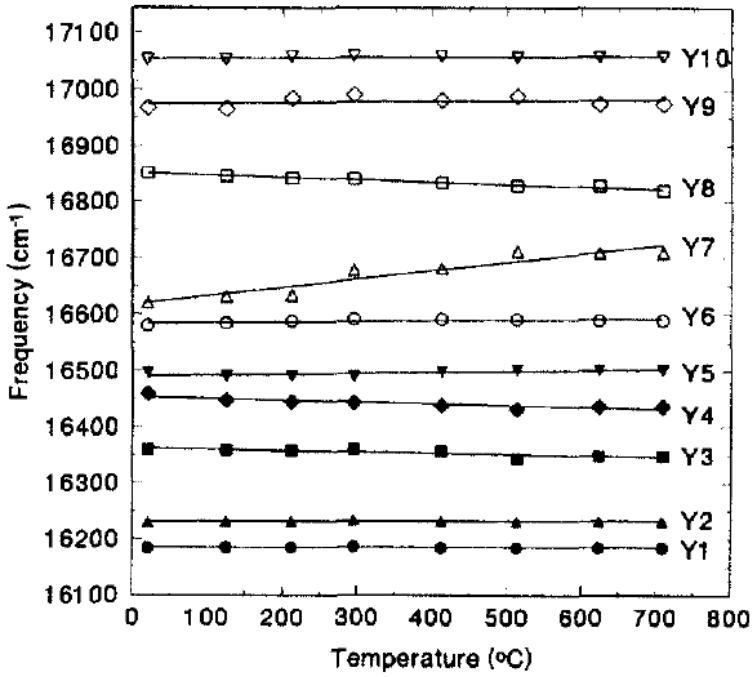

Figure 4.9: Position of 10 Sm:YAG photoluminescence lines up to 982 K at 1 bar pressure by Zhao *et al.*, with almost no frequency dependence on temperature in Y1 or Y2 (Zhao 1998).

Just as the ruby fluorescence pattern changes with hydrostaticity of the pressure transmitter, the Sm:YAG pattern is subject to change upon temperature increase. Notably, at very high pressures, the Y4 and Y1 peaks are seen to split (Trots

2013) and the Y1 peak – which is most prominent at ambient pressure – is seen to greatly soften above 60 GPa (Goncharov 2005), making the Y2 peak a more recommended basis for a pressure scale.

Pressure scales based on Sm:YAG are often linear in form (Hess 1992, Zhao 1998) and this is seen to be valid up to 100 GPa (Goncharov 2005), thus:

$$P\left(\mathrm{GPa}\right) = A\left(\mathrm{Y}X - \mathrm{Y}X_0\right) \qquad 4.3$$

Here, YX and YX_0 are the measured positions of the X Sm:YAG photoluminescence peak under pressure and at ambient pressure respectively, in units of nm. While pressure can be measured using X up to 10 (Zhao 1998), Goncharov *et al.* suggest calibrations based on X up to 4, giving A coefficients of 3.175, 3.29, and 3.03 for the Y1, Y2 and Y3 peaks – which we use most frequently (Goncharov 2005).

While the Sm:YAG photoluminescence peaks are not subject to the shift in temperature that is observed in the ruby peaks, they do still exhibit significant broadening (Zhao 1998, Wei 2011). The peaks begin to broaden after 373 K (Figure 4.10) and quick and accurate pressure measurement during an experiment becomes difficult. During experiments it is beneficial to use the Y3 scale wherever possible since it is sufficiently separated from Y1 and Y2, but still displays a large shift in pressure compared with the more prominent Y4 (Goncharov 2005), however it is not sharp at ambient conditions and suffers further broadening at elevated temperature.

As an alternative, for fast measurements during high temperature experiments, we can employ the "Y1.5" pressure scale which uses the centre of the broad peak caused by the overlapping Y1 and Y2 peaks and an A value of 3.2325 in equation 4.3 – the average of the Y1 and Y2 A values.

When exciting Sm:YAG *in situ* in a DAC, blue laser light must be employed. While the green laser light has sufficient photon energy to excite photoluminescence from the material, the second-order diamond peak when diamond is excited with a green laser falls in the same location as the Sm:YAG lines – complicating the determination of their position and thus the pressure. A simple modification to the spectroscopy equipment is made, introducing a 405 nm solid state laser, directed towards the objective lens *via* a 50-50 beam splitter (Figure 3.11).

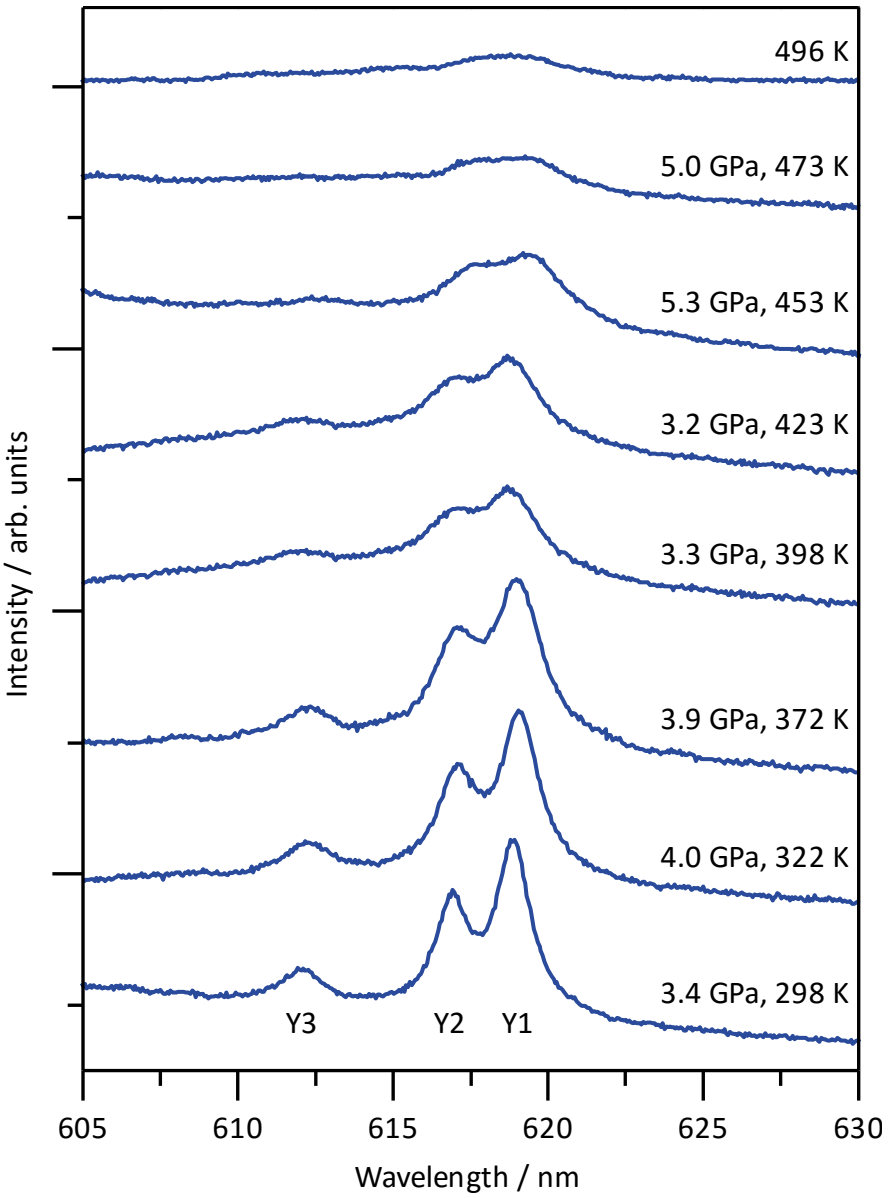

Figure 4.10: Devolution of Sm:YAG photoluminescence spectrum on temperature increase until complete signal loss at high temperature. Broadening becomes significant after 373 K. Spectra are fitted with Lorentzian functions in MagicPlot fitting software up to 473 K. Spectrum at 496 K was unable to be confidently fit with peak functions due to loss of photoluminescence signal.

Contrary to claims that Sm:YAG peaks can be resolved easily up to 1,000 K (Zhao 1998), a recurring issue with Sm:YAG crystals is that of the photoluminescence peaks disappearing at sample-dependent, arbitrary high temperatures. Figure 4.10 shows the evolution of the Sm:YAG photoluminescence spectrum upon heating, with significant broadening between 373 K and 473 K and the signal ultimately disappearing into the background at 496 K. In all cases where the signal is lost at high

temperature, it is not recovered upon cooling below the arbitrary temperature at which it disappears, and does not begin to return until temperatures approach ambient.

Unlike ruby, Sm:YAG crystals are not widely commercially available and are most frequently purpose-grown for high pressure experiments. Without having being subject to the decades of development and quality control that is the case with ruby crystal, there is the potential that the crystals used in our experiments, grown by the Czochralski process and provided by Trots *et al.* (Trots 2013 and supplementary information) are of fairly low quality, and that some of the Sm^{3+} ions in the crystal are sitting in interstitial sites on the lattice rather than replacing yttrium ions. If this were true, it is conceivable that with enough thermal energy, Sm^{3+} ions could begin to diffuse out of the crystal, leaving only those ions which form part of the lattice available to provide photoluminescence – which would be broad at high temperature, but more pronounced once the crystal returns to room temperature. In their study presenting the crystals, Trots *et al.* use laser ablation inductively coupled plasma-mass spectrometry (ICP-MS) to determine the stoichiometry as $Y_{2.71}Sm_{0.29}Al_5O_{12}$. It would be interesting to directly measure the Sm^{3+} content before and after an experiment at high temperature.

Chapter 5. Hydrogenation of graphene at high pressure and temperature

5.1. Hydrogenation at 6.5 GPa and 493 K

Figure 5.1 shows graphene on a copper substrate in an atmosphere of solid hydrogen at 6.5 GPa, with a sufficient border of hydrogen around the sample.

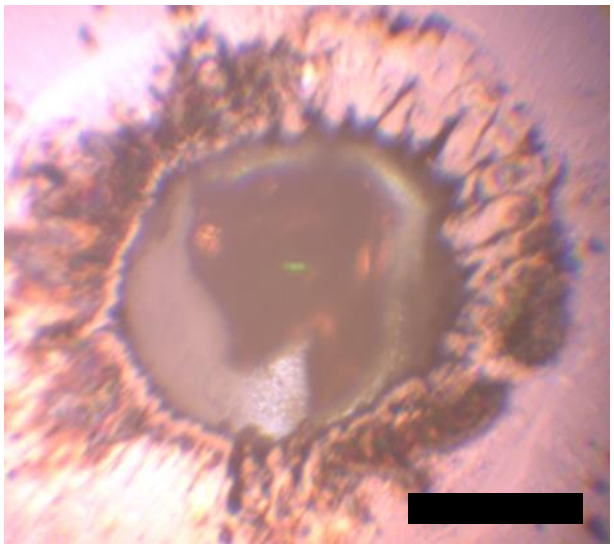

Figure 5.1: Optical micrograph showing a copper flake coated with CVD-grown graphene surrounded by solid hydrogen at 298 K. Scale bar is 100 μm.

Whilst maintaining this pressure by observation of the splitting of the diamond anvil Raman peak at the culet, the sample was heated to a maximum of 493 K. This temperature was maintained until the sample chamber had collapsed significantly around the sample – a total of around 10 minutes, at which point the

temperature was gradually reduced with pressure maintained constant, before the pressure was released at ambient temperature.

It is important not to release pressure at elevated temperatures to avoid the accidental removal of any hydrogen bonded to the lattice following the observations that hydrogen can be thermally annealed from hydrogenated graphene at temperatures starting as low as 75°C (348 K) under vacuum conditions (Luo 2009) – pressure was thus released at ambient temperature. Similarly, a study has shown that pristine graphene can be denatured using photons with even modest laser power focused to a diffraction-limited point (Krauss 2009). Although the effects documented by Krauss *et al.* take place over a number of hours, laser-induced denaturing is a factor which should be considered when performing Raman spectroscopy on samples, taking care not to accidentally damage graphene or hydrogenated graphene samples, or to anneal away hydrogen with the laser on hydrogenated samples.

The resulting Raman spectra from the high pressure high temperature hydrogen treatment of graphene are presented in Figure 5.2. Similarly to reports on graphene hydrogenated by the atomic hydrogen method (Elias 2009), the D peak intensity is seen to vary greatly across the sample.

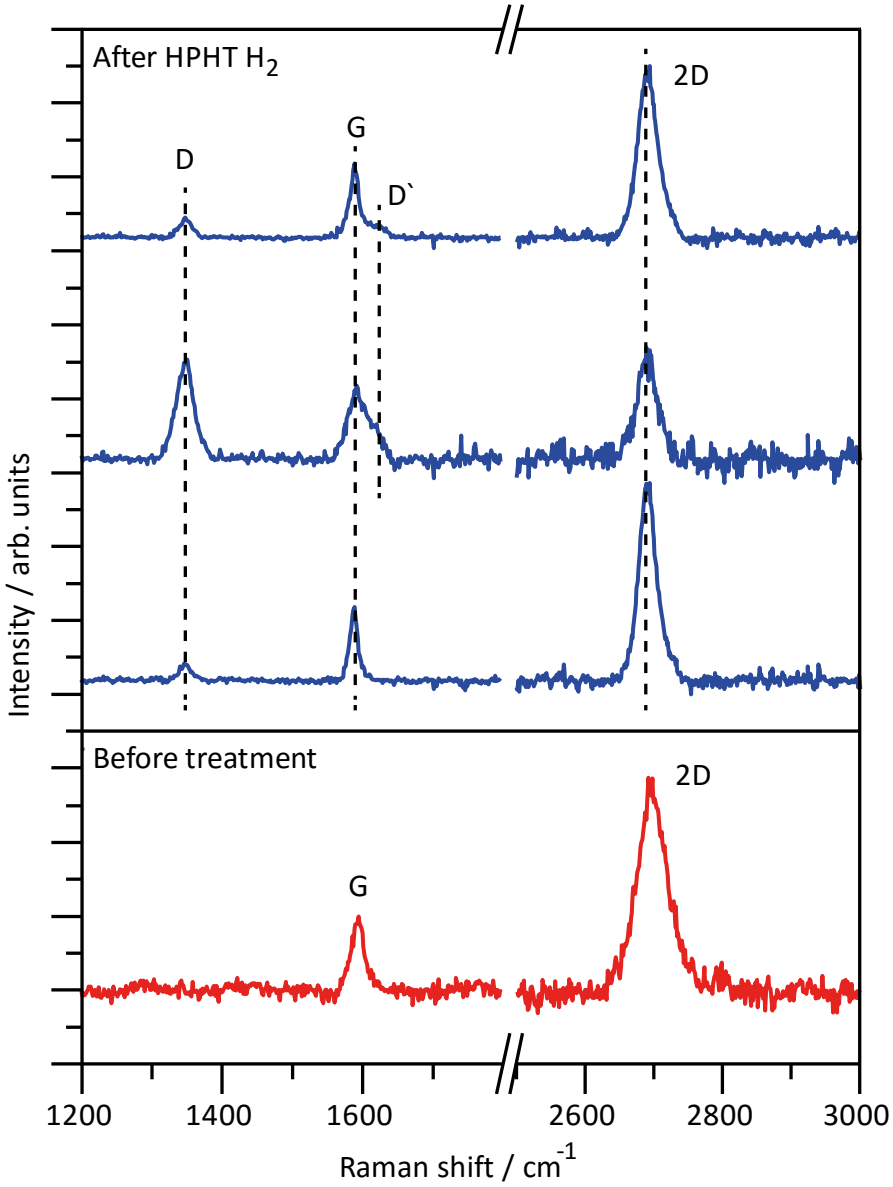

Figure 5.2: Changes in the Raman spectra of a graphene sample exposed to fluid molecular hydrogen at 6.5 GPa and 493 K for ~10 minutes. (bottom, red) Raman spectrum before the treatment, showing no measurable D peak activity. (top, blue) Raman spectrum at a number of sites across the sample after exposure, showing development of the defect peaks with varying intensity. All spectra are normalised to the G peak intensity.

In order to measure the I_D/I_G ratio to quantitatively compare the hydrogenation with the literature, the Raman spectra were fitted with peak functions using MagicPlot Student 2.5.1. It was found in all cases that after subtraction in OriginPro 9.0 to remove the background due to the copper substrate that the peaks fitted well with Gaussian functions (In Figure 5.3, R^2 close to 1, implying a good fit).

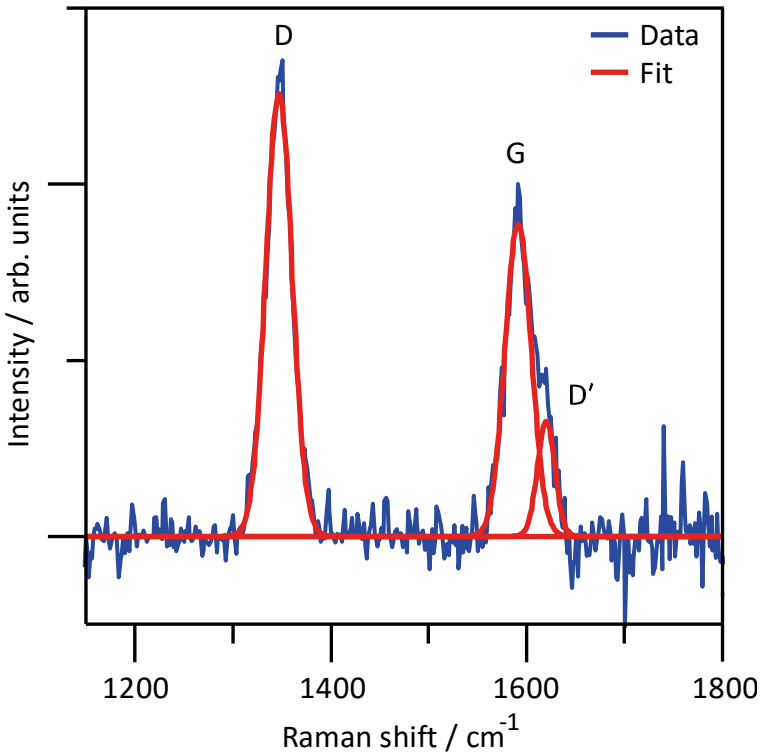

Figure 5.3: Gaussian curves fitted to the G and D and D' defect peaks in the Raman spectrum of the of the area the hydrogenated sample shown in Figure 5.2 exhibiting the most intense D peak – *i.e.* the most hydrogenated area.

In the case of the area exhibiting the most intense D peak from the hydrogenated sample, the I_D/I_G determined from the Gaussian height values after fitting in MagicPlot was 1.4 (L_D = 11.97 nm, 514 nm excitation), suggesting that only low levels of hydrogenation have been achieved across the sample.

5.2. Deuteration of graphene at 6.5 GPa and 473 K

A sample of graphene on copper was prepared in an environment of molecular deuterium *via* high pressure gas loading. The motivation behind loading into and reacting with deuterium is that its melting curve is lower than that of hydrogen (Caillabet 2011), allowing an investigation into whether having the reagent and pressure transmitting medium (PTM) further into the fluid state would influence the rate of the reaction.

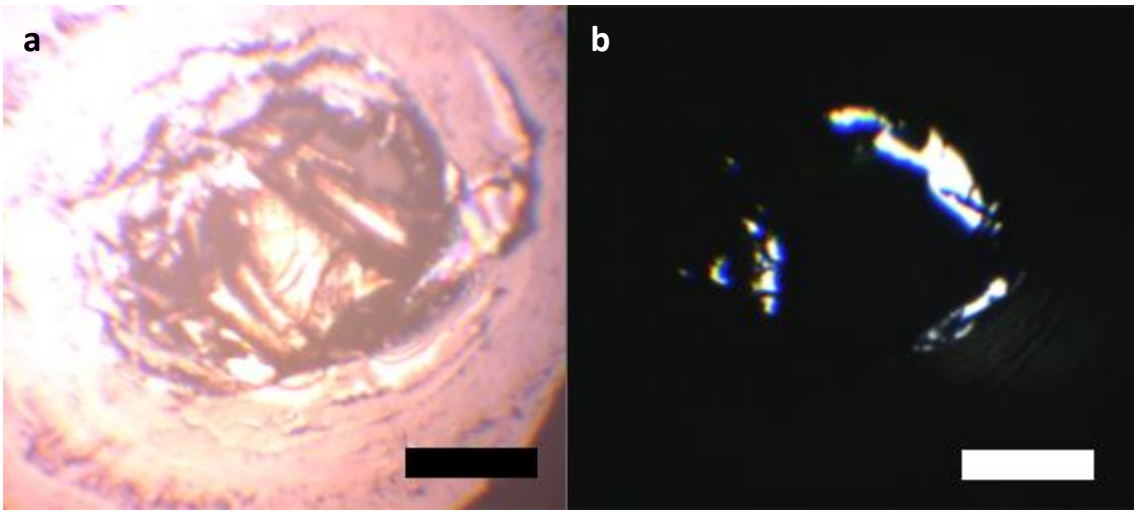

Figure 5.4: Optical micrographs of graphene on copper substrate in fluid deuterium at 6.5 GPa and 443 K. (**a**) Front lighting only, (**b**) back lighting only, illustrating presence of deuterium between the sample and gasket. Scales bar are 100 μm.

As in § 5.1, graphene in deuterium was compressed to 6.5 GPa with reference to the splitting of the diamond Raman peak at the culet. Pressure was maintained up to 473 K and this temperature was maintained until the border of deuterium around the sample (Figure 5.4) was observed to almost disappear before cooling to ambient temperature – the time spent at the nominal conditions was once again around 10 minutes.

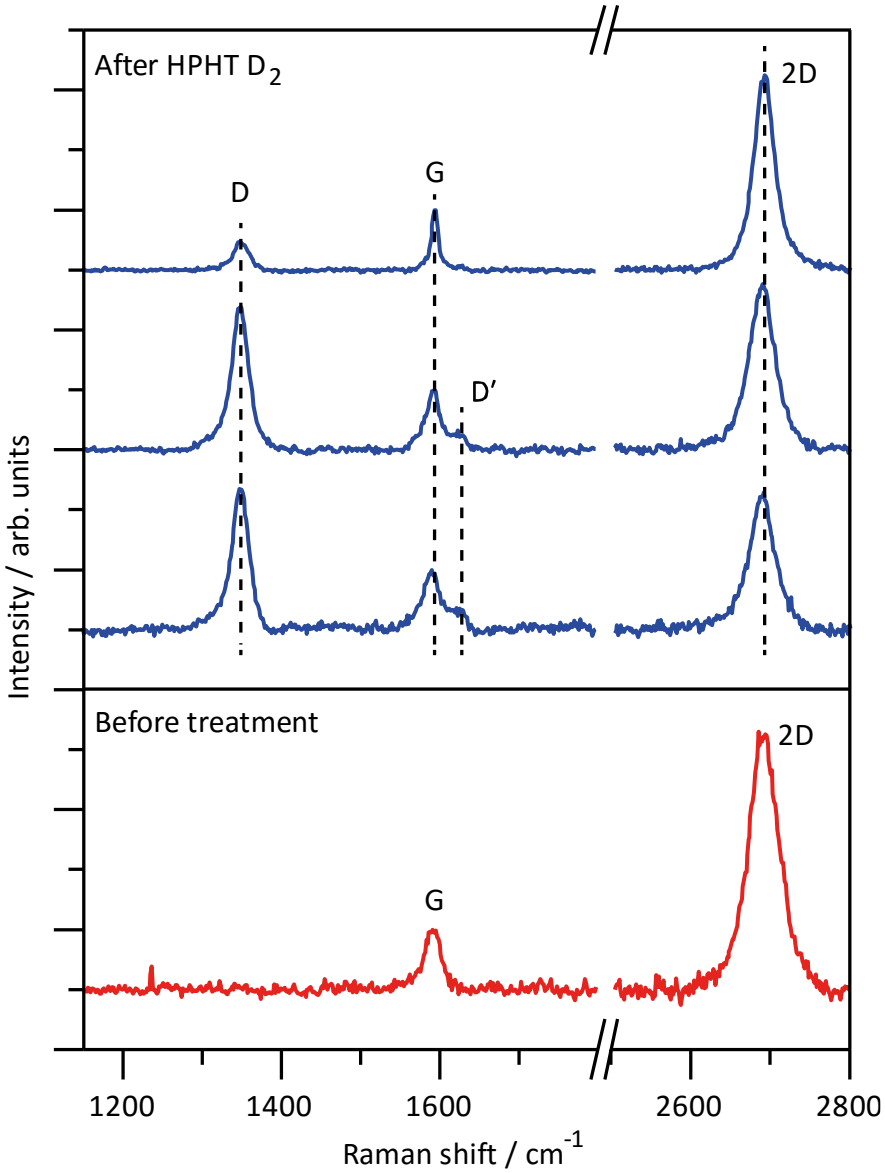

Figure 5.5: Change in Raman spectrum from pristine (red) to functionalised (blue) after 10 minutes of exposure of graphene to fluid deuterium at 6.5 GPa and 473 K.

Observation of the sample after retrieval show the D and D' peak in the Raman spectrum with varying intensity in different locations. In the most intense location, a fit with Gaussians functions in MagicPlot reveals an I_D/I_G value of 2.5 – equivalent to L_D = 6.70 (using 514 nm excitation) – shown in Figure 5.6. The deuterated sample is modified to a level that is comparable to the hydrogenated samples produced by Elias *et al.* using graphene membranes exposed to atomised hydrogen on both sides of the lattice for 2 hours (Elias 2009), while only allowing molecular deuterium access to one side of the lattice for around 10 minutes.

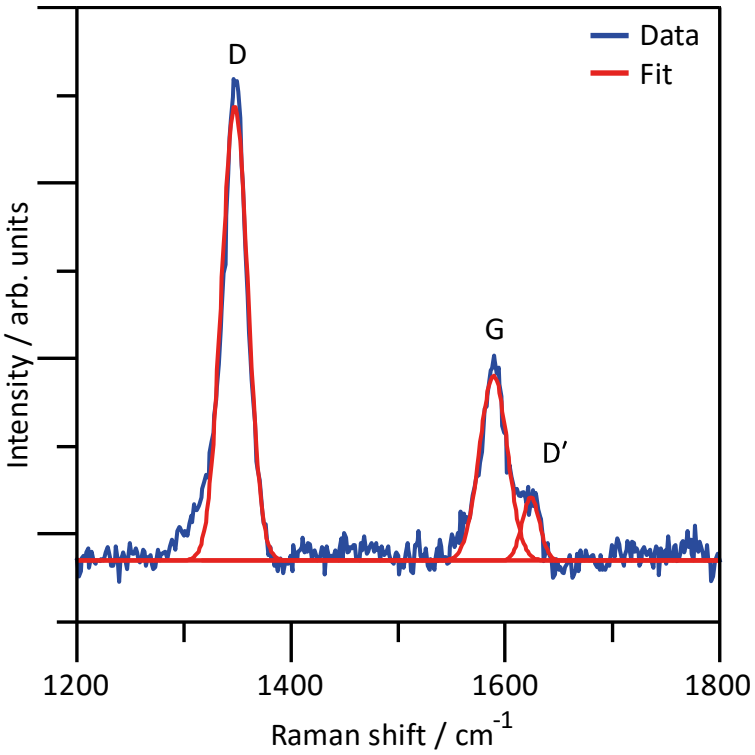

Figure 5.6: Gaussian peak functions fitted to the location in Figure 5.5 exhibiting the strongest defect peaks. MagicPlot reports for the fitted peaks allow calculation of the intensity ratio I_D/I_G = 2.5.

5.2.1. Long-term stability of deuterated graphene

Regarding the stability of functionalised graphene, the deuterated sample was left untouched in the lab for some 5 months. Figure 5.7 shows the Raman spectrum of graphene deuterated in a diamond anvil cell immediately after the treatment, exhibiting I_D/I_G = 2.5 (Figure 5.6), compared with the Raman spectrum in the same location after 5 months.

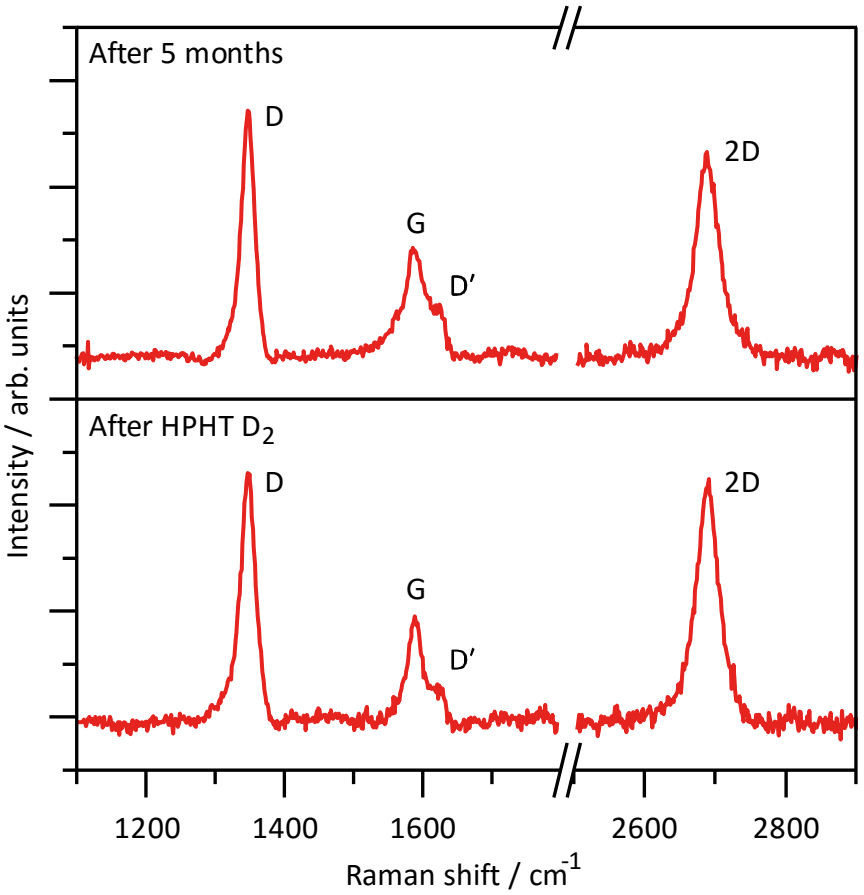

Figure 5.7: The Raman spectrum of deuterated graphene immediately after deuterium treatment (bottom) and 5 months after deuterium treatment (top) in the same location on the sample. The intensity of the defect-induced D and D' peaks has not reduced in this time (I_D/I_G = 2.5 in both spectra).

The D and D' peaks are still visible in the Raman spectra – collected as close to the original locations as possible – after 5 months. Immediate inspection of the spectrum allows confirmation that deuterium has remained bonded to the graphene lattice, and the I_D/I_G value of the most deuterated location is still 2.5, as it was when measured immediately after the high pressure high temperature treatment. This suggests that functionalised graphene samples prepared by the DAC method are stable for extended time periods.

5.3. Hydrogenation at 5.0 GPa and 473 K

Figure 5.8 shows the resulting Raman spectrum at several locations across the sample after hydrogen treatment at 473 K and 5.0 GPa – measured using the stress-induced splitting of the diamond Raman peak at the culet – for roughly 10 minutes. As before, the intensity of the D peak, *i.e.* the extent of hydrogenation, varies greatly across the sample.

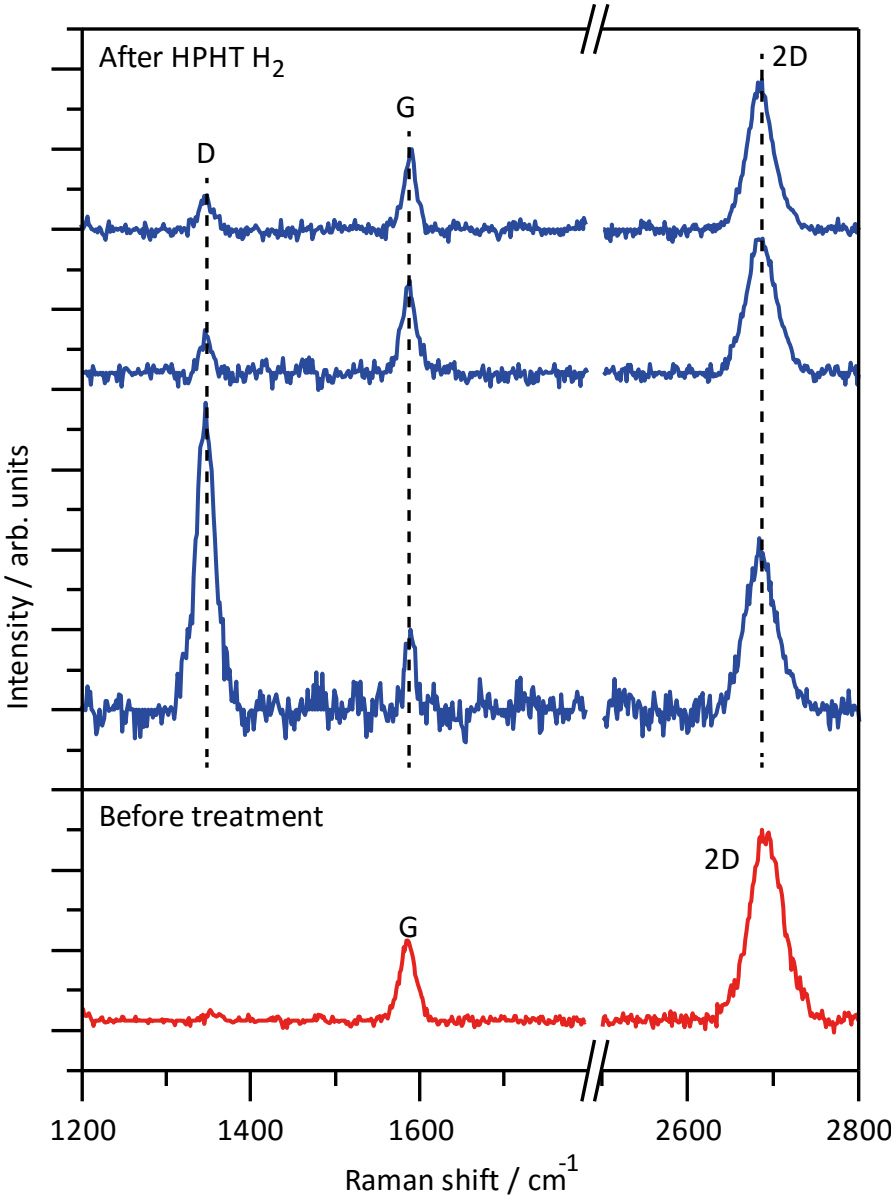

Figure 5.8: Several locations on graphene sample treated with fluid molecular hydrogen at 5.0 GPa and 473 K exhibiting D peak with varying intensity (blue) compared with no D peak activity in pristine graphene before treatment (red).

As before, the peaks have been fitted with Gaussian curves (Figure 5.9) in order to determine their relative intensities. In the location with the most intense D peak, the I_D/I_G ratio is 3.7, which equates to a spacing of L_D = 5.20 nm between hydrogenated sites – close to the Stage II transition (Figure 3.7).

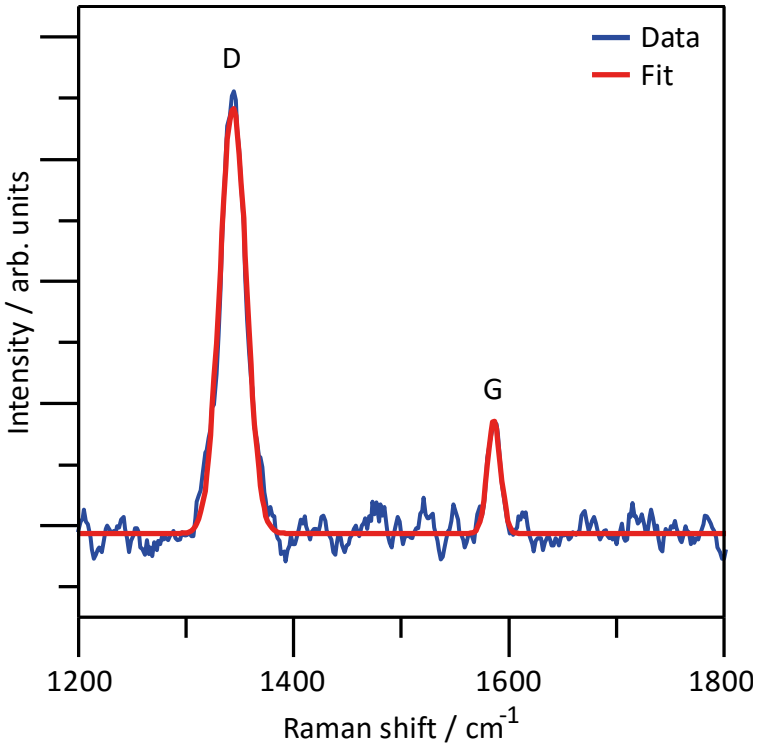

Figure 5.9: Gaussian functions fitted in MagicPlot to the D and G peaks for the most hydrogenated location of graphene sample treated at 5.0 GPa and 473 K in hydrogen.

In addition, the Raman spectrum of the highly hydrogenated area shown in Figure 5.9 was collected 33 days after the treatment at high pressure and high temperature – suggesting long-term stability of hydrogenated graphene even at higher levels of hydrogenation.

5.4. Thermal annealing of hydrogenated and deuterated graphene

Following the protocol set by Elias *et al.* (Elias 2009), we aim to test that the D peak had been activated in the Raman spectra of our graphene samples after hydrogen

treatment at high pressure and temperature due to hydrogen forming covalent bonds with the carbon atoms in the graphene – partially converting the bonding nature to become sp^3-like in those sites – and not simply due to structural damage of the graphene caused by physical disruption during the experiment, by subsequently removing the hydrogen from the graphene using a mild thermal annealing.

As Elias *et al.* used 450°C in an inert atmosphere of argon (Elias 2009), but Luo *et al.* have reported thermal annealing of their hydrogenated samples as low commencing at temperatures as 348 K in a vacuum, with total removal of hydrogen achieved by 350°C (Luo 2009), we opted for an easily-achievable temperature of 200°C in an inert atmosphere of nitrogen for extended periods of time to ensure a complete anneal whilst remaining sufficiently below the graphitisation temperature of carbon (Figure 2.6). The hydrogenated graphene sample produced in § 5.1 was placed on a Stuart US150 hotplate inside a Saffron Beta glovebox, pumped with nitrogen to have a dry environment with 3 ppm oxygen. The hotplate was set to 473 K – measured with a thermocouple fixed on its surface – and the sample left overnight on the plate. The resulting Raman spectrum resembled that of disordered carbon (Ferrari 2000), suggesting a burning of the sample under these conditions.

In order to find a more inert atmosphere to ensure a successful annealing, heating experiments were performed at 2×10^{-7} mbar with colleagues at Manchester Metropolitan University's Dalton Research Institute (now University of Huddersfield) in the vacuum chamber of a Zeiss Supra VP 40 scanning electron microscope (SEM) modified to facilitate *in situ* Raman spectroscopy. The deuterated sample from § 5.2 was placed inside the SEM chamber and heated to 423 K for 5 hours, and its Raman spectrum after heating once again suggested damage caused by the environment.

After continued failure of the annealing attempts, arrangements were made with University of Manchester to load hydrogenated samples into a scanning tunnelling microscope (STM) capable of capturing atomic resolution images of graphene (Zan 2012). The STM vacuum chamber is pumped to a normal working pressure of 3×10^{-10} mbar and its tantalum stage can be illuminated from behind with radiation from a tungsten filament to heat the sample. Feedback from a type K thermocouple is used to maintain constant temperature.

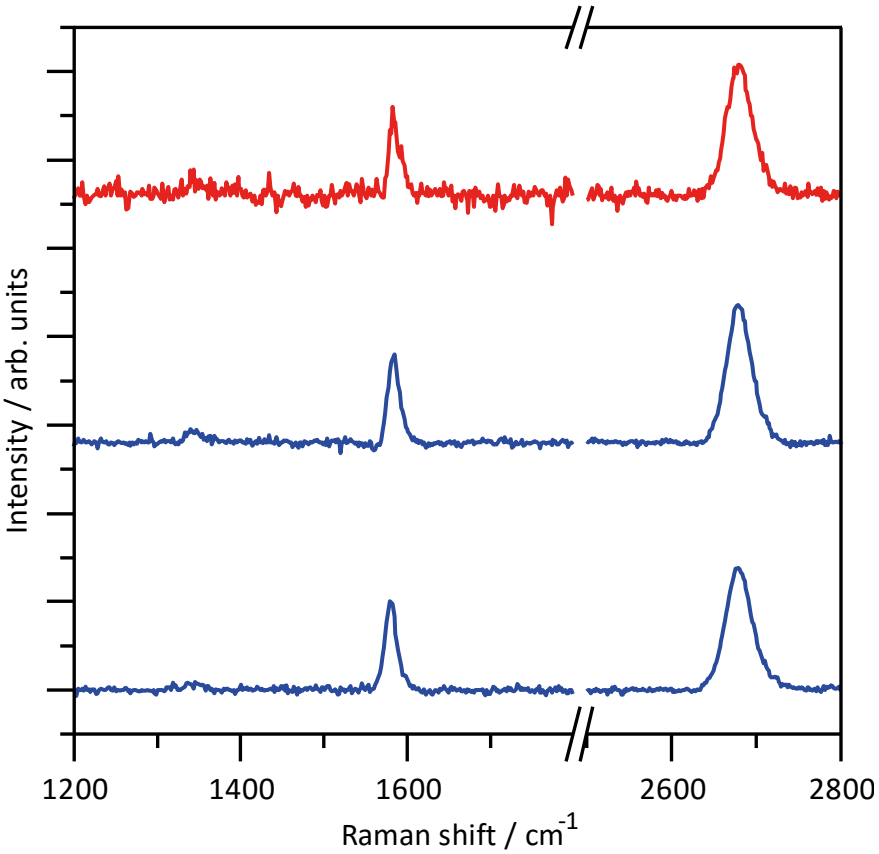

Figure 5.10: Raman spectrum of graphene sample hydrogenated at 5.0 GPa and 473 K in fluid molecular hydrogen (§ 5.3) after thermal annealing at 3×10^{-10} mbar at 473 K. Red spectrum is the location on the sample that had previously exhibited high Stage I hydrogenation (I_D/I_G = 3.7).

The hydrogenated sample from § 5.3 was left overnight at 473 K in ultra-high vacuum conditions. Figure 5.10 shows the resulting Raman spectrum of annealed graphene. After inspection *via* Raman spectroscopy on both sides of the copper substrate, no areas were found exhibiting a sizeable D peak, and the hydrogenated area which had previously shown I_D/I_G = 3.7 was seen to exhibit no D peak activity.

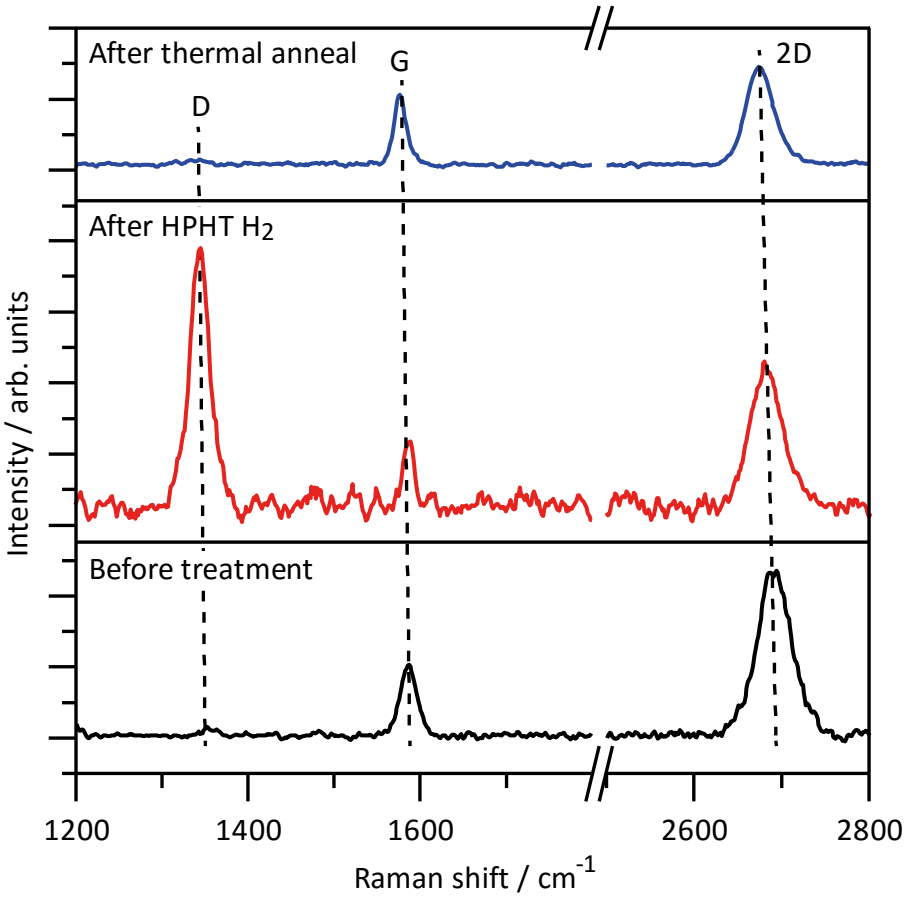

Figure 5.11: Evolution of the Raman spectrum of graphene subjected to fluid molecular hydrogen at 5.0 GPa and 473 K, first pristine after CVD growth (black spectrum), then exhibiting high Stage I hydrogenation (red spectrum) and ultimately returning to pristine graphene with mild thermal annealing (blue spectrum).

We thus prove the hydrogenation of monolayer graphene in the same manner as other authors (Elias 2009, Luo 2009): by removing hydrogen from the sample by thermal annealing at temperatures far below the graphitisation temperature of carbon (Saito 2004), *i.e.* temperatures which are not sufficient to remove the D peak from the Raman spectrum of graphene were it caused by structural damage.

In addition, when preparing pristine graphene samples for preliminary annealing attempts inside the SEM and STM chambers, it was found to be convenient to deliberately mount samples in a stainless steel gasket to improve thermal contact and greatly simplify handling. Mounting was achieved by placing the sample inside the DAC in air and closing the cell while viewing the sample chamber under a microscope, applying enough force to the diamonds so as to have the walls of the sample chamber collapse onto the edges of the copper flake. Subsequent investigation with Raman

spectroscopy shows no change in the spectrum of the graphene away from the edges of the sample. This strengthens the argument that the D peak in high pressure and temperature samples has been caused by adding hydrogen to the graphene and not caused by structural damage to the graphene during experiments – since during experiments, the contact with the collapsing gasket is comparable to the contact during deliberate mounting and often avoided altogether.

5.5. Influence of pressure on graphene-hydrogen reaction at 473 K

It is important to observe the effects of changing pressure on the reaction between graphene and hydrogen, as pressure requirements are intrinsically linked to the maximum sample size. Should it be possible to get high levels of hydrogenation at lower pressure, diamonds with larger culets could be employed to allow for more sample space – in this way, it may be possible to prepare samples on a variety of substrates including thin silicon, allowing electronic measurements of samples to be made.

By employing diamonds with a 1 mm culet for larger control over pressure at lower pressure levels, samples of graphene on copper were loaded in an atmosphere of hydrogen and compressed to 2.6 GPa. The larger chamber compared with the sample size allowed high pressure and temperature conditions to be maintained for 1 hour – allowing exposure of the graphene to hydrogen at the nominal conditions for a longer time than the usual 10–15 minutes. After 1 hour of exposure, the graphene sample was recovered onto a glass slide – *i.e.* the sample chamber had not collapsed around the copper flake so as to mount it inside the steel gasket.

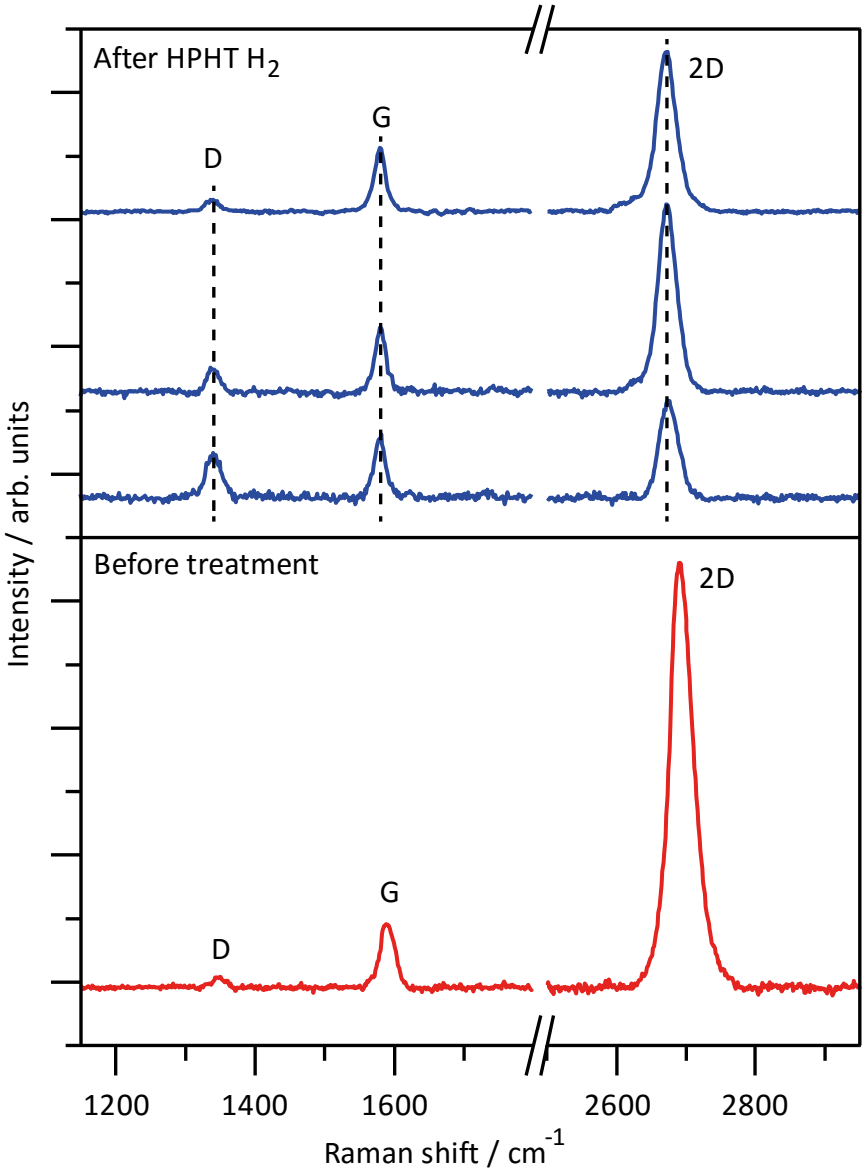

Figure 5.12: Raman spectra of sample treated in hydrogen at 2.6 GPa and 473K for 1 hour, showing small D peak enhancement after treatment (blue spectra) compared with small D peak in before spectrum (red).

Subsequent Raman spectra are shown in Figure 5.12. Areas exhibiting hydrogenation at 2.6 GPa and 473 K are sparse – across both sides of the ~200 μm copper flake, only one location was able to be found that had significant D peak activity. The intensity of the D peak in this location is only 0.7 times that of the G peak, suggesting very low levels of hydrogenation compared with experiments at higher pressure, a spacing L_D = 27.46 nm between defects (in this case hydrogenated sites) on the lattice. The enhanced D peak is considered to come from hydrogenation alone and not physical damage to the lattice as in this case the graphene sample did not come

into contact with sample chamber edges which could cause damage – even in procedures where graphene was deliberately brought to sufficient contact with a collapsing sample chamber so as to fix it in place (as in § 5.4), no enhancement of the D peak was observed.

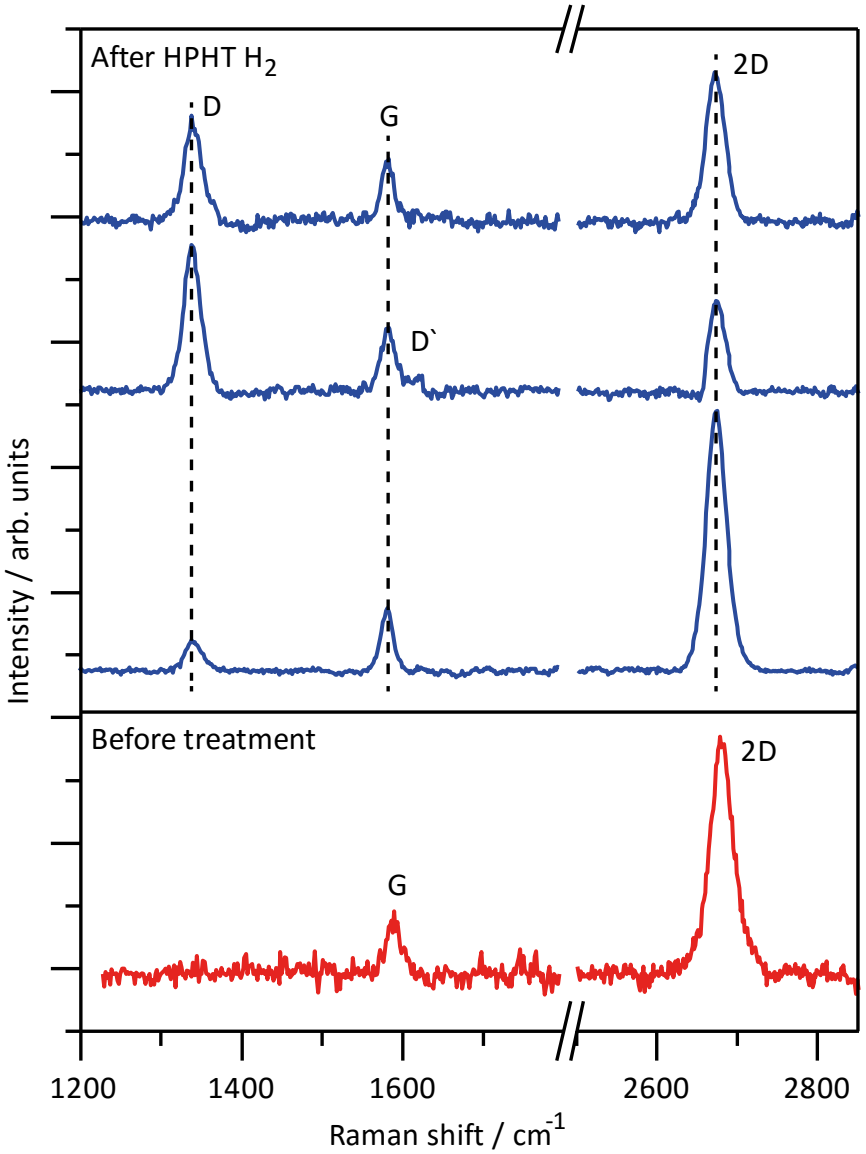

Figure 5.13: Raman spectrum at several locations of sample treated with hydrogen at 4.0 GPa and 473 K. (red) Before treatment, (blue) after treatment with significant D peak enhancement.

Upon increasing pressure to 4.0 GPa, we observe two improvements in the hydrogenation. Firstly, hydrogenation was seen at almost all locations across the sample and secondly, the highest recorded I_D/I_G ratio was 2.3 – or L_D = 8.36 nm. These

results suggest that while activation of hydrogenation may occur as low as 2.6 GPa, the favourability of the reaction is greatly enhanced with further pressure.

Upon reflection of the argument in § 2.3 which discusses the low dissociation energy of C-H bonds in partially-hydrogenated graphene, this result is intuitive. Graphene, especially when grown by CVD on copper substrates, has a complicated long-range structure containing curvature and kinks – *i.e.* a large variation in η. Owing that high-η areas on the lattice already more closely resemble sp^3 in their bonding, it follows that they should be the first locations to accept hydrogenation and that a higher pressure should be required for hydrogenation to occur in low-η areas where the bonding more closely resembles sp^2.

5.6. Influence of temperature on graphene-hydrogen reactions at high pressure

To map out the graphene-hydrogen reaction in P-T space, experiments were carried out in hydrogen and deuterium at ambient temperature and high pressure. Graphene on copper was loaded into the room-temperature DAC (Figure 4.2) in an atmosphere of hydrogen or deuterium into the solid phase at high temperature and left for some time at ambient pressure.

The Raman spectra of graphene after pressure release are shown in Figure 5.14. Graphene pressurised to 7.4 GPa at ambient temperature in hydrogen – a pressure comparable to that used in §§ 5.1 and 5.2 to achieve hydrogenation or deuteration – does not develop a significant D peak after 4 hours in these conditions.

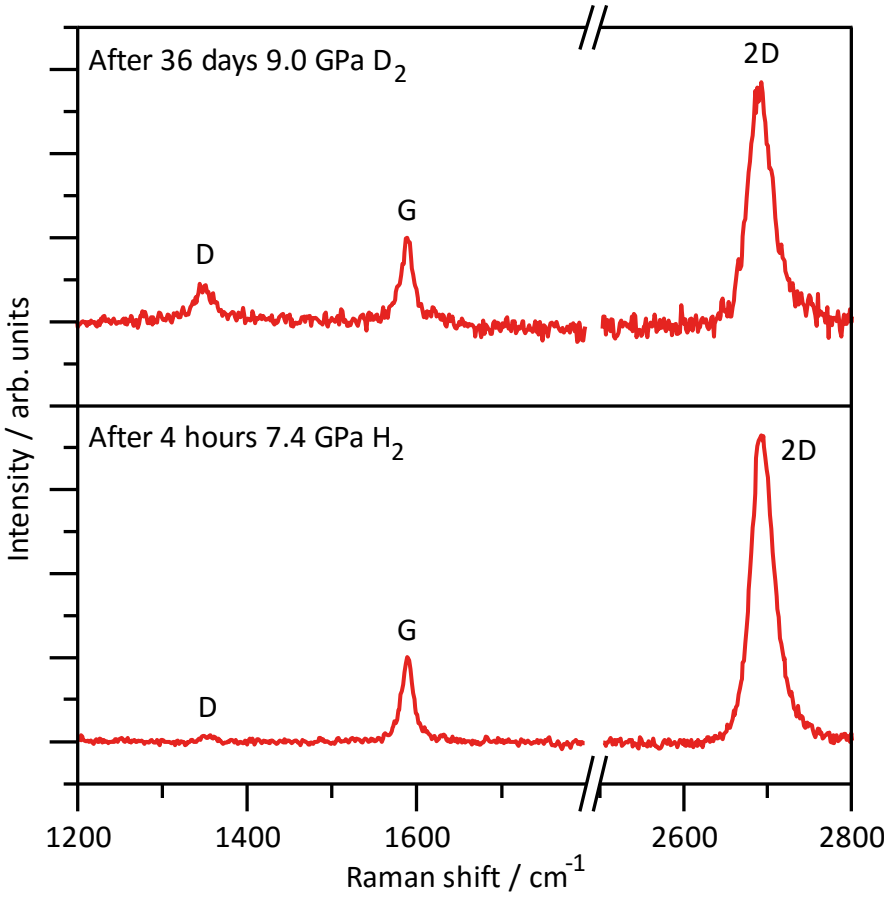

Figure 5.14: Raman spectrum of graphene after pressure treatment at 298 K. (bottom) 4 hours in hydrogen at 7.4 GPa showing almost zero D peak activity. (top) 36 days in deuterium showing small D peak.

There is a measurable D peak in graphene pressurised to 9.0 GPa in deuterium after 36 days in these conditions – the I_D/I_G measured by fitting Gaussian functions to the peaks is 0.4. Such a small D peak is difficult to attribute to deuteration since, in some cases, a D peak of this magnitude is inherently visible in a graphene sample grown by CVD (Riikonen 2013). However, if deuteration has occurred over this time period at ambient pressure, it is insignificant when compared with the levels achieved in § 5.2 under more modest pressure conditions in only 10 minutes. It may suggest that at significantly higher pressures, we may see this rate increase, but to press beyond 9.0 GP would require diamonds with smaller culets, drastically reducing the possible sample size.

Chapter 6. The Frenkel line in supercritical methane

6.1. The Frenkel Line

A new microscopic model for liquids has been formulated by considering particle motion in a liquid to be a duality of solid-like vibrations around fixed sites and gas-like diffusion between those sites, and then by the introduction of a *liquid relaxation time*, τ (Frenkel 1946, Brazhkin 2012). Physically, τ describes the average time between consecutive jumps between the fixed sites, separated on average by a distance a.

Immediately, then, it can be deduced that if one is to observe a liquid for a time t which is shorter than the liquid relaxation time τ, the particles in the liquid would not jump between fixed sites and the liquid would appear as if it were a solid. It follows that for all frequencies ω which correspond to $t < \tau$, a liquid is capable of supporting shear waves as does a solid (Brazhkin 2012). Comparing with the maximum vibrational frequency available to the particles, the Debye frequency, ω_D, gives an effective range:

$$\frac{2\pi}{\tau} < \omega < \frac{2\pi}{\tau_D} \qquad 6.1$$

over which a liquid can support shear waves. Here τ_D is the time period related to the Debye frequency. The zero shear resistance of liquids at low frequencies is responsible for their ability to flow. Providing particles in a liquid with more thermal energy by increasing temperature increases the number of jumps made, *i.e.* reduces τ.

This reduces the range defined by equation 6.1 over which a liquid is "solid-like", or rigid, until:

$$\tau = \tau_D \qquad 6.2$$

At which point, the liquid is no longer able to support shear waves at any frequency (Brazhkin 2012), we can consider the liquid to be entirely "gas-like" or a non-rigid fluid. Increasing pressure on a liquid moves its particles closer together, thereby increasing the Debye frequency (Baierlein 1999) and increasing the temperature requirement to satisfy 6.2, tracing out a *Frenkel line* on the phase diagram in pressure-temperature space, as seen in Figure 6.1 (Brazhkin 2012).

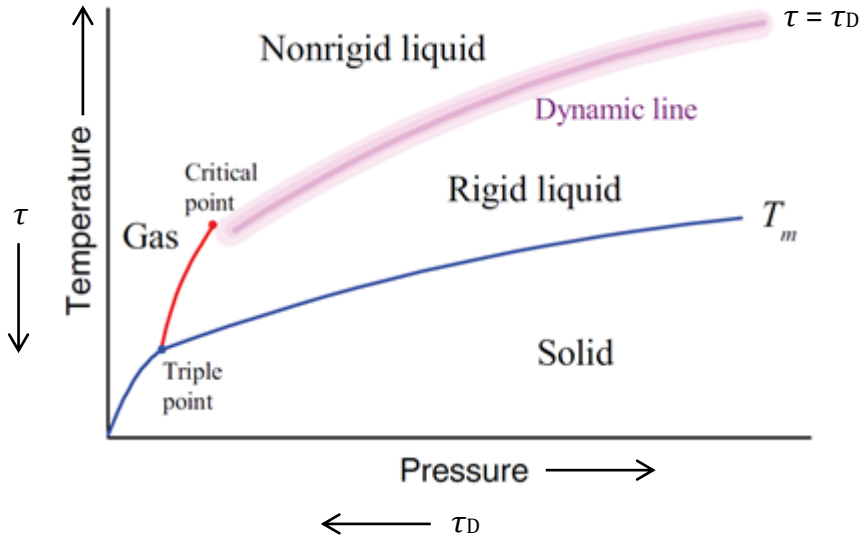

Figure 6.1: Frenkel line on the pressure-temperature phase diagram of an ordinary material (Brazhkin 2012).

In contrast with the understanding of the supercritical fluid state from van der Waals theory (§ 1.2), this new microscopic theory of a liquid predicts a distinguishable difference between liquid and gas (rather, rigid fluid and non-rigid fluid) which extends to arbitrarily high pressure and high temperature beyond the critical point (Brazhkin 2012).

The microscopic Frenkel model already has some support from empirical observations. Frenkel predicted that a rigid liquid should have a positive dispersion in sound velocities as there would be a contribution to the velocity from the shear

modulus for all frequencies which satisfy 6.1 (Brazhkin 2012). The positive dispersion of sound velocities in a liquid can be observed experimentally (Gorelli 2006, Simeoni 2010), and Frenkel theory predicts that it should cease to exist once the criterion defined in equation 6.2 is satisfied as there are then no more shear waves supported to contribute to the velocity.

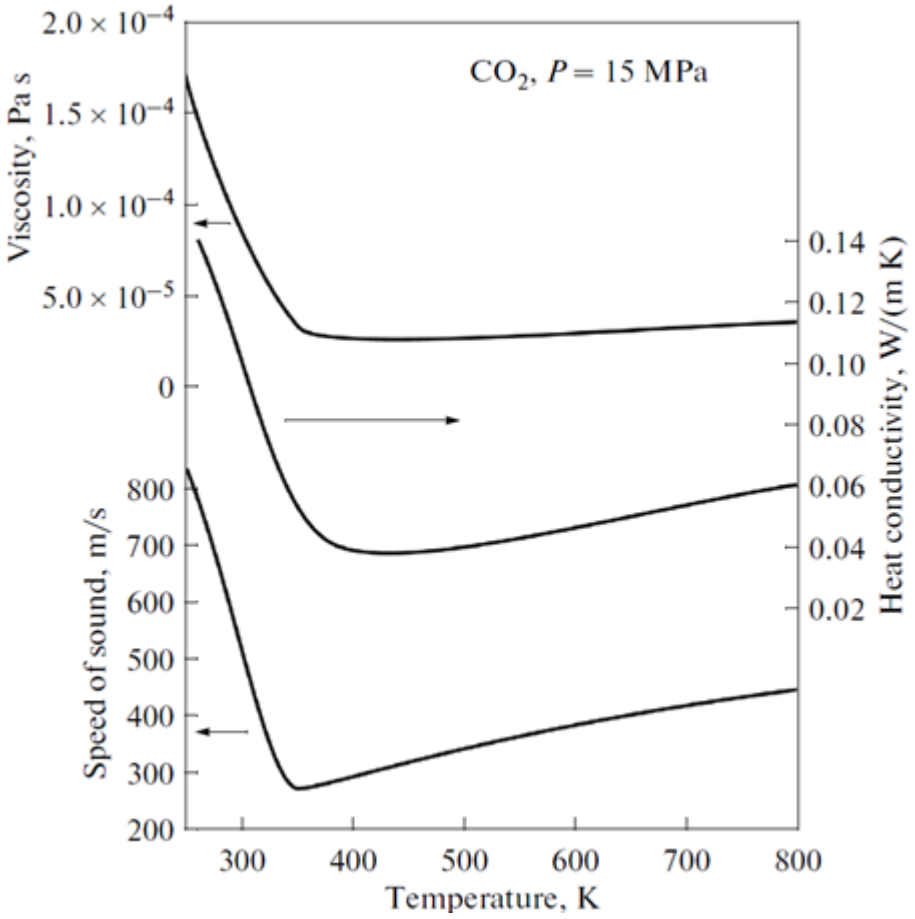

Figure 6.2: Temperature dependences of viscosity, thermal conductivity and sound velocity for carbon dioxide at twice its critical pressure exhibiting qualitative changes in their behaviours as the fluid goes from rigid to gas-like (Brazhkin 2014).

Taking the criterion 6.2 as the point at which particles in a liquid transition from solid-like diffusive to gas-like ballistic dynamics, the Frenkel model predicts qualitative changes in the behaviour of the diffusion coefficient, viscosity and thermal conductivity of a material with temperature (Brazhkin 2012, Brazhkin 2014, Trachenko 2014), which are consistent with experimental observations (Brazhkin 2012).

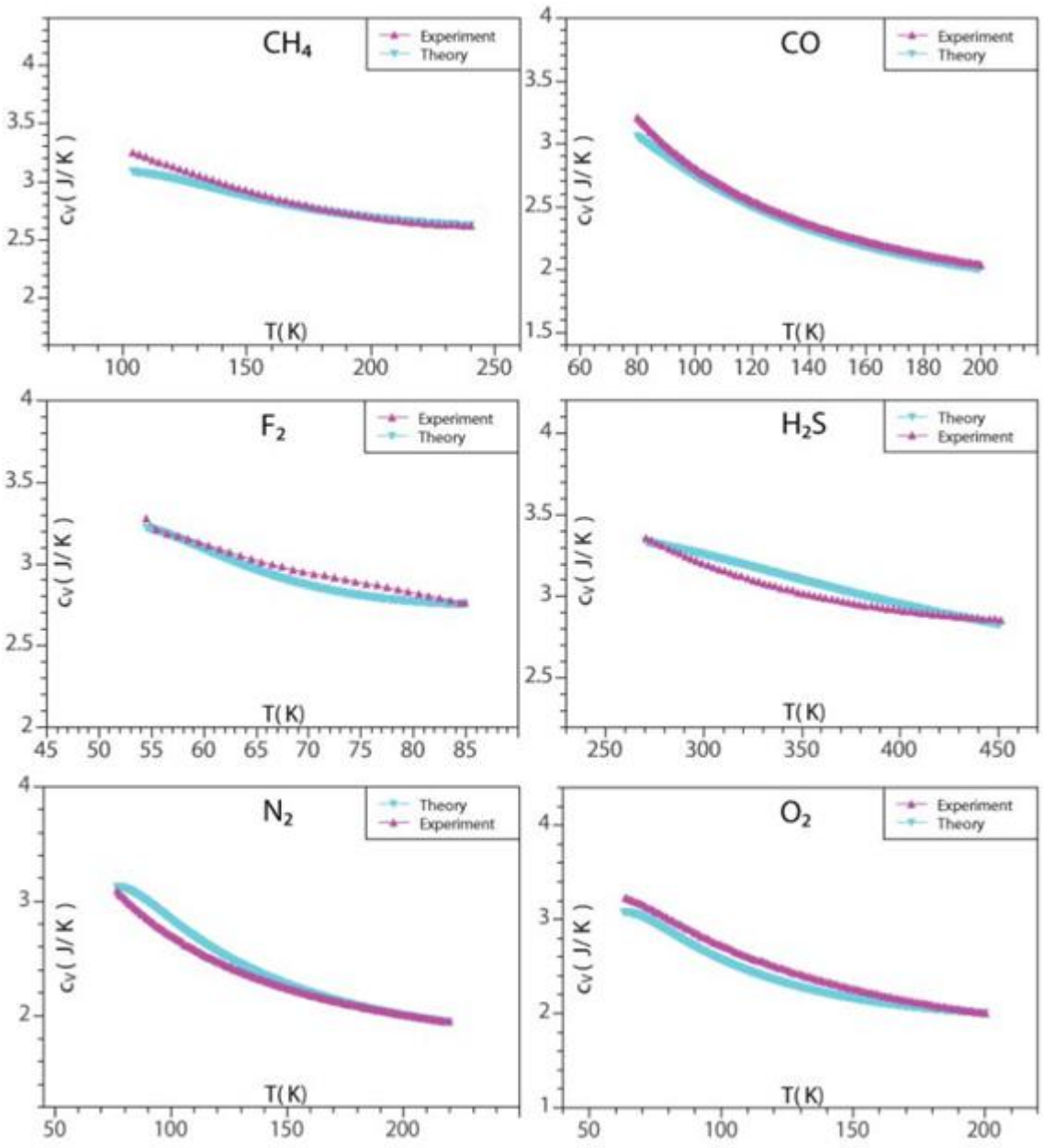

Figure 6.3: Examples of heat capacity c_v calculated by Bolmatov *et al.* using Frenkel theory for molecular liquids (blue lines), compared with measured c_v (purple lines) (Bolmatov 2012). Note: (The Boltzmann constant k_B = 1 in these simulations).

The Frenkel model also provides theoretical values of the constant volume heat capacity c_v which are consistent with measured values for a wide variety of liquids (Bolmatov 2012). The immediate drop in c_v from $3k_B$ to $2k_B$ (Figure 6.3) is attributed the gradual disappearance of shear rigidity as temperature increases and the range in equation 6.1 decreases, beyond which c_v tends towards its ideal gas value (Bolmatov 2013).

The properties of supercritical fluids are predicted to be at their most interesting close to the Frenkel line. For example, in Figure 6.2 the viscosity, thermal conductivity and sound velocity each takes their lowest values in carbon dioxide – a supercritical fluid widely used in various industries (§ 1.2) – and it is predicted that other technologically-useful properties of fluids, such as their surface tension and thus ability to wet and their chemical reactivity, might also be optimised close to the dynamic transition at the Frenkel line (Brazhkin 2014, Yang 2015). A confirmation of the presence of the Frenkel line would thus allow these useful physical and chemical parameters to be optimised for supercritical fluids at pressure and temperature arbitrarily higher than their critical values for a variety of industrial purposes.

6.1.1. The Widom line

In recent years, supercritical fluids have been subject to experiments which confirm a range of physical properties above, but close to, the critical point show uncharacteristic discontinuous properties. The discontinuities appear as maxima or *ridges* in properties such as the constant pressure heat capacity c_p (Xu 2005), thermal expansion coefficient and density fluctuations with temperature which protrude out separately from the critical point (Brazhkin 2011), and each protrusion is termed a *Widom line* in honour of American chemist Benjamin Widom. The Widom lines have also been noted as forming a boundary between liquid-like and gas-like dynamics beyond the critical point *via* the disappearance of the positive sound velocity dispersion (Gorelli 2006, Simeoni 2010).

It is important to draw the distinction between the Widom lines, which are each an extension of the maximum of an individual property of the fluid beyond the critical point, and the Frenkel line. The Frenkel line is predicted to extend to arbitrarily high pressure and temperature beyond the critical point, existing as a definitive transition between solid-like and gas-like fluid which is not related to the boiling curve, as evidenced by its prediction even in theoretical materials without a boiling curve (Brazhkin 2012).

6.1.2. Frenkel line report on argon

During preparation of this thesis, an article has been published claiming the first experimental detection of Frenkel line transition in argon (Bolmatov 2015). The proposed Frenkel line for argon is shown in Figure 6.4, alongside the points on the pressure-temperature path traversed during the experiments.

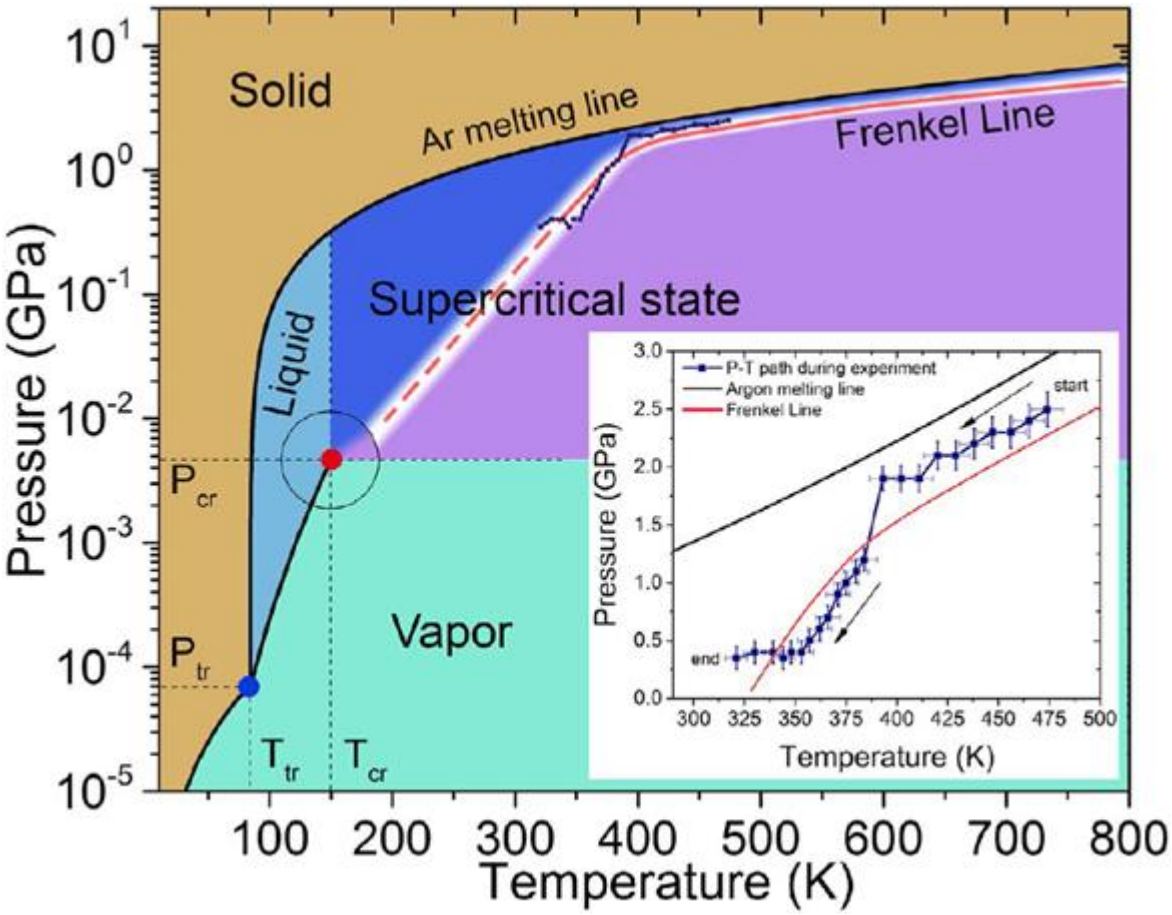

Figure 6.4: *P-T* phase diagram of argon with proposed Frenkel line by Bolmatov *et al.*, inset shows the path in pressure and temperature taken (Bolmatov 2015).

It is important to note that neither pressure nor temperature is kept constant during the experiments by Bolmatov *et al.*, their Frenkel line transition region (Figure 6.5b) comprises a large (1.5 GPa) change in pressure as well as a 60 K drop in temperature, but the Frenkel line transition is attributed solely to the raster in temperature. If the Frenkel line does exist as an equilibrium line on the pressure-temperature phase diagram, an accurate confirmation of its existence and location requires either pressure or temperature to be constant while the other varied.

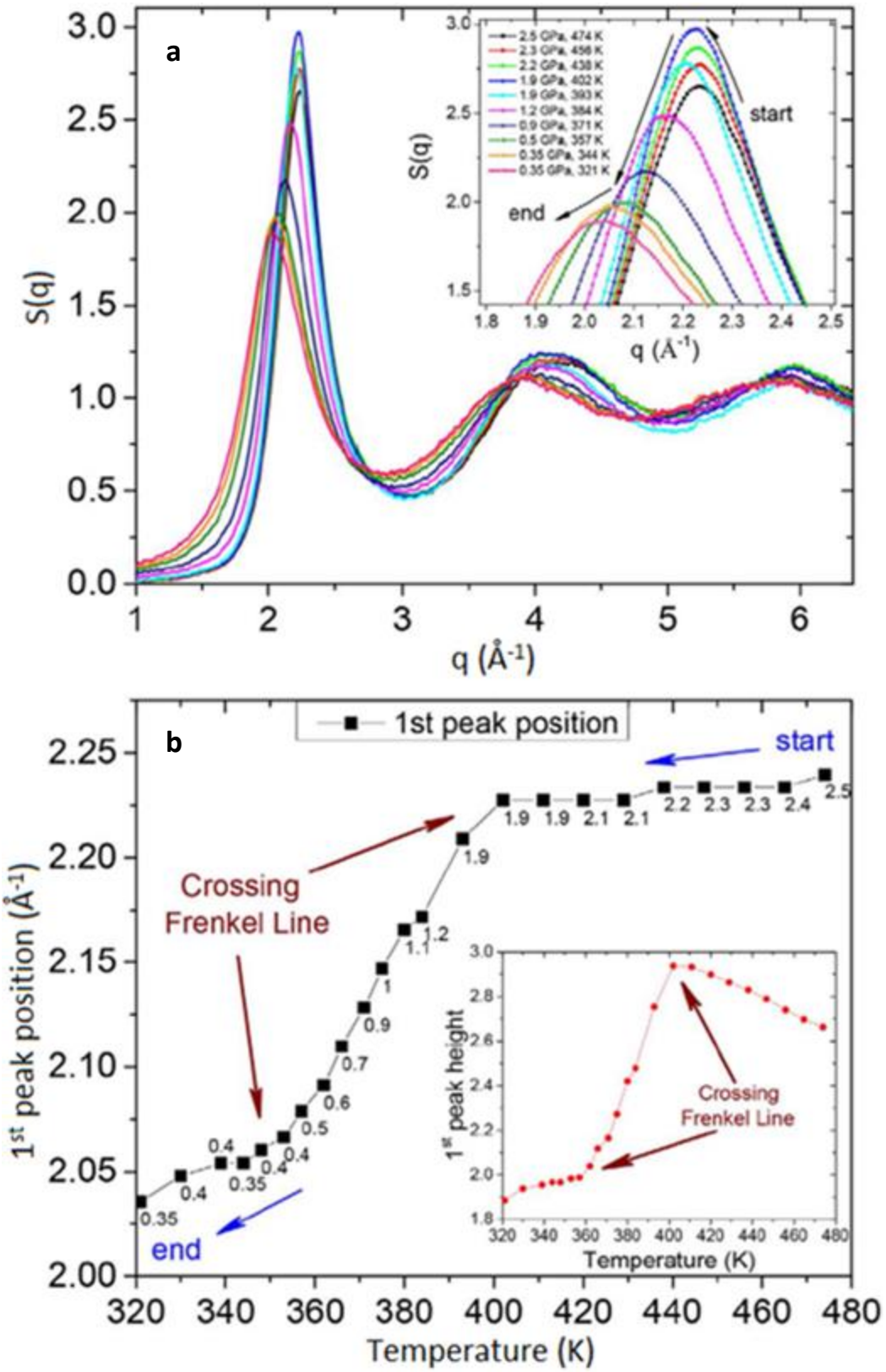

Figure 6.5: X-ray diffraction of fluid argon at high pressure and high temperature by Bolmatov *et al.* (**a**) Changes in structure factor $S(\boldsymbol{q})$ at different pressure-temperature conditions. (**b**) Position (and height, inset) of first peak in $S(\boldsymbol{q})$ at different pressure(labels)-temperature(axis) conditions (Bolmatov 2015).

Whether or not one expects to observe a significant change in the static structure of a fluid as it crosses the Frenkel line is not yet determined. The first major peak in the structure factor is effectively a statistical measure of short-range order, its position providing the average distance *a* between particles (Fischer 2006) and its size a measure of the amount of particles at that distance.

The suggestion that a significant change in the first peak should occur on crossing the Frenkel line suggests either that the particles should suddenly move relative to one another – an increase in *a*, *i.e.* a change in density – or their spread of separations around the average *a* should suddenly change. The former disagrees directly with established van der Waals equation of state (§ 1.2) – which the original Frenkel model does not challenge – and the latter implies that a gradual reduction in temperature should see a sudden jump in liquid relaxation time τ, which is not suggested in the original Frenkel model (Brazhkin 2012).

The work performed by Bolmatov *et al.* thus should not be considered as an experimental confirmation of the Frenkel line until it is repeated at constant pressure or temperature and supplemented with measured changes in parameters which are predicted to be affected by a transition across the Frenkel line.

6.2. Experimental considerations

High pressure and high temperature X-ray diffraction on methane was performed using the ID27 beamline, capable of delivering a high-intensity, focused monochromatic X-ray beam with micrometre-scale width to avoid contributions to diffraction patterns from the gasket or pressure sensors (Mezouar 2005).

ID27 also features a multichannel collimator for X-ray diffraction experiments. During DAC experiments, measurements are made on a samples orders of magnitude smaller than the diamonds used to apply pressure and there is a significant background spectrum caused by the inelastic Compton scattering of the diamonds.

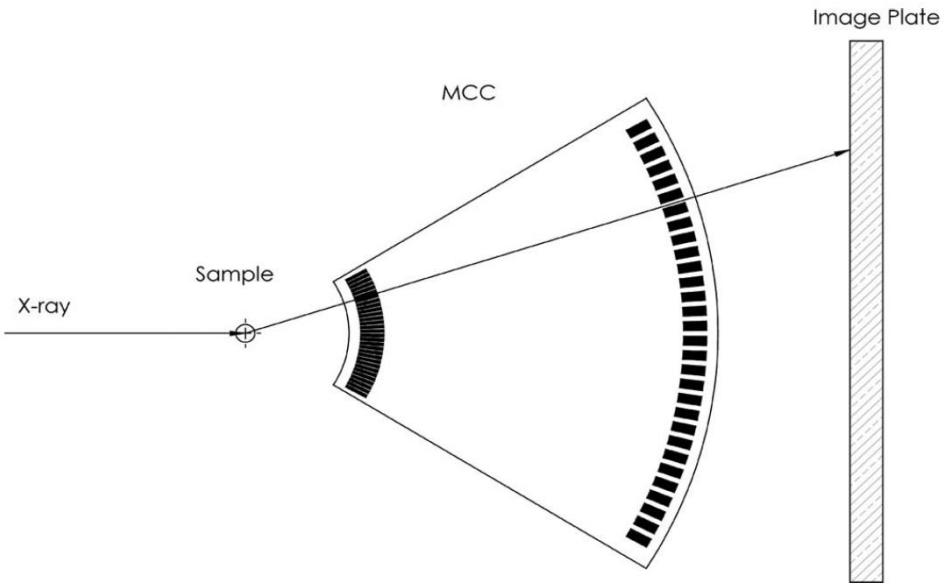

Figure 6.6: Design of the multichannel collimator at ID27 (Weck 2013).

To address this issue, the multichannel collimator was developed for use in high pressure experiments with large volume presses (Morard 2011) and recently redesigned for DACs (Weck 2013). The device is shown in Figure 6.6 and has the slits of the collimator trained to a focal point such that the device acts as a spatial filter which removes contributions from locations not in focus. The small (50 μm) primary slits define the effective volume over which the collimator samples, which is close to the sample sizes we expect in DAC experiments (Weck 2013), thus removing a large part of the Compton background.

6.2.1. Methane

As discussed in § 4.1.2, the low boiling point of methane allows for large amounts of liquid to be condensed inside the sample chamber of the DAC. The properties of methane are of fundamental interest as it is found in atmospheres throughout the solar system (Cruikshank 1976, Loveday 2001).

In addition, methane features an intense Raman peak around 3,000 cm^{-1} due to the C-H bonds stretching (Hollas 1996) which undergoes significant changes in its behaviour under high pressure phase changes (Hebert 1987). This makes methane, unlike monatomic argon, a suitable material for investigating how changes in the local

environment of a molecule due to a Frenkel transition might affect intramolecular vibrations.

6.3. Experiments on supercritical methane

6.3.1. Raman transition at 298 K

Methane was compressed to 1.5 GPa. During a slow decompression, Raman spectra showing the vibron mode of methane were collected at small pressure intervals according to the shift in ruby photoluminescence peaks. After background subtraction in OriginPro 9.0, the Raman vibron was fitted with a Lorentzian profile using MagicPlot fitting software.

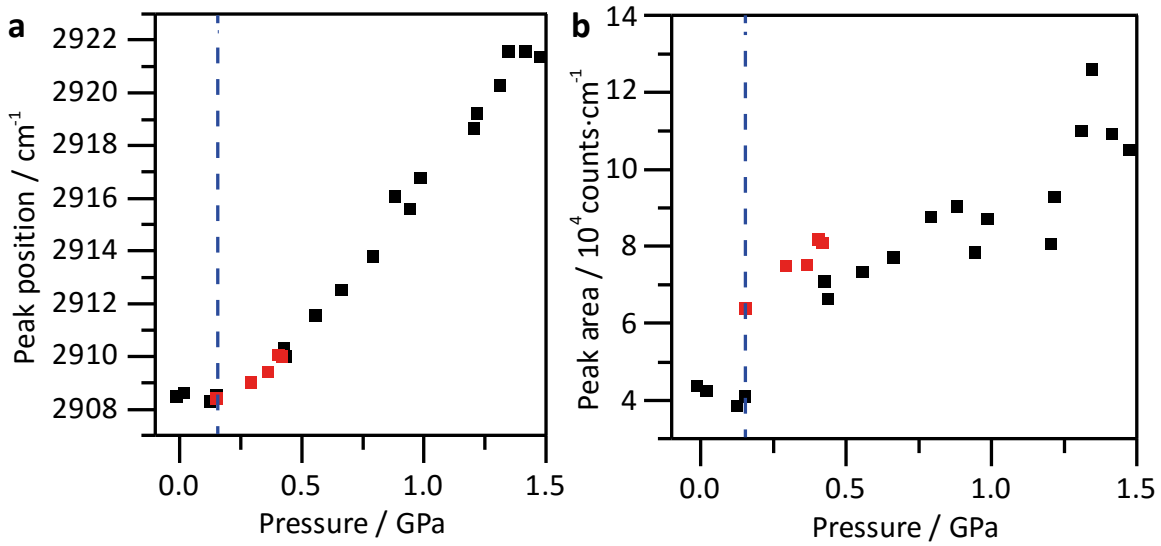

Figure 6.7: Raman vibron of methane 298 K. (**a**) Peak position and (**b**) fitted peak area at various pressures. Red squares are data collected after transition was observed on decompression. The blue dashed line is placed at 0.152 GPa to represent the suggested crossover.

Figure 6.7 shows the trends in the peak centre and area under the fitted peak with pressure. In both cases, a sudden change is observed between data collected at 0.153 and 0.151 GPa according to the fitted position of the ruby photoluminescence peak: the vibron peak frequency loses its dependence on pressure and the area

underneath the peak drops by a factor of 1/3 and loses its dependence on pressure. The blue line on Figure 6.7 is thus placed at the proposed transition pressure 0.152(±0.032) GPa – the error in transition pressure is propagated from equation 4.1 using the uncertainty in ruby peak positions, described in Appendix B.

The red squares in Figure 6.7 represent the 5 data points that were collected after the pressure had been released below the transition pressure at 0.152(±0.032) GPa, showing that the changes observed in vibron behaviour are reversible. The results signify a discontinuous transition in methane 100 K above its critical point.

6.3.2. X-ray diffraction at 298 K

To complement Raman spectroscopy measurements, X-ray diffraction has been performed on methane under isothermal decompression. Diffraction patterns were integrated using the Dioptas software package (Prescher 2015) and the pattern from the DAC once emptied of methane subtracted to remove any remnant Compton scattering. The integrated patterns were then normalised and the first peak fitted in MagicPlot (Appendix C has full details on X-ray analysis).

The trends in the position and magnitude of the first peak in $S(\boldsymbol{q})$ with pressure are shown in Figure 6.8 for two separate X-ray diffraction experiments. The parameters of the first peak show no discontinuities over the range of 0–1.5 GPa, where we see a transition in Raman behaviour. Notably, the maximum intensity of the first peak varies roughly linearly with pressure at constant temperature. This is unlike the inset of Figure 6.5b, which shows Bolmatov *et al.* claiming to have crossed the Frenkel line on reducing temperature due to a significant change in first peak height (Bolmatov 2015), but pressure is also changed in this region by approximately 1.5 GPa and the effects of pressure on $S(\boldsymbol{q})$ first peak height are wrongly neglected in the work by Bolmatov *et al.*

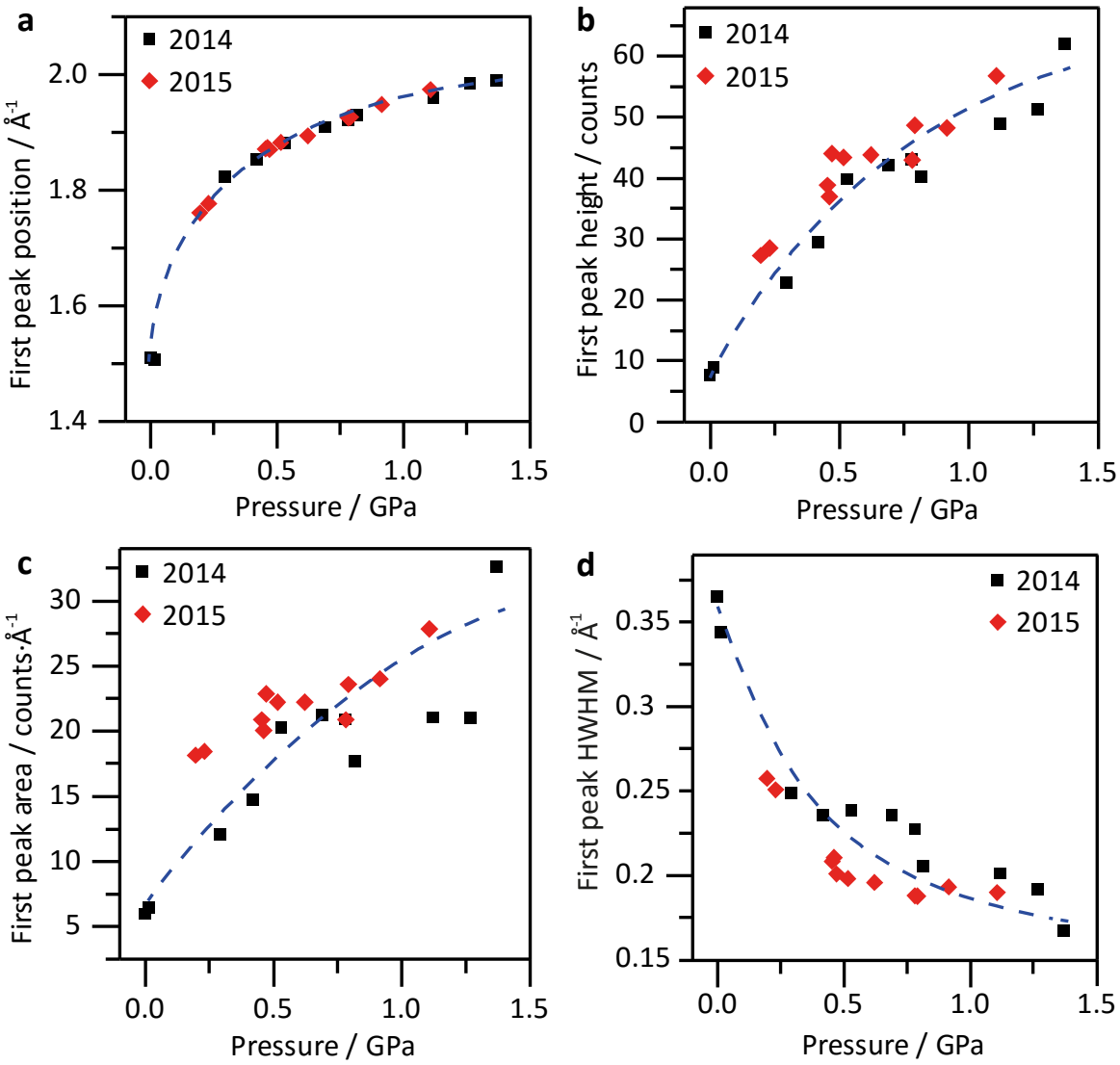

Figure 6.8: Changes in first peak of measured structure factor $S(\boldsymbol{q})$ of methane under decompression from 1.5 GPa at 298 K. (**a**) The centre position, (**b**) the normalised height, (**c**) the normalised area and (**d**) the HWHM. Blue dashed lines are intended as guides to the eye only.

Figure 6.8 shows the position, height, area and width of the first peak in $S(\boldsymbol{q})$ varying smoothly upon decompression from 1.5 GPa to ambient pressures at room temperature.

Figure 6.8a gives the position of the first major peak in $S(\boldsymbol{q})$, *i.e.* $2\pi/a$ where a is the average distance between particles (Fischer 2006). By considering each methane molecule as existing inside a sphere with radius $a/2$, we can convert first peak position into the volume V occupied by a single methane molecule.

The smooth variation in Figure 6.8a, and thus Figure 6.9, resembles the isotherms of an ideal gas. The foundation of the van der Waals corrections to the ideal gas law is to account for the effects of intermolecular potential energy on the pressure and volume of a system (Baierlein 1999). At temperatures far exceeding T_C, kinetic energy of the particles far exceeds their potential energy and the V plot varies monatonically in P as in the ideal gas law (Figure 1.2). We thus fit volume data with the equation:

$$P = \frac{A}{V + B} + C \qquad 6.3$$

Where A, B and C are scaling and translating coefficients. Figure 6.9 shows the fit from OriginPro 9.0, with A = 4.20 kg Å^2 s^{-2}, B = -13.82 and C = -0.20 GPa.

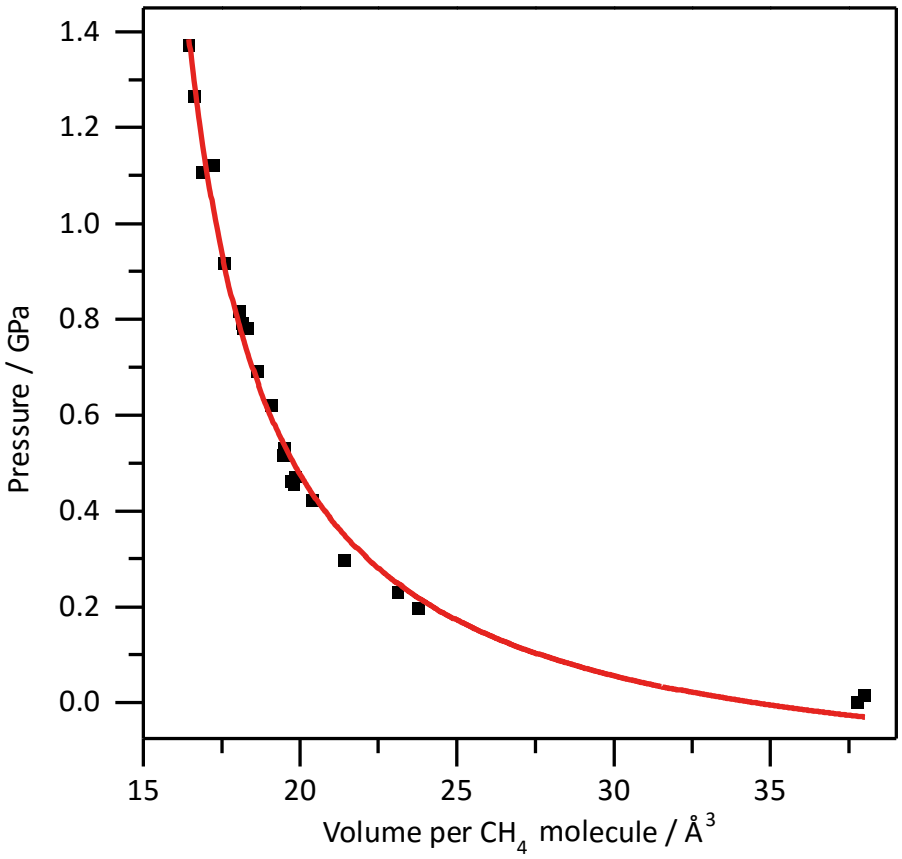

Figure 6.9: Modified isothermal ideal gas equation of state fitted to volumes derived from first peak in $S(\boldsymbol{q})$ for supercritical methane at 298 K as measured by X-ray diffraction.

The trend in volume with increasing pressure correlates with existing theory of supercritical fluids according to the van der Waals equation. Above T_c, we do not expect to observe discontinuous changes in volume (*i.e.* density) under isothermal compression. This is in disagreement with the significant change in first peak position seen by Bolmatov *et al*. (Figure 6.5, Bolmatov 2015), which we can attribute to their uncontrolled path in P-T.

6.3.3. Experiments at 523 K

The implications of the Frenkel model are that a characteristic crossover between rigid and non-rigid fluid exists until arbitrarily high pressure and temperature beyond the critical point. If the Raman transition in Figure 6.7 is due to a Frenkel line transition, we thus expect to observe it at higher temperatures. Methane was heated to 523 K and decompressed, with pressure measured using Sm:YAG crystals for the insensitivity of their photoluminescence peaks to temperature. Methane vibron data were processed as in § 6.3.1.

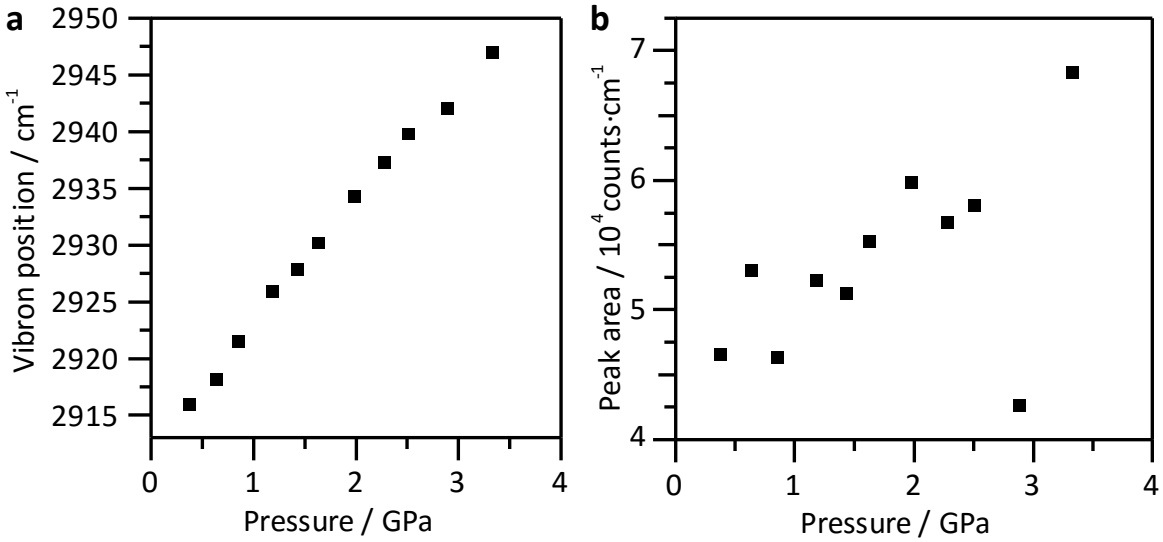

Figure 6.10: Raman vibron of methane 523 K. (**a**) Peak position and (**b**) fitted peak area at various pressures.

In contrast to Figure 6.7, Figure 6.10 show the vibron peak position and area varying smoothly between 0.3 and 3.0 GPa, no change in behaviour of the vibron intensity is observed and the vibron position does not become unresponsive to pressure.

The anomalously small methane vibron at 2.9 GPa can be attributed to data collected near the edge of the sample chamber of the DAC, while all other data was collected in the centre – *i.e.* maximising the amount of methane inside the beam.

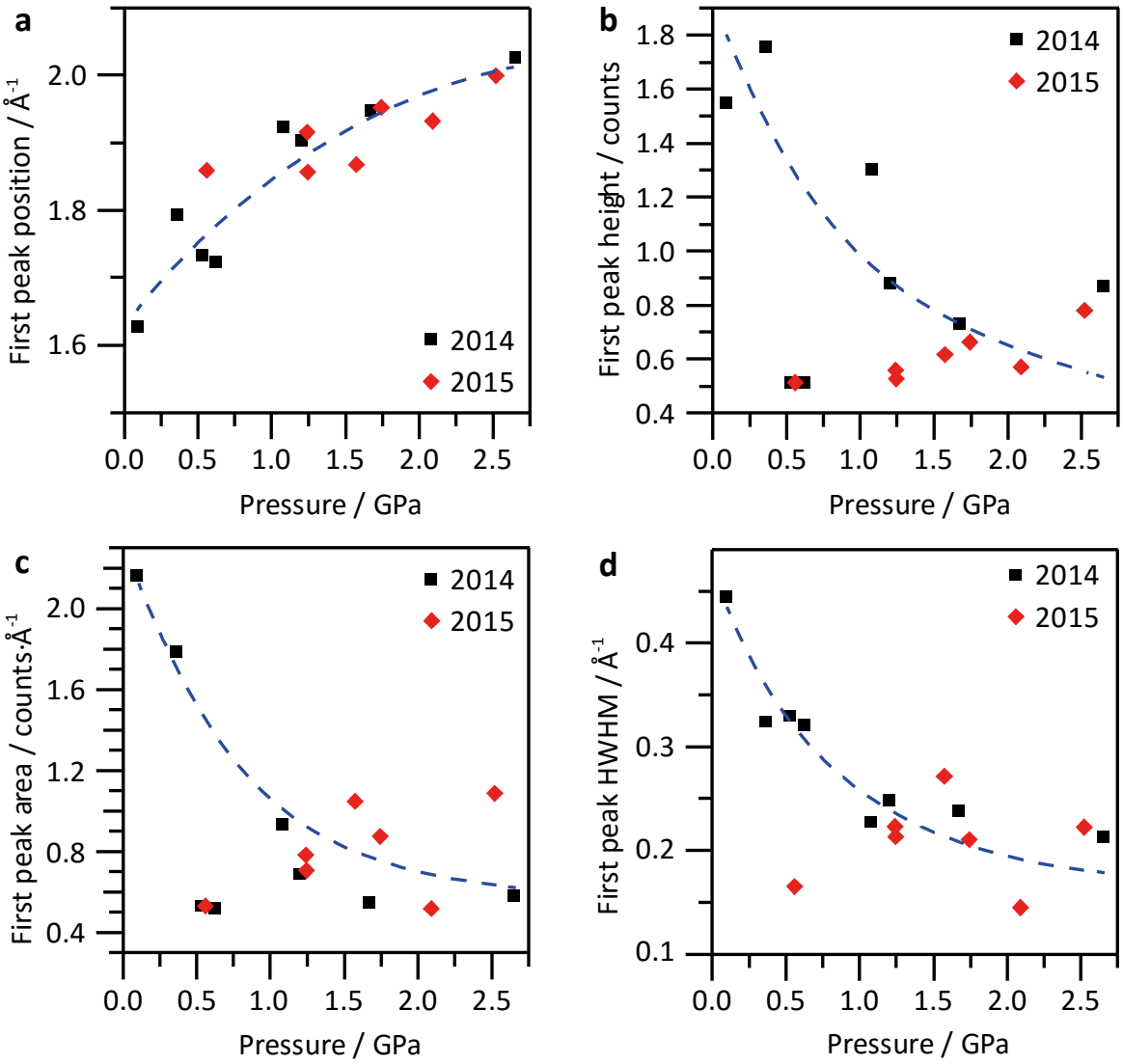

Figure 6.11: Changes in first peak of measured structure factor $S(\boldsymbol{q})$ of methane under decompression from 2.5 GPa at 540 K. (**a**) The centre position, (**b**) the normalised height, (**c**) the normalised area and (**d**) the HWHM. Neglecting the cluster of points around 0.5 GPa, the blue dashed lines are intended as guides to the eye.

Similar to experiments at 298 K, and in accordance with existing van der Waals thermodynamics, X-ray diffraction experiments on methane at 540 K show no clear discontinuities in static structure factor $S(\boldsymbol{q})$ that would suggest a change in structure (Figure 6.11).

As in § 6.3.2, first peak positions in $S(\boldsymbol{q})$ are converted into volume per atom and fitted with the modified ideal gas law in equation 6.3. The resulting smooth PV isotherm is shown in Figure 6.12 with the parameters A = 14.96 kg Å^2 s^{-2}, B = -11.23 and C = -0.64.

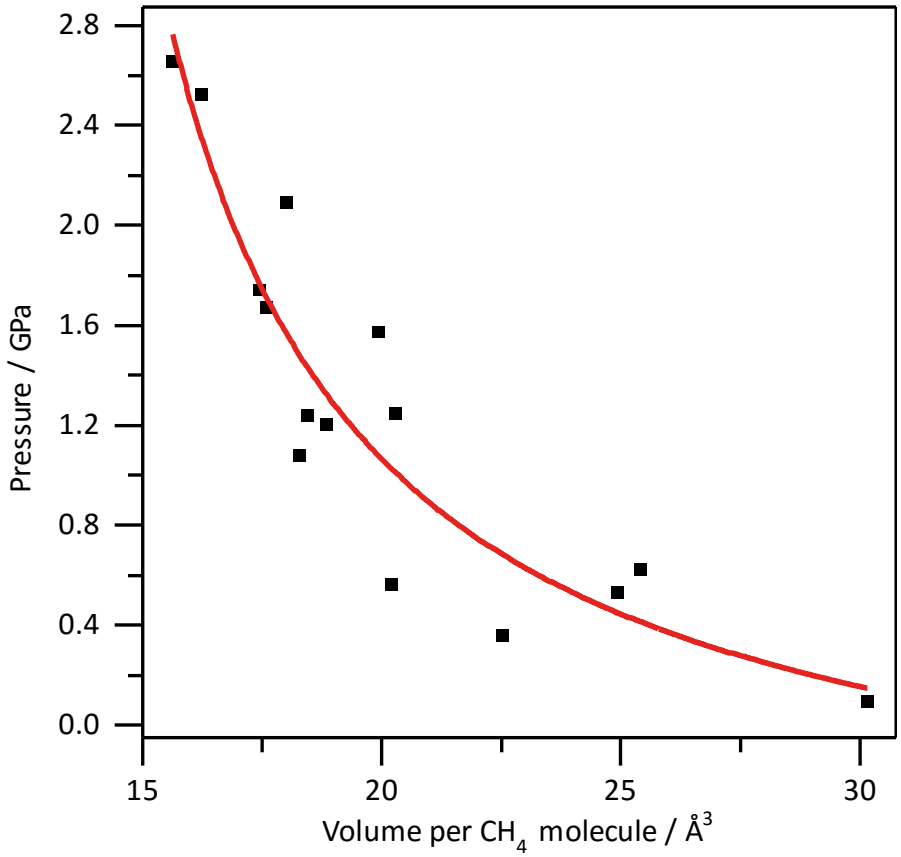

Figure 6.12: Modified isothermal ideal gas equation of state fitted to volumes derived from first peak in $S(\boldsymbol{q})$ for supercritical methane at 540 K as measured by X-ray diffraction.

The broad distribution of first peak position in Figure 6.11a, and thus volume in Figure 6.12, compared with similar experiments at 298 K can be attributed to variations in temperature over the course of the two experiments – two separate experimental runs with average temperature at collection 540 ± 11.5 K. Referring to discussions in § 4.2, the uncertainty in measuring pressure at elevated temperature is already high at low DAC pressures, the large variations in diffraction patterns at 523 K (Figure 6.11) can be attributed to both the temperature variation and its corresponding large effect on accurate pressure measurements.

Chapter 7. Conclusions and future directions

7.1. Hydrogenation of graphene in a diamond anvil cell

The experiments in this work in this thesis can be summarised as a pressure-temperature "phase diagram" for the reaction between graphene and hydrogen. Figure 7.1 shows reacting conditions for hydrogen in blue and deuterium in green, with conditions at which no reaction occurs shown as red crosses. The red cross at ambient pressure and high temperature is placed in the knowledge that temperature in absence of pressure will readily remove hydrogen from hydrogenated graphene (§ 2.3).

Other than the reactions at 6.5 GPa, there is a clear trend in L_D – the average separation between defects, and thus hydrogenation extent (§ 3.3) – with increasing pressure. This could be down to experimental procedures, as the 6.5 GPa reactions were performed before the acquisition of Sm:YAG crystals for accurate measurement of pressure at high temperature in the low-pressure regions, where diamond splitting is not the most useful for fast pressure determination mid-experiment since the splitting is small and the overlap between unstressed and stressed diamond peaks is significant (Figure 4.8). After Sm:YAG was included in experiments, a higher level of confidence in pressure measurements was found in quick measurements, such that fewer alterations needed to be made to be sure to have constant pressure. Repeating the experiments at 6.5 GPa might see higher levels of hydrogenation – perhaps even Stage II, but the high levels of hydrogenation reached with single-sided samples at more modest pressures suggest that having the samples prepared as membranes to

allow hydrogen access to both sides of the graphene will have a much larger impact on the hydrogenation extent than further pressure increase.

Omitting the 6.5 GPa reactions from a plot of L_D against pressure P, the extent of hydrogenation in the region explored can be tentatively fitted with a decay function in Origin, giving $L_D = 350.3 \times P^{-2.67}$ (inset of Figure 7.1), which suggests a defect spacing of 1 nm – well into Stage II – could require pressures of 9 GPa at 473 K – although it is very important to note that only three data points are fitted.

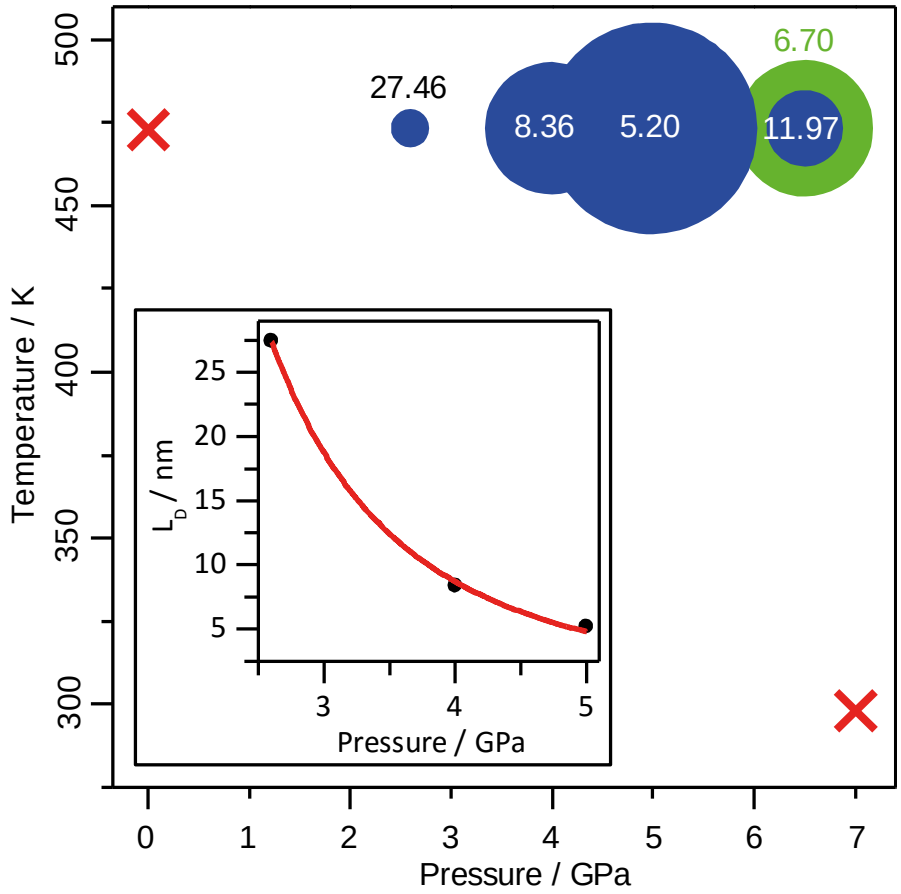

Figure 7.1: Pressure-temperature phase diagram for graphene-hydrogen reactions, where bubbles represent the extent of hydrogenation according to I_D/I_G and L_D values marked onto the points, data from Figure 5.3, Figure 5.9, Figure 5.12 and Figure 5.13. Crosses show non-reacting conditions. (green) Deuterated graphene, data from Figure 5.6. (inset) Decreasing L_D with pressure P.

The results in Chapter 5 confirm a new method of creating partially-hydrogenated graphene using a combination of high pressure and high temperature in a diamond anvil cell. The table in Figure 7.2 shows values of L_D collected from Raman

spectra in the literature employing plasma methods on single-sided samples (Luo 2009, Burgess 2011, Matis 2012) and with an atomising gun (Guillemette 2014), demonstrating the competitiveness of the DAC method with existing methods. In all cases with existing methods, the L_D values shown are those where those authors have seen saturation in I_D/I_G, whereas the new DAC method has improvements that may be made in order to improve hydrogenation – in pressure, temperature, time and sample preparation. As such, the first lab synthesis of graphane is feasible using high pressure and high temperature.

	L_D / nm
(Elias 2009)	20.09 (single-sided)6.61 (double sided)
(Luo 2009)	4.04
(Burgess 2011)	4.53
(Matis 2012)	4.31
(Guillemette 2014)	4.5 (Stage I) / 1.5 (Stage II)
This work	5.20

Figure 7.2: Table of L_D representing hydrogenation extent from the literature.

As a general comment on the large variation in hydrogenation extents in samples throughout the work, we refer to the discussion in § 2.1 of ripples in graphene, *i.e.* variations in the factor η which describes the curvature (or sp^3-like nature) of the bonding. Graphene naturally exhibits ripples and curves, and it is suggested that these sites with higher η should hydrogenate more readily than the flatter sites. Based on STM images from their study of deliberately disordered graphene, Lucchese *et al.* characterise defect sites in graphene as comprising two parts: the defect itself and an extended "activated region" surrounding the defect where the graphene sheet exhibits short range, out-of-plane rippling (Lucchese 2010). These ripples signify a drastic change in the η value close to the defects and we would expect a similar activated region to occur around hydrogenated sites, which could cause a cascade effect in hydrogenation around distinct points – for instance, as in Figure 5.8, where we simultaneously observe low-I_D/I_G locations and our most highly hydrogenated locations.

In samples with the highest hydrogen content (Figure 5.8 and Figure 5.9), I_D/I_G is measured as 3.7. Using equation 3.7, this equates to an average distance L_D of 5.20 nm between hydrogenated sites on the graphene lattice. Referring to the study on deliberately disordered graphene by Lucchese *et al.* and Figure 3.7, an I_D/I_G of around 3.5 and L_D around 5 nm sees the transition between Stage I and Stage II derivatisation (§ 3.3), indicating that samples hydrogenated under conditions of 5.0 GPa and 473 K are close to Stage II.

The high I_D/I_G also comments on the stability of graphene hydrogenated with only a single side exposed. The stability of single-sided hydrogenated graphene was modelled by DFT calculations on graphene with added ribbons of hydrogenated graphene of various thicknesses and densities by Xiang *et al.*, who saw that above 10 at. % coverage, single-sided hydrogenated graphene was not stable (Xiang 2010). These calculations form the basis of the assertion by Burgess *et al.* that an I_D/I_G of 2 equates to approximately 10 at. % coverage, as both Burgess *et al.* and Elias *et al.* saw saturation in their I_D/I_G at around 2 (Elias 2009, Burgess 2011). Although there are issues with accuracy in the measurements of hydrogen content as well as the Xiang *et al.* DFT model lacking intrinsic ripples which we expect to affect reactivity, it is not inconceivable that samples prepared through the DAC method are hydrogenated on both sides, albeit not to the same extent as a sample prepared as a membrane. Under compression in a DAC and heating, hydrogen molecules may find themselves accessing the underside of the graphene lattice by entering through the gaps around the edges of the graphene crystal or by diffusing through the copper itself (Braaten 1936) – indeed, fluid molecular hydrogen is even known to diffuse through diamond anvils under compression (Howie 2013).

The employment of STM will become crucial in experiments where samples prepared through the DAC method exhibit higher levels of functionalisation, beyond the Stage II transition where the Raman peaks broaden. The suggestion prevailing in the literature (Luo 2009, Burgess 2011) is that plasma methods begin to etch graphene above a certain power to cause damage, thus limiting the method from producing fully-hydrogenated graphane. Burgess *et al.* remark on a broadening of the Raman peaks as in Stage II, but suggest that this is wholly down to etched defects, incorrectly suggesting a discrepancy between the low-level hydrogenation and low-level defects

up to that point (Burgess 2011), while Luo *et al.* suggest a loss of reversibility of their hydrogenated graphene as evidence that defects are present (Luo 2009). The Luo explanation has a stronger foundation, and could be confirmed easily with atomic-scale images of Stage II hydrogenated (and subsequently dehydrogenated) graphene prepared by the DAC method – where the risk of etching is not present since the reaction occurs between graphene and molecular H_2, not due to bombardment of the graphene with high-energy atomic H.

The preparation of graphene samples suspended over apertures in a substrate as a quasi-freestanding membrane will be crucial in the refinement of the DAC hydrogenation method developed in this thesis. Suspended samples elsewhere have seen a roughly doubled rate of hydrogenation with the plasma hydrogenation technique (Elias 2009). In addition, the Grüneisen parameters of graphene have only been determined so far for graphene on a substrate, where the substrate has significant influence on the compressibility of the sample (Proctor 2009, Filintoglou 2013), and preparation of graphene membranes for DAC experiments would allow the mechanical properties of freestanding pristine graphene to be probed without dependence on a substrate material.

7.1.1. Towards graphane with DAC-compatible graphene membranes

In order to vastly improve hydrogen coverage and to press towards making fully-hydrogenated graphane using the DAC method, it will be important to develop samples of free-standing graphene *membranes*. Samples of this architecture were employed by Elias *et al.*, who saw a roughly doubled rate of hydrogenation for their plasma method when graphene was exposed to hydrogen on both sides (Elias 2009).

Graphene grown by CVD onto copper is commonly transferred between substrate using a polymer conduit. A thin layer of the polymer can be deposited onto the graphene and the copper chemically etched away. The graphene-on-polymer can then be placed onto the desired substrate and the polymer chemically removed (Mattevi 2011).

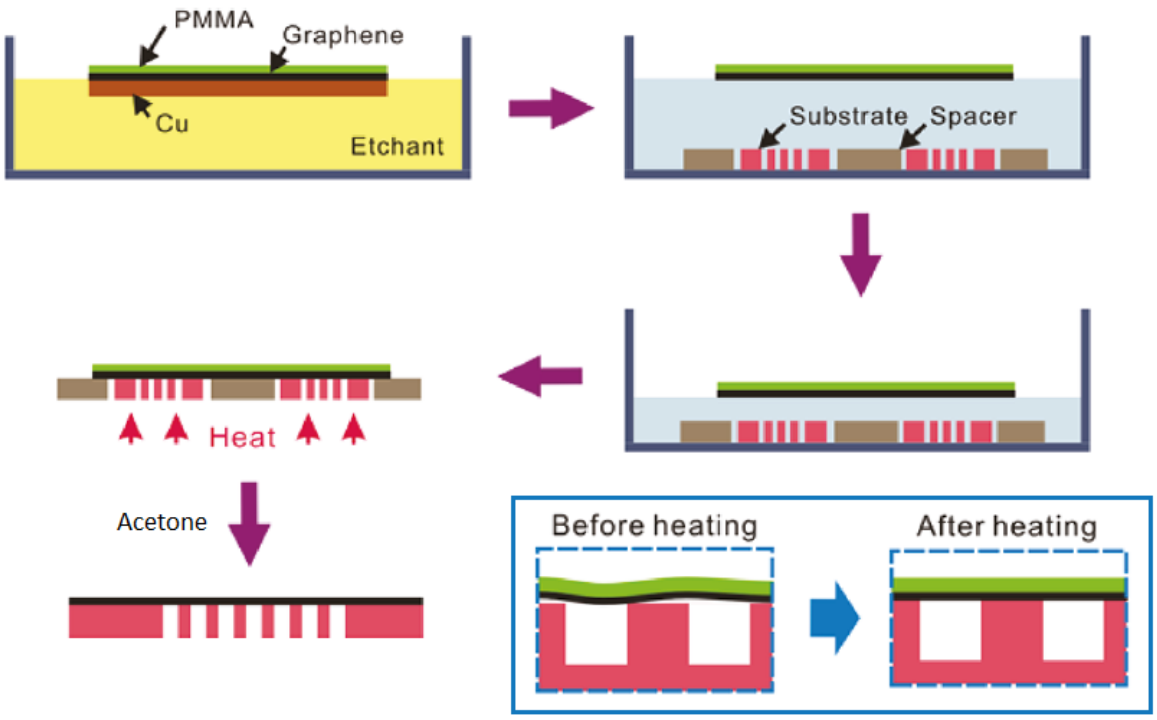

Figure 7.3: Transfer of CVD-grown graphene from copper substrates to substrates containing apertures, such that monolayers exist as partially-unsupported membranes, *via* a polymer conduit. Modified from (Suk 2011).

By utilising laser drilling, spark erosion or milling with a focused ion beam, substrates can be prepared either as bulk containing a system of apertures or as a large batch of small – 50-200 μm – substrates with apertures. Following the scheme proposed in Figure 7.3 (Suk 2011) could allow batch processing of graphene grown by CVD onto copper into DAC-compatible graphene membranes for future hydrogenation experiments.

7.2. Search for the Frenkel line

Through gradual pressure reduction in methane at 298 K, we observe discontinuous changes in the intensity and in the pressure dependence of the frequency of its Raman-active vibron – well above its critical point.

The loss of rigidity at the Frenkel line is due to a complete disappearance of the vibrational, "solid-like" component of the motion of liquid particles. In other words,

the particles are no longer partially confined to equilibrium positions by intermolecular interactions (Brazhkin 2012). This insensitivity to intermolecular interactions can be used to explain the Raman effects observed below 0.152(±0.032) GPa (Figure 6.7), where the frequency of the Raman vibron of methane and its intensity are no longer affected by density, *i.e.* changes in intermolecular separations that would alter interaction potentials. The significant step in vibron intensity at 0.152(±0.032) GPa, which we observed to be reversible, could be a result of the sudden appearance and disappearance of solid-like behaviours which affect the environment of each molecule, affecting their polarizability and thus, by equation 3.6, the intensity of the Raman scattering (Hollas 1996).

That the Raman transition observed in methane at 298 K is not reflected at far greater temperatures (Figure 6.10) casts doubt over whether the transition is in fact due to a transition across the Frenkel line. However, whilst the effects described by Widom phenomena are only present close to the critical point, the Raman transition was observed at a temperature exceeding T_C of methane by over 100 K, eliminating the possibility of confusion with a Widom line. It could be possible that the Frenkel line – or, at least, some of its detectable effects such as the Raman behaviour transition – do not extend to arbitrarily high pressures and temperatures beyond the critical point as predicted, and this could be confirmed by observing the Raman discontinuity at smaller intervals in temperature, both away from and towards the critical point.

Importantly, the transition in Raman behaviours seen in Figure 6.7 is not accompanied by any detectable change in local structure (Figure 6.8 and Figure 6.11). From van der Waals theory (§ 1.2), we do not expect any discontinuous change in density at any pressure-temperature conditions once we are beyond the critical point. The Frenkel line, if this is indeed the cause behind the Raman transition, is thus not associated with a first-order phase transition.

An important step in confirming that the Raman transition seen in 6.3.1 is an effect due to Frenkel line transition will be to investigate the effect in other Raman-active systems. For its astronomical importance (Owen 2005), Raman activity (Schmidt 1991) low critical temperature (Linstrom 2011) and ease of loading into a DAC, nitrogen is an immediate candidate, as well as hydrogen (Howie 2015) or ammonia (Wright 1984, Palasyuk 2014). Both nitrogen and hydrogen have strong

rotational modes unlike the near-spherical methane, allowing further investigations into the changes in Raman behaviour at the transition.

7.2.1. Acoustic measurements at high pressure

As discussed in § 6.1, a crossing of the Frenkel line is marked by a complete collapse of the frequency range (equation 6.1) over which shear waves can be supported by a liquid. Thus, a concrete method of confirming the validity of the Frenkel line theory would be observations of such an acoustic change in a material well above its critical point. Acoustic measurements on sample in a DAC are complicated by the diamond anvils, which are typically orders of magnitude larger than the sample itself, but some methods have been developed.

A technique has been developed by Chigarev *et al.* which allows direct measurement of the speed of sound in a material placed inside a DAC (Chigarev 2008) using a pulsed laser to generate acoustic waves inside the sample and a continuous wave laser to detect fluctuations in reflectivity of the sample due to acoustic waves. The Chigarev method could detect Frenkel transitions by the disappearance of the transverse mode signals from a sample as it becomes a non-rigid fluid under decompression. However, it has not yet been demonstrated in transparent samples and the effectiveness of generating and detecting acoustic waves at the diamond-sample interface could be lost.

Using a buffer rod tailored to convert compressive waves into shear waves and direct them through a diamond anvil, Jacobsen *et al.* have devised a method for measuring sound velocities in crystalline samples under compression in a DAC (Jacobsen 2004). However, their method does not see shear reflections in alcohol samples until the liquid-glass transition line has been crossed, suggesting that some redesigning must be made in order to detect a Frenkel transition (Jacobsen 2005).

To probe for Frenkel line transitions in the lower pressure range, it is possible to employ a large volume press such as the Paris-Edinburgh cell (Besson 1992) in place of the diamond anvil cell. The Paris-Edinburgh cell has recently been modified to feature a buffer rod arrangement for ultrasonic measurements (Kono 2013), and by varying the pressure of the sample and sweeping the frequency of the transducer, it

could be possible to watch the range in equation 6.1 decrease until eventual disappearance at the Frenkel line.

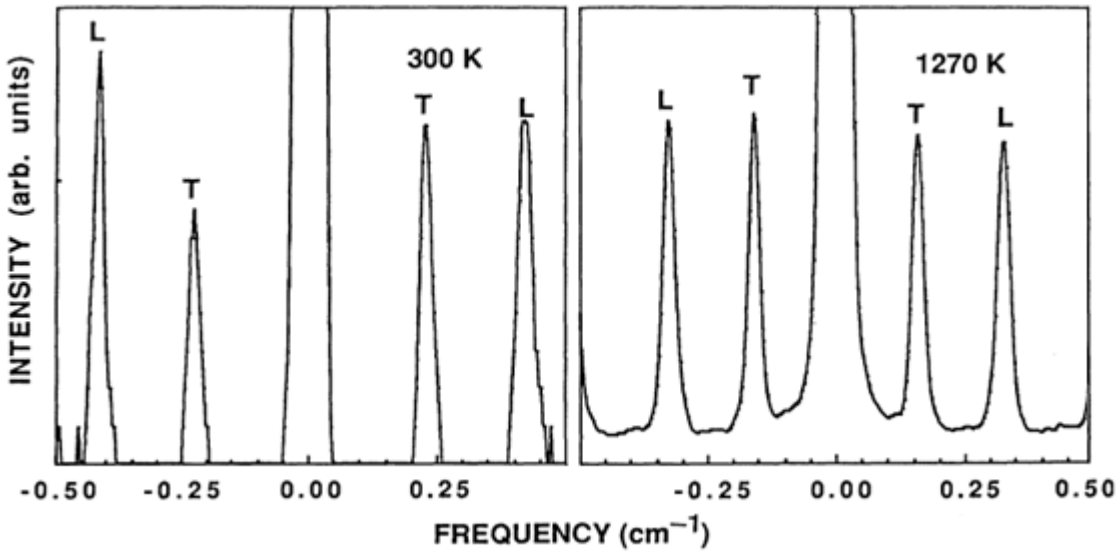

Figure 7.4: Brillouin spectra of boron trioxide at ambient and elevated temperatures, exhibiting shear (T) waves well into the liquid state (Grimsditch 1989).

Perhaps the most suitable method for observing acoustic phenomena inside a DAC is Brillouin spectroscopy, the analogue of Raman spectroscopy where light is inelastically scattered by long wavelength acoustic phonons in a material (Polian 2003). Low-frequency modes attributed to shear rigidity are present in liquids (Figure 7.4, Grimsditch 1989) and a crossing of the Frenkel line would see these modes disappear.

Appendix A: Other interactions between graphene and pressure media

A study by Filintoglou *et al.* details experiments performed on graphene under quasi-hydrostatic pressure in a 1:1 mixture of FC70 and FC77 *Fluorinert* – branded coolant fluids, generally fluorocarbons and fluorinated oils, often used as a pressure transmitting medium in neutron scattering experiments to avoid noise from scattering from hydrogen in other common PTMs such as alcohols and oils (Sidorov 2005). Filintoglou *et al.* observed defect-related Raman peaks appearing on pressure release (Filintoglou 2013). The elegant explanation offered by Filintoglou *et al.* is that at pressures above the melting line of the PTM, the graphene will exist essentially as a free-floating single-layer in a solid solvent, having no preferential adhesion to either the substrate or the PTM. However, upon melting, the monolayer graphene will develop some preferential adhesion to either the substrate or the PTM, varying in different locations across the sheet. This, they claim, causes structural damage to the graphene as the PTM melts.

In order to ensure that the D peak was activated in high pressure and temperature hydrogenation experiments due to hydrogen bonded to the graphene lattice and not due to structural damage across the sample caused by crossing the hydrogen melting line several times during an experiment (on initial compression, on both heating and cooling, and once again at pressure release), graphene was loaded into a HT cell in an atmosphere of liquid nitrogen. Pressure was raised to 7.1 GPa, well into the region where nitrogen is solid at ambient temperature (Schmidt 1991) and then released. Care was taken not to mount the sample in the gasket on this occasion, as it was important to be able to distinguish between damage caused by PTM melting and damage potentially caused by contact with the gasket. Raman inspection of the sample afterwards reveals no damage to the sample – evident by the lack of D peak across both sides of the copper flake (Figure A.1).

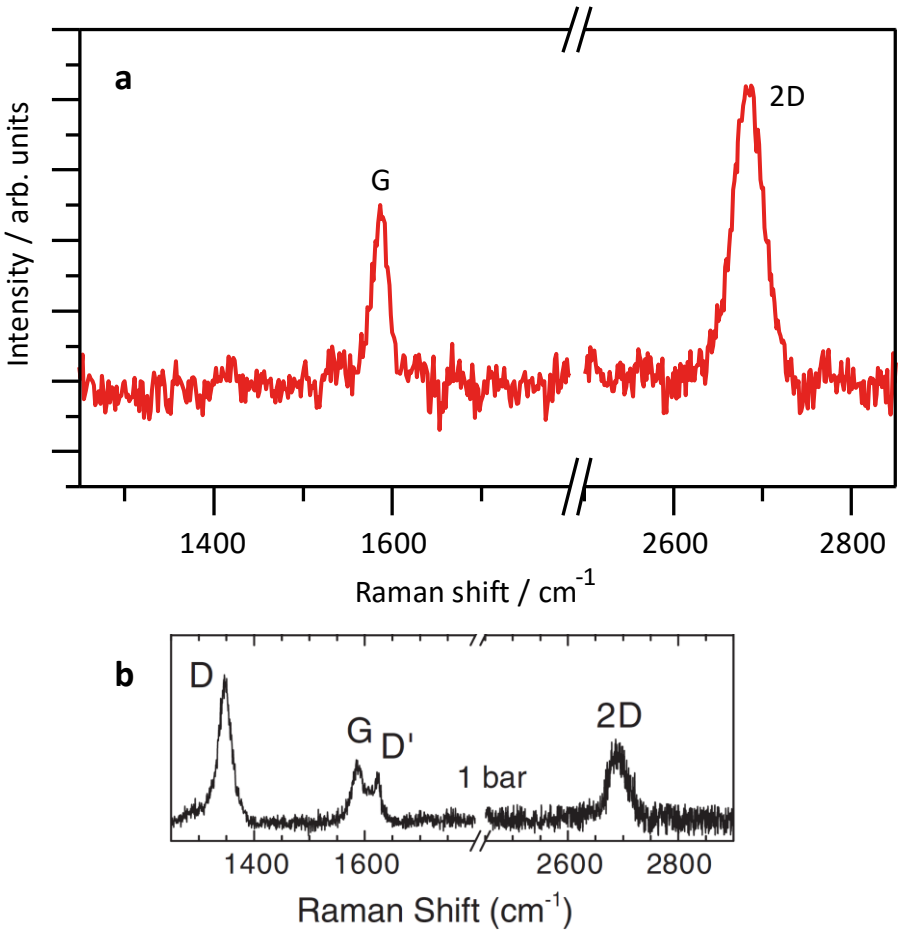

Figure A.1: (a) Raman spectrum of graphene after compression in nitrogen to 7.1 GPa, resembling pristine graphene with no structural damage. (b) Graphene spectrum after compression to 3.0 GPa in a *Fluorinert* mixture, exhibiting disorder-induced D and D' peaks (Filintoglou 2013).

The explanation offered by Filintoglou *et al.* suggests a phenomenon which should be true for any solidifying and melting atmosphere around graphene on a solid substrate, which is not the case in experiments with nitrogen either here or in past compressions by Proctor *et al.* (Proctor 2009), or in hydrogen and deuterium. While the large electronegativity difference between the carbon and fluorine means that the C-F bonds in the *Fluorinert* compounds are strong and the D peak is unlikely to be caused by a chemical reaction between PTM and graphene (Lemal 2004), it also makes the *Fluorinert* compounds partially polarised. The relationship between polarity of a PTM and its tendency to damage graphene has been probed by compressing graphene on copper in a 4:1 methanol-ethanol mixture as a PTM, Figure A2 shows the Raman spectrum of graphene after pressure was released.

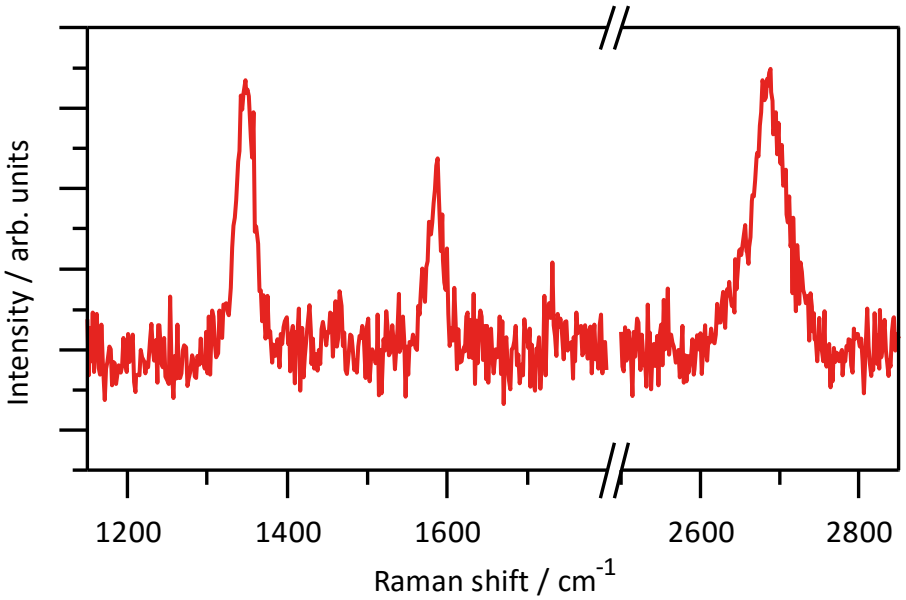

Figure A.2: Raman spectrum of graphene on copper substrate after compression to 7.2 GPa in a 4:1 methanol-ethnol mixture, resembling Stage I disordered graphene with I_D/I_G = 1.7 determined by Gaussian peak fitting in MagicPlot.

The implication from Figure A.2 and Filintoglou *et al.* is that graphene will become disordered upon compression cycles in an atmosphere that is polar, which is supported in part by experiments elsewhere compressing graphene to 7 GPa in alcohol mixtures (Nicolle 2011), though no comment was made there on the presence or disappearance of the D peak after pressure treatment. Results on compression in hydrogen and deuterium shown in Figure 5.14 and in nitrogen in Figure A.1a, however, suggest that compression cycles on graphene in a non-polar medium will not lead to damage even when the melting line is crossed.

Appendix B: Propagation of errors in pressure measurement

When describing the location of the Raman transition in § 6.3.1, it is important to consider the error in measuring pressure using ruby photoluminescence. First, by rearranging equation 4.1 from Mao *et al.* (Mao 1986):

$$P = \frac{A}{B}^{B} + \frac{\Delta \mathrm{R1}}{\mathrm{R1}_0}^{B} + \frac{A}{B} \qquad \text{B.1}$$

The constants A and B are derived from fitting equation 4.1 to experimental data by Mao *et al.* and their errors can be considered not to affect our measurements. Thus only the second term in equation B.1 needs to be considered. We have then:

$$\frac{\delta P}{P} = B\frac{\delta \Delta \mathrm{R1}}{\Delta \mathrm{R1}} + B\frac{\delta \mathrm{R1}_0}{\mathrm{R1}_0} \qquad \text{B.2}$$

The uncertainties in the shift in R1 and in the original position in R1 can be taken from the standard deviations of the R1 peak positions given in the report outputted from MagicPlot. In general, the values are around 0.0015 cm^{-1}, so $\delta\Delta$R1 and $\delta \mathrm{R1}_0$ will be replaced by a single value, δfit, and B.2 becomes:

$$\delta P = PB\left(\frac{\delta \mathrm{fit}}{\Delta \mathrm{R1}} + \frac{\delta \mathrm{fit}}{\mathrm{R1}_0}\right) \qquad \text{B.3}$$

Substituting values of B from (Mao 1986) and δfit from MagicPlot:

$$\delta P = 7.665\left(\frac{0.0015}{\Delta \mathrm{R1}} + \frac{0.0015}{\mathrm{R1}_0}\right)P \qquad \text{B.4}$$

Averaged over the 24 datapoints collected during the experiment in § 6.3.1, the value of δP is 0.032 GPa.

Appendix C: Analyses of raw data from supercritical methane experiments

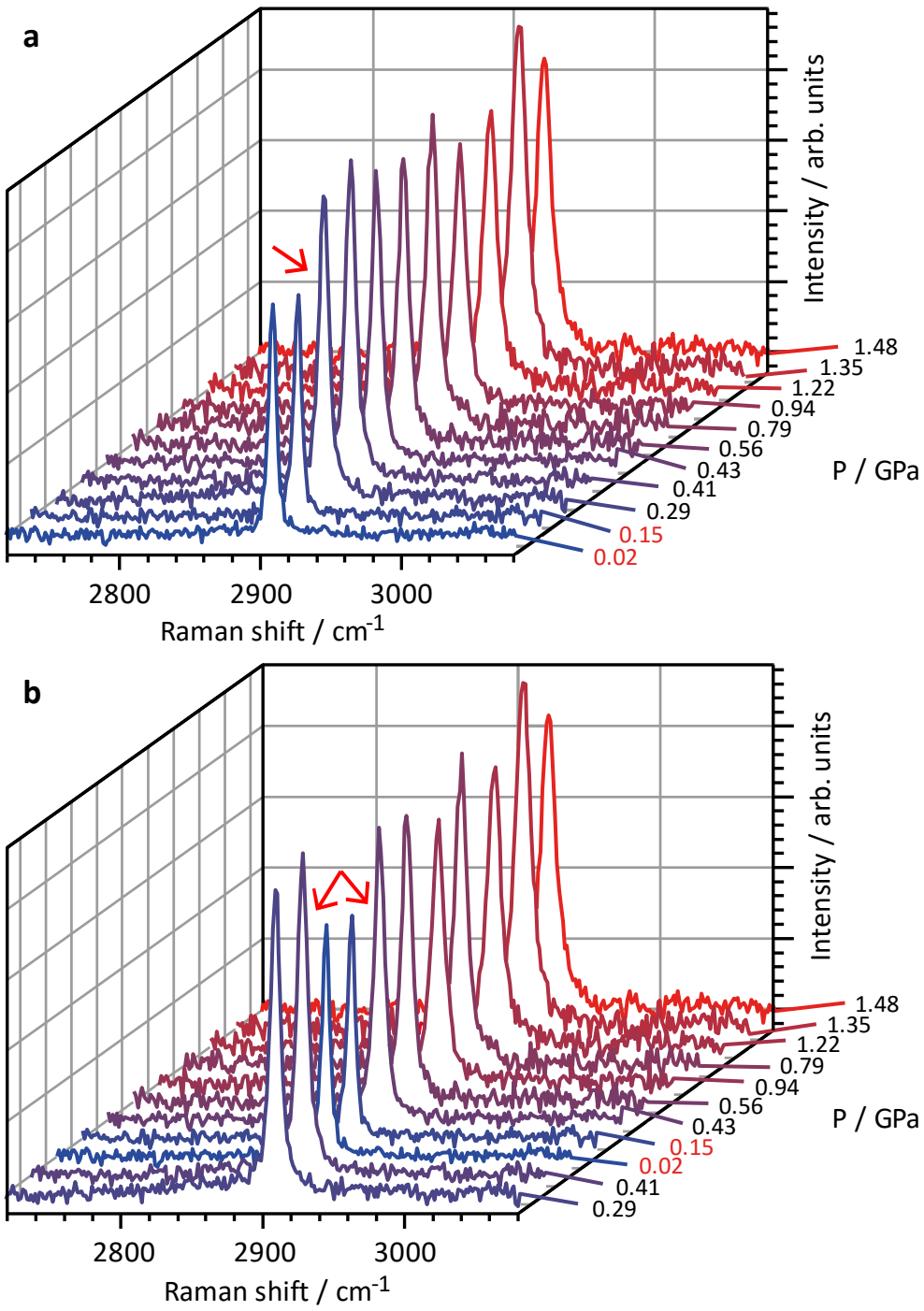

Figure C.1: Waterfall plots showing selected Raman spectra from § 6.3.1. Spectra are displayed in (**a**) pressure-order and (**b**) acquired order to demonstrate reversibility of the Raman transition. Red arrows point to transition pressures.

Figures C.1 and Figure C.2 show the vibrational mode of methane upon pressure variation at 298 and 523 K respectively. Raman spectra in Chapter 6 were collected *in situ* in a DAC using spectrometer layout in Figure 3.11. Background was fitted with a parabola in MagicPlot Student and subtracted, then the peak fitted with a Lorentzian curve. Details of the vibron obtained from the fitting form the plots in Figure 6.7 and Figure 6.10.

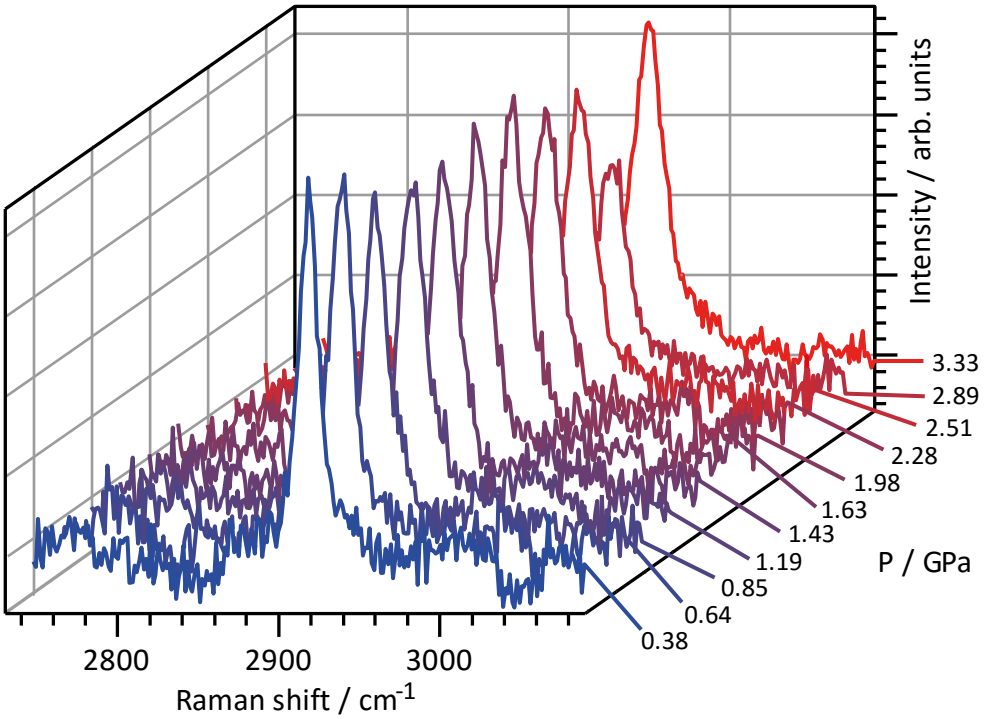

Figure C.2: Waterfall plot of Raman spectra from experiment in §6.3.3 (Figure 6.10) not exhibiting any sudden changes in intensity as in Figure C.1.

The procedure by which data on the first peak in $S(\boldsymbol{q})$ for supercritical methane was analysed begins with integration using the Dioptas software (Prescher 2015). Experiment geometry was calibrated in Dioptas using a lanthanum hexaboride or cerium dioxide standard.

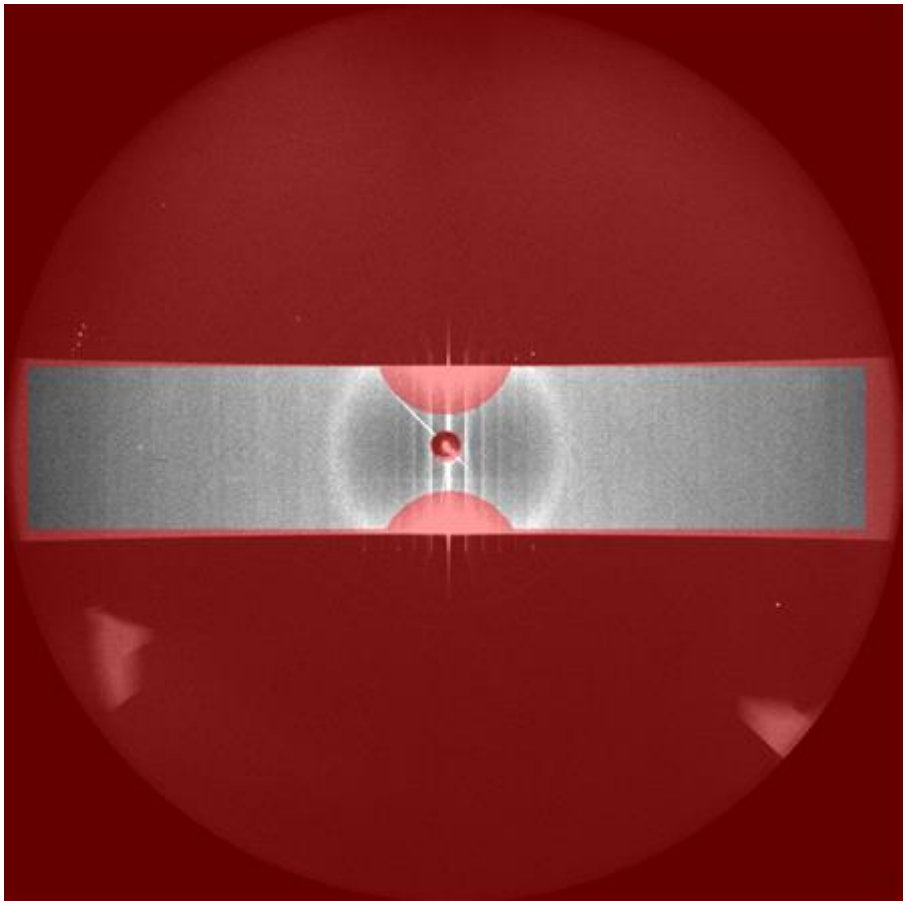

Figure C.3: Two-dimensional diffraction pattern of fluid methane at 0.69 GPa captured at ID27, semi-transparent red areas are those which are masked out (inset: image without multichannel collimator).

Figure C.1 shows how the images must be masked in order to remove sections of the image plate which are not exposed due to the multichannel collimator. To account for Compton scattering background not removed by the collimator, scattering data was collected from the DAC after methane had been released (Figure C.2a).

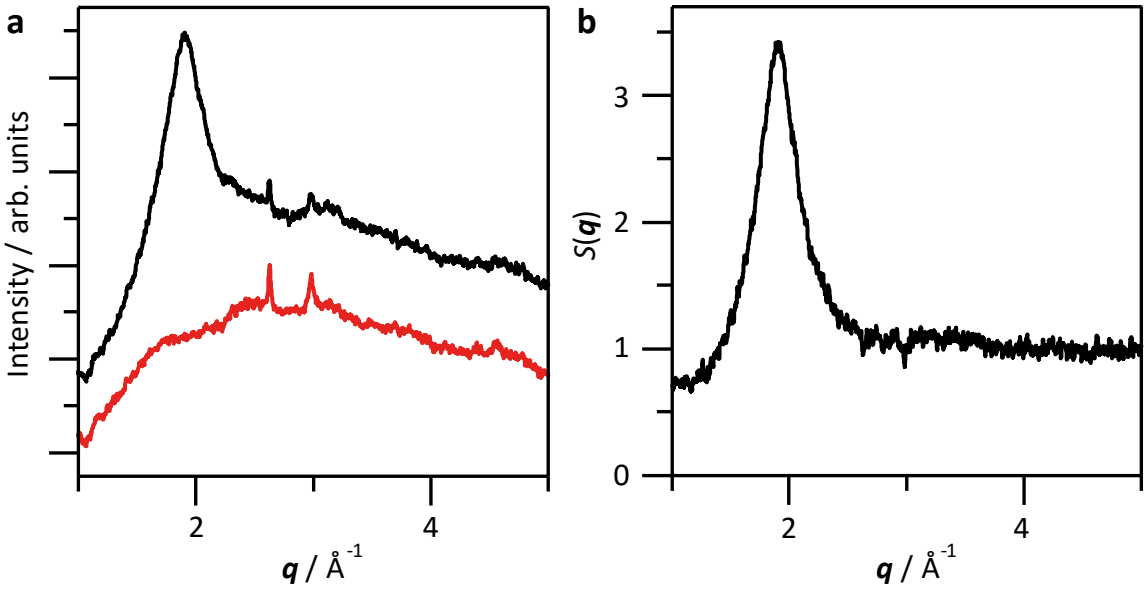

Figure C.4: Background correction of integrated diffraction patterns. (**a**) Diffraction pattern of fluid methane at 0.69 GPa (black) and Compton-scattered signal from empty pressure cell (red). (**b**) Static structure factor of methane $S(\boldsymbol{q})$ at 0.69 GPa obtained by subtracting cell background and normalising in the high $\boldsymbol{q}$ limit.

After subtraction of the background, all data was normalised in the high $\boldsymbol{q}$ limit where $S(\boldsymbol{q})$ tends to 1 (Fischer 2006). The first peak in $S(\boldsymbol{q})$ can be fitted with a Gaussian peak using the MagicPlot software and used to generate the data shown in Figure 6.8 and Figure 6.11.

References

(Akahama 2006) Y Akahama & H Kawamura, "Pressure calibration of diamond anvil Raman gauge to 310 GPa", *J. Appl. Phys.* **100**, 043516 (2006)

(Ansell 2015) D Ansell *et al.*, "Hybrid graphene plasmonic waveguide modulators", *Nat. Commun.* **6**, 8846 (2015)

(Badding 1991) J V Badding, R J Hemley & H-K Mao, "High-Pressure Chemistry of Hydrogen in Metals: *In Situ* Study of Iron Hydride", *Science* **253**, 421 (1991)

(Bagri 2010) A Bagri *et al.* "Structural evolution during the reduction of chemically derived graphene oxide", *Nat. Chem.* **2**, 581 (2012)

(Bai 2010) J Bai *et al.*, "Graphene nanomesh", *Nat. Nanotechnol.* **5**, 190 (2010)

(Baierlein 1999) R Baierlein, "Thermal Physics", Cambridge University Press: Cambridge, United Kingdom (1999)

(Bakowies 1992) D Bakowies & W Thiel, "Theoretical study of buckminsterfullerene derivatives $C_{60}X_n$ (X=H, F; n=2, 36, 60)", *Chem. Phys. Lett.* **193**, 236 (1992)

(Balog 2009) R Balog *et al.*, "Atomic Hydrogen Adsorbate Structures on Graphene", *J. Am. Chem. Soc.* **131**, 8744 (2009)

(Balog 2010) R Balog *et al.*, "Bandgap opening in graphene induced by patterned hydrogen adsorption", *Nat. Mater.* **9**, 315 (2010)

(Balog 2013) R Balog *et al.*, "Controlling Hydrogenation of Graphene on Ir(111)", *ACS Nano* **7**, 3823 (2013)

(Bangert 2010) U Bangert *et al.*, "Structure of hydrogen-dosed graphene deduced from low electron energy loss characteristics and density functional calculations", *Appl. Phys. Lett.* **97**, 253118 (2010)

(Beckman 2003) E J Beckman, "Supercritical and near-critical CO_2 in green chemical synthesis and processing", *J. Supercrit. Fluid.* **28**, 121 (2004)

(Bell 1984) P M Bell, H-K Mao & K Goettel, "Ultrahigh Pressure: Beyond 2 Megabars and the Ruby Fluorescence Scale", *Science* **226**, 542 (1984)

(Benedetti 1999) L R Benedetti *et al.* "Dissociation of CH_4 at High Pressures and Temperatures: Diamond Formation in Giant Planet Interiors?", *Science* **286**, 100 (1999)

(Berger 2004) C Berger *et al.*, "Ultrathin Epitaxial Graphite: 2D Electron Gas Properties and a Route toward Graphene-based Nanoelectronics", *J. Phys. Chem. B* **108**, 19912 (2004)

(Bernal 1924) J D Bernal, "The Structure of Graphite", *Proc. R. Soc. Lond. A* **106**, 749 (1924)

(Besedin 1998) S P Besedin & A P Jephcoat, "High-Pressure X-ray Studies of the Ni-H, Re-H and Al-H Systems", *Rev. High Pressure Sci. Technol.* **7**, 301 (1998)

(Besson 1992) J M Besson *et al.*, "Neutron powder diffraction above 10 GPa", *Physica B* **180-181**, 907 (1992)

(Birch 1944) A J Birch, "Reduction by dissolving metals", *J. Chem. Soc.*, 430 (1944)

(Block 1976) S Block & G Piermarini, "The diamond cell stimulates high-pressure research", *Physics Today* **29**(9), 44 (1976)

(Boehm 1986) H P Boehm, R Setton & E Stumpp, "Nomenclature and terminology of graphite intercalation compounds", *Carbon* **2**, 241 (1986)

(Bolmatov 2012) D Bolmatov, V V Brazhkin & K Trachenko, "The phonon theory of liquid thermodynamics", *Sci. Rep.* **2**, 421 (2012)

(Bolmatov 2013) D Bolmatov, V V Brazhkin & K Trachenko, "Thermodynamic behaviour of supercritical matter", *Nat. Commun.* **4**, 2331 (2013)

(Bolmatov 2015) D Bolmatov *et al.*, "The Frenkel Line: a direct experimental evidence for the new thermodynamic boundary", *Sci. Rep.* **5**, 15850 (2015)

(Bovenkerk 1959) H P Bovenkerk *et al.*, "Preparation of Diamond", *Nature* **184**, 1094 (1959)

(Braaten 1936) E O Braaten & G F Clark, "The Diffusion of Hydrogen though Copper", *Proc. R. Soc. Lond. A.* **135**, 504 (1936)

(Brazhkin 2011) V V Brazhkin *et al.*, "Widom Line for the Liquid-Gas Transition in Lennard-Jones System", *J. Phys. Chem. B* **115**, 14112 (2011)

(Brazhkin 2012) V V Brazhkin *et al.*, "Two liquid states of matter: A dynamic line on a phase diagram", *Phys. Rev. E* **85**, 031203 (2012)

(Brazhkin 2014) V V Brazhkin *et al.*, "The Frenkel Line and Supercritical Technologies", *Russ. J. Phys. Chem. B* **8**, 1087 (2014)

(Bridgman 1948) P W Bridgman, "Rough Compressions of 177 Substances to 40,000 kg/cm^{-2}", *Proc. Natl. Acad. Sci. U.S.A.* **76**, 71 (1948)

(Burgess 2011) J S Burgess *et al.*, "Tuning the electronic properties of graphene by hydrogenation in a plasma enhanced chemical vapor deposition reactor", *Carbon* **49**, 4420 (2011)

(Caillabet 2011) L Caillabet, S Mazevet & P Loubeyre, "Multiphase equation of state of hydrogen from *ab initio* calculations in the range 0.2 to 5 g/cc up to 10 eV", *Phys. Rev. B* **83**, 094101 (2011)

(Cançado 2006) L G Cançado *et al.*, "General equation for determination of the crystallite size L_a of nanographite by Raman spectroscopy", *Appl. Phys. Lett.* **88**, 163106 (2006)

(Castro Neto 2009) A H Castro Neto *et al.*, "The electronic properties of graphene", *Rev. Mod. Phys.* **81**, 109 (2009)

(Chigarev 2008) N Chigarev *et al.*, "Laser generation and detection of longitudinal and shear acoustic waves in a diamond anvil cell", *Appl. Phys. Letts.* **93**, 181905 (2008)

(Chandrachud 2010) P Chandrachud *et al.* "A systematic study of electronic structure from graphene to *graphane*", *J. Phys.: Condens. Mat.* **22**, 465502 (2010)

(Cruikshank 1976) D P Cruikshank, C B Pilcher & D Morrison, "Pluto: Evidence for Methane Frost", *Science* **194**, 835 (1976)

(de Heer 2007) W A de Heer *et al.*, "Epitaxial graphene", *Solid State Commun.* **143**, 92 (2007)

(Dean 2013) C R Dean *et al.*, "Hofstadter's butterfly and the fractal quantum Hall effect in moiré superlattices", *Nature* **497**, 598 (2013)

(Demirbas 2007) A Demirbas, "Progress and recent trends in biofuels", *Prog. Energ. Combust.* **33**, 1 (2008)

(Ding 2010) F Ding *et al.*, "Stretchable Graphene: A Close Look at Fundamental Parameters through Biaxial Straining", *Nano Lett.* **10**, 3453 (2010)

(Dubrovinskaia 2010) N Dubrovinskaia *et al.*, "Diamond as a high pressure gauge up to 2.7 Mbar", *Appl. Phys. Lett.* **97**, 251903 (2010)

(Dubrovinsky 2012) L Dubrovinsky *et al.*, "Implementation of micro-ball nanodiamond for high-pressure studies above 6 Mbar", *Nat. Commun.* **3**, 1163 (2012)

(Dubrovinsky 2015) L Dubrovinsky *et al.*, "The most incompressible metal osmium at static pressures above 750 gigapascals", *Nature* **525**, 226 (2015)

(Eigler 2013) S Eigler *et al.*, "Wet Chemical Synthesis of Graphene", *Adv. Mater.* **25**, 3583 (2013)

(Elias 2009) D C Elias *et al.*, "Control of Graphene's Properties by Reversible Hydrogenation: Evidence for Graphane", *Science* **323**, 610 (2009)

(Eng 2013) A Y S Eng *et al.*, "Searching for Magnetism in Hydrogenated Graphene: Using Highly Hydrogenated Graphene Prepared *via* Birch Reduction of Graphite Oxides", *ACS Nano* **7**, 5930 (2013)

(Errandonea 2004) D Errandonea *et al.*, "Pressure-induced α → ω transition in titanium metal: a systematic study of the effects of uniaxial stress", *Physica B* **355**, 116 (2004)

(Fasolino 2007) A Fasolino, J H Los & M I Katsnelson, "Intrinsic ripples in graphene", *Nat. Mater.* **6**, 858 (2007)

(Ferrari 2000) A C Ferrari & J Robertson, "Interpretation of Raman spectra of disordered and amorphous carbon", *Phys. Rev. B* **61**, 14095 (2000)

(Ferrari 2006) A C Ferrari *et al.* "Raman Spectrum of Graphene and Graphene Layers", *Phys. Rev. Lett.* **97**, 187401 (2006)

(Ferrari 2007) A C Ferrari, "Raman spectroscopy of graphene and graphite: Disorder, electron–phonon coupling, doping and nonadiabatic effects", *Solid State Commun.* **143**, 47 (2007)

(Ferrari 2013) A C Ferrari & D M Basko, "Raman spectroscopy as a versatile tool for studying properties of graphene", *Nat. Nanotechnol.* **8**, 235 (2013)

(Ferrari 2015) A C Ferrari *et al.*, "Science and technology roadmap for graphene, related two-dimensional crystals, and hybrid systems", *Nanoscale* **7**, 4587 (2015)

(Filintoglou 2013) K Filintoglou *et al.*, "Raman spectroscopy of graphene at high pressure: Effects of the substrate and pressure transmitting media", *Phys. Rev. B* **88**, 045418 (2013)

(Fischer 2006) H E Fischer, A C Barnes & P S Salmon, "Neutron and x-ray diffraction studies of liquids and glasses", *Rep. Prog. Phys.* **69**, 233 (2006)

(Flores 2009) M Z S Flores *et al.*, "Graphene to graphane: a theoretical study", *Nanotechnology* **20**, 465704 (2009)

(Frenkel 1946) J Frenkel, "Kinetic Theory of Liquids", Oxford University Press: Oxford, United Kingdom (1946)

(Fukuda 2001) H Fukuda, A Kondo & H Noda, "Biodiesel Fuel Production by Transesterification of Oils", *J. Biosci. Bioeng.* **92**, 405 (2001)

(Gao 2011) H Gao *et al.*, "Band Gap Tuning of Hydrogenated Graphene: H Coverage and Configuration Dependence", *J. Phys. Chem. C* **115**, 3236 (2011)

(Geim 2007) A K Geim & K S Novoselov, "The rise of graphene", *Nat. Mater.* **6**, 183 (2007)

(Geng 2015) D Geng, H Wang & G Yu, "Graphene Single Crystals: Size and Morphology Engineering", *Adv. Mater.* **27**, 2821 (2015)

(Goncharov 2005) A F Goncharov *et al.*, "Optical calibration of pressure sensors for high pressures and temperatures", *J. Appl. Phys.* **97**, 094917 (2005)

(Goncharov 2012) A F Goncharov, "Raman Spectroscopy at High Pressures", *International Journal of Spectroscopy* **2012**, 617528 (2012)

(Gordon 1972) A J Gordon & R A Ford, "The Chemist's Companion: A Handbook of Practical Data, Techniques and References", John Wiley & Sons: New York City, NY, USA (1972)

(Gorelli 2006) F Gorelli *et al.*, "Liquidlike Behavior of Supercritical Fluids", *Phys. Rev. Lett.* **97**, 245702 (2006)

(Graf 2007) D Graf *et al.*, "Spatially Resolved Raman Spectroscopy of Single- and Few-Layer Graphene", *Nano Lett.* **7**, 238 (2007)

(Gregoryanz 2004) E Gregoryanz *et al.*, "Synthesis and characterization of a binary noble metal nitride", *Nat. Mater.* **3**, 294 (2004)

(Grimsditch 1989) M Grimsditch, R Bhadra & L M Torell, "Shear Waves through the Glass-Liquid Transformation", *Phys. Rev. Lett.* **62**, 2616 (1989)

(Guillemette 2013) J Guillemette *et al.*, "Quantum Hall Effect in Hydrogenated Graphene", *Phys. Rev. Lett.* **110**, 176801 (2013)

(Guillemette 2014) J Guillemette, thesis entitled "Electronic Transport in Hydrogenated Graphene", McGill University, Montréal, QC, Canada (2014)

(Haberer 2010) D Haberer *et al.*, "Tunable Band Gap in Hydrogenated Quasi-Free-Standing Graphene", *Nano Lett.* **10**, 3360 (2010)

(Han 2007) M Y Han *et al.*, "Energy Band-Gap Engineering of Graphene Nanoribbons", *Phys. Rev. Lett.* **98**, 206805 (2007)

(Hanfland 1989) M Hanfland, H Beister & K Syassen, "Graphite under pressure: Equation of state and first-order Raman modes", *Phys. Rev. B* **39**, 12598 (1989)

(Hazen 1999) R M Hazen, "The Diamond Makers", Cambridge University Press: Cambridge, United Kingdom (1999)

(Hebert 1987) P Hebert *et al.*, "Optical studies of methane under high pressure", *Phys. Rev. B* **36**, 9196 (1987)

(Hess 1992) N J Hess & D Schiferl, "Comparisons of the pressure-induced frequency shift of Sm:YAG to the ruby and nitrogen vibron pressure scales from 6 to 820 K and 0 to 25 GPa and suggestions for the use as a high-temperature pressure calibrant", *J. Appl. Phys.* **71**, 2082 (1992)

(Hollas 1996) J M Hollas, "Modern Spectroscopy", John Wiley & Sons: Chichester, United Kingdom (1996)

(Howie 2013) R T Howie, thesis entitled "Optical Studies of Dense Hydrogen at Multi-Megabar Pressures", University of Edinburgh, Edinburgh, United Kingdom (2013)

(Howie 2015) R T Howie, P Dalladay-Simpson & E Gregoryanz, "Raman spectroscopy of hot hydrogen above 200 GPa", *Nat. Mater.* **14**, 495 (2015)

(Huang 2010) E-P Huang *et al.*, "High-temperature and pressure Raman spectroscopy of diamond", *Material Letters* **64**, 580 (2010)

(Ishigami 2007) M Ishigami *et al.*, "Atomic Structure of Graphene on SiO_2", *Nano Lett.* **7**, 1643 (2007)

(Jacobsen 2004) S D Jacobsen *et al.*, "Shear waves in the diamond-anvil cell reveal pressure-induced instability in (Mg,Fe)O", *Proc. Natl. Acad. Sci. U.S.A.* **101**, 5867 (2004)

(Jacobsen 2005) S D Jacobsen *et al.*, "Advances in High-Pressure Technology for Geophysical Applications, Chapter 2: Chapter 2 – A gigahertz ultrasonic interferometer for the diamond anvil cell and high-pressure elasticity of some iron-oxide minerals", Elsevier: Amsterdam, Netherlands (2005)

(Jiao 2009) L Jiao *et al.*, "Narrow graphene nanoribbons from carbon nanotubes", *Nature* **458**, 877 (2009)

(Johnson 2002) D A Johnson, "Metals and Chemical Change", Royal Society of Chemistry: Cambridge, United Kingdom (2002)

(Klotz 2009) S Klotz *et al.*, "Hydrostatic limits of 11 pressure transmitting media", *J. Phys. D: Appl. Phys.* **42**, 075413 (2009)

(Kobayashi 2013) T Kobayashi *et al.*, "Production of a 100-m-long high-quality graphene transparent conductive film by roll-to-roll chemical vapor deposition and transfer process", *Appl. Phys. Lett.* **102**, 023112 (2013)

(Kono 2013) Y Kono *et al.* "Toward comprehensive studies of liquids at high pressures and high temperatures: Combined structure, elastic wave velocity, and viscosity measurements in the Paris–Edinburgh cell", *Phys. Earth Planet. Inter.* **228**, 269 (2013)

(Krauss 2009) B Krauss *et al.*, "Laser-induced disassembly of a graphene single crystal into a nanocrystalline network", *Phys. Rev. B* **79**, 165428 (2009)

(Kuila 2011) T Kuila *et al.*, "Recent advances in graphene based biosensors", *Biosens. Bioelectron.* **26**, 4637 (2011)

(Kunc 2003) K Kunc, I Loa & K Syassen, "Equation of state and phonon frequency calculations of diamond at high pressures", *Phys. Rev. B* **68**, 094107 (2003)

(Kvashin 2014) A G Kvashin *et al.*, "Phase Diagram of Quasi-Two-Dimensional Carbon, From Graphene to Diamond", *Nano Lett.* **14**, 676 (2014)

(Lacam 1980) A Lacam, M Madon & J P Poirer, "Olivine glass and spinel formed in a laser heated diamond-anvil high pressure cell", *Nature* **288**, 155 (1980)

(Lee 2008) C Lee *et al.*, "Measurement of the Elastic Properties and Intrinsic Strength of Monolayer Graphene", *Science* **321**, 385 (2008)

(Leenaerts 2010) O Leenaerts *et al.*, "First-principles investigation of graphene fluoride and graphane", *Phys. Rev. B* **82**, 195436 (2010)

(Lemal 2004) D M Lemal, "Perspective on fluorocarbon chemistry", *J. Org. Chem.* **69**, 1 (2004)

(Lenz-Solomun 1994) P Lenz-Solomun, M-C Wu & D W Goodman, "Methane coupling at low temperatures on Ru(001) and Ru(1120) catalysts", *Catal. Letts.* **25**, 75 (1994)

(Levchenko 2010) I Levchenko *et al.*, "The large-scale production of graphene flakes using magnetically-enhanced arc discharge between carbon electrodes", *Carbon* **48**, 4556 (2010)

(Li 2011) B Li *et al.*, "Photochemical Chlorination of Graphene", *ACS Nano* **5**, 5957 (2011)

(Linstrom 2011) P J Linstrom & W G Mallard, "NIST Chemistry WebBook, NIST Standard Reference Database Number 69", National Institute of Standards and Technology, Gaithersburg, MD, USA, http://webbook.nist.gov (retrieved 19/12/2015) (2011)

(Liu 2011) N Liu *et al.*, "Universal Segregation Growth Approach to Wafer-Size Graphene from Non-Noble Metals", *Nano Lett.* **11**, 297 (2011)

(Loveday 2001) J S Loveday *et al.*, "Stable methane hydrate above 2 GPa and the source of Titan's atmospheric methane", *Nature* **410**, 661 (2001)

(Lucchese 2010) M M Lucchese *et al.*, "Quantifying ion-induced defects and Raman relaxation length in graphene", *Carbon* **48**, 1592 (2010)

(Luo 2009) Z Luo *et al.*, "Thickness-Dependent Reversible Hydrogenation of Graphene Layers", *ACS Nano* **3**, 1781 (2009)

(Maiman 1960) T H Maiman, "Stimulated Optical Radiation in Ruby", *Nature* **187**, 493 (1960)

(Mao 1976) H-K Mao & P M Bell, "High-Pressure Physics: The 1-Megabar Mark on the Ruby R_1 Static Pressure Scale", *Science* **191**, 851 (1976)

(Mao 1979) H-K Mao & P-M Bell, "Observations of Hydrogen at Room Temperature (25°C) and High Pressure (to 500 Kilobars)", *Science* **203**, 1004 (1979)

(Mao 1986) H K Mao, J Xu & P M Bell, "Calibration of the Ruby Pressure Gauge to 800 kbar Under Quasi-Hydrostatic Conditions", *J. Geophys. Res.: Solid Earth* **91**, 4673 (1986)

(Matis 2012) B R Matis *et al.*, "Surface Doping and Band Gap Tunability in Hydrogenated Graphene", *ACS Nano* **6**, 17 (2012)

(Mattevi 2011) C Mattevi, H Kim & M Chhowalla, "A review of chemical vapour deposition of graphene on copper", *J. Mater. Chem.* **21**, 3324 (2011)

(Maxwell 1875) J C Maxwell, "On the Dynamical Evidence of the Molecular Constitution of Bodies", *Nature* **11**, 357 (1875)

(McMahon 2015) M I McMahon, "Diamonds on Diamond: structural studies at extreme conditions on the Diamond Light Source", *Phil. Trans. R. Soc. A* **373**, 20130158 (2015)

(Meyer 2007) J C Meyer *et al.*, "The structure of suspended graphene sheets", *Nature* **446**, 60 (2007)

(Mezouar 2005) M Mezouar *et al.*, "Development of a new state-of-the-art beamline optimized for monochromatic single-crystal and powder X-ray diffraction under extreme conditions at the ESRF", *J. Synchrotron Radiat.* **12**, 659 (2005)

(Mildren 2013) R P Mildren & J R Rabeau, "Optical Engineering in Diamond", Wiley-VCH: Weinheim, Germany (2013)

(Mohiuddin 2009) T M G Mohiuddin *et al.*, "Uniaxial strain in graphene by Raman spectroscopy: *G* peak splitting, Grüneisen parameters, and sample orientation", *Phys. Rev. B* **79**, 205433 (2009)

(Moore 1983) W J Moore, "Basic Physical Chemistry", Prentice-Hall, Inc.: Englewood Cliffs, NJ, United States of America (1983)

(Morard 2011) G Morard *et al.*, "High efficiency multichannel collimator for structural studies of liquids and low-Z materials at high pressures and temperatures", *Rev. Sci. Instrum.* **82**, 023904 (2011)

(Nair 2008) R R Nair *et al.*, "Fine Structure Constant Defines Visual Transparency of Graphene", *Science* **320**, 1308 (2008)

(Nair 2010) R R Nair *et al.*, "Fluorographene: A Two-Dimensional Counterpart to Teflon", *Small* **6**, 2877 (2010)

(Ni 2008) Z H Ni *et al.*, "Raman spectroscopy of epitaxial graphene on a SiC substrate", *Phys. Rev. B.* **77**, 115416 (2008)

(Nicolle 2011) J Nicolle *et al.*, "Pressure-Mediated Doping in Graphene", *Nano Lett.* **11**, 3564 (2011)

(Novoselov 2004) K S Novoselov *et al.*, "Electic Field Effect in Atomically Thin Carbon Films", *Science* **306**, 666 (2004)

(Novoselov 2005) K S Novoselov *et al.*, "Two-dimensional gas of massless Dirac fermions in graphene", *Nature* **438**, 197 (2005)

(Novoselov 2007) K S Novoselov *et al.*, "Room-Temperature Quantum Hall Effect in Graphene", *Science* **315**, 1379 (2007)

(Novoselov 2009) K S Novoselov, "Beyond the wonder material", *Physics World* **22**(August), 27 (2009)

(Novoselov 2012) K S Novoselov *et al.*, "A roadmap for graphene", *Nature* **490**, 192 (2012)

(Owen 2005) T Owen, "Planetary science: Huygens rediscovers Titan", *Nature* **438**, 756 (2005)

(Palasyuk 2014) T Palasyuk *et al.*, "Ammonia as a case study for the spontaneous ionization of a simple hydrogen-bonded compound", *Nat. Commun.* **5**, 3460 (2014)

(Pei 2012) S Pei & H-M Cheng, "The reduction of graphene oxide", *Carbon* **50**, 3210 (2012)

(Petitgirard 2015) S Petitgirard *et al.*, "Fate of $MgSiO_3$ melts at core–mantle boundary conditions", *Proc. Natl. Acad. Sci. U.S.A.* **112**, 14186 (2015)

(Piermarini 1973) G J Piermarini, S Block & J D Barnett, "Hydrostatic limits in liquids and solids up to 100 kbar", *J. Appl. Phys.* **44**, 5377 (1973)

(Piermarini 1975) G J Piermarini *et al.* "Calibration of the pressure dependence of the R_1 ruby fluorescence line to 195 kbar", *J. Appl. Phys.* **46**, 2774 (1975)

(Piscanec 2007) S Piscanec *et al.*, "Optical phonons of graphene and nanotubes", *Eur. Phys. J. Special Topics* **148**, 159 (2007)

(Polian 2003) A Polian, "Brillouin scattering at high pressure: an overview", *J. Raman Specrosc.* **34**, 633 (2003)

(Potts 2011) J R Potts *et al.*, "Graphene-based polymer nanocomposites", *Polymer* **52**, 5 (2011)

(Prescher 2015) C Prescher & V B Prakapenka, "*DIOPTAS*: a program for reduction of two-dimensional X-ray diffraction data and data exploration", *High Pressure Res.* **35**, 223 (2015)

(Proctor 2009) J E Proctor *et al.*, "High-pressure Raman Spectroscopy of Graphene", *Phys. Rev. B* **80**, 073408 (2009)

(Pumera 2013) M Pumera & C H A Wong, "Graphane and hydrogenated graphene", *Chem. Soc. Rev.* **42**, 5987 (2013)

(Ragan 1992) D D Ragan, R Gustavsen & D Schiferl, "Calibration of the ruby R_1 and R_2 fluorescence shifts as a function of temperature from 0 to 600 K", *J. Appl. Phys.* **72**, 5539 (1992)

(Reich 2004) S Reich & C Thomsen, "Raman spectroscopy of graphite", *Phil. Trans. R. Soc. Lond. A* **362**, 2271 (2004)

(Rekhi 1999) S Rekhi, L Dubrovinsky & S Saxena, "Temperature-induced ruby fluorescence shifts up to a pressure of 15 GPa in an externally heated diamond anvil cell", *High Temp. – High Pres.* **31**, 299 (1999)

(Regueiro 1992) M N Regueiro, P Monceau & J-L Hodeau, "Crushing C_{60} to diamond at room temperature", *Nature* **355**, 237 (1992)

(Riikonen 2013) J Riikonen *et al.*, "Photo-Thermal Chemical Vapor Deposition of Graphene on Copper", *Carbon* **62**, 43 (2013)

(Saito 2004) R Saito, G Dresselhaus & M Dresselhaus, "Physical Properties of Carbon Nanotubes", Imperial College Press: London, United Kingdom (2004)

(Savini 2010) G Savini, A C Ferrari & F Giustino, "First-Principles Prediction of Doped Graphane as a High-Temperature Electron-Phonon Superconductor", *Phys. Rev. Lett.* **105**, 037002 (2010)

(Scheler 2013) T Scheler *et al.*, "High-Pressure Synthesis and Characterization of Iridium Trihydride", *Phys. Rev. Lett.* **111**, 215503 (2013)

(Schmidt 1991) S C Schmidt *et al.*, "Calibration of the nitrogen vibron pressure scale for use at high temperatures and pressures", *J. Appl. Phys.* **69**, 2793 (1991)

(Sessi 2009) P Sessi *et al.*, "Patterning Graphene at the Nanometer Scale via Hydrogen Desorption", *Nano Lett.* **9**, 4343 (2009)

(Sidorov 2005) V A Sidorov & R A Sadykov, "Hydrostatic limits of Fluorinert liquids used for neutron and transport studies at high pressure", *J. Phys. Cond. Mat.* **17**, S3005 (2005)

(Simeoni 2010) G G Simeoni *et al.*, "TheWidom line as the crossover between liquid-like and gas-like behaviour in supercritical fluids", *Nat. Phys.* **6**, 503 (2010)

(Sofer 2015) Z Sofer *et al.*, "Fluorographane $(C_1H_xF_{1-x-\delta})_n$: synthesis and properties", *Chem. Commun.* **51**, 5633 (2015)

(Sofo 2007) J O Sofo, A S Chaudhari & G D Barber, "Graphane: A two-dimensional hydrocarbon", *Phys. Rev. B* **75**, 153401 (2007)

(Subrahmanyam 2009) K S Subrahmanyam *et al.*, "Simple Method of Preparing Graphene Flakes by an Arc-Discharge Method", *J. Phys. Chem. C* **113**, 4257 (2009)

(Subramaniam 1997) B Subramaniam, R A Rajewski & K Snavely, "Pharmaceutical Processing with Supercritical Carbon Dioxide", *J. Pharm. Sci.* **86**, 885 (1997)

(Trachenko 2013) K Trachenko & V V Brazhkin, "Duality of liquids", *Sci. Rep.* **3**, 2188 (2013)

(Trachenko 2014) K Trachenko, V V Brazhkin & D Bolmatov, "Dynamic transition of supercritical hydrogen: Defining the boundary between interior and atmosphere in gas giants", *Phys. Rev. E* **89**, 032126 (2014)

(Trots 2013) D M Trots *et al.*, "The Sm:YAG primary fluorescence pressure scale", *J. Geophys. Res.: Solid Earth* **118**, 5805 (2013)

(Tsu 1978) R Tsu, J González H & I Hernández C, "Observation of splitting of the E_{2g} mode and two-phonon spectrum in graphites", *Solid State Commun.* **27**, 507 (1978)

(Tuinstra 1970) F Tuinstra & J L Koenig, "Raman Spectrum of Graphite", *J. Chem. Phys.* **35**, 1126 (1970)

(Unarunotai 2009) S Unarunotai *et al.*, "Transfer of graphene layers grown on SiC wafers to other substrates and their integration into field effect transistors", *Appl. Phys. Lett.* **95**, 202101 (2009)

(Vidano 1981) R P Vidano *et al.*, "Observation of Raman band shifting with excitation wavelength for carbons and graphites", *Solid State Commun.* **39**, 341 (1981)

(Vos 1991) W L Vos & J A Schouten, "On the temperature correction of the ruby pressure scale", *J. Appl. Phys.* **69**, 6744 (1991)

(Wada 1980) N Wada, P J Gaczi & S A Solin, ""Diamond-like" 3-fold coordinated amorphous carbon", *J. Non-Cryst. Solids* **35-36**, 543 (1980)

(Wallace 1947) P R Wallace, "The Band Theory of Graphite", *Phys. Rev.* **71**, 622 (1947)

(Wang 1990) Y Wang, D C Alsmeyer & R L McReery, "Raman Spectroscopy of Carbon Materials: Structural Basis of Observed Spectra", *Chem. Mater.* **2**, 557 (1990)

(Wang 2008) H Wang *et al.*, "Vibrational properties of graphene and graphene layers", *J. Raman. Spectrosc.* **40**, 1791 (2008)

(Wang 2010) Y Wang *et al.*, "Toward High Throughput Interconvertible Graphane-to-Graphene Growth and Patterning", *ACS Nano* **4**, 6146 (2010)

(Weck 2013) G Weck *et al.*, "Use of a multichannel collimator for structural investigation of low-Z dense liquids in a diamond anvil cell: Validation on fluid H_2 up to 5 GPa", *Rev. Sci. Instrum.* **84**, 063901 (2013)

(Wei 2011) Q Wei, N Dubrovinskaia & L Dubrovinsky, "Ruby and Sm:YAG fluorescence pressure gauges up to 120 GPa and 700 K", *J. Appl. Phys.* **110**, 043513 (2011)

(Wen 2011) X-D Wen *et al.*, "Graphane sheets and crystals under pressure", *Proc. Natl. Acad. Sci. U.S.A.* **108**, 6833 (2011)

(Wright 1984) I P Wright, "Ices in the Solar System", *Nature* **308**, 692 (1984)

(Xiang 2010) H J Xiang *et al.*, "Thermodynamically stable single-side hydrogenated graphene", *Phys. Rev. B* **82**, 165425 (2010)

(Xu 2005) L Xu *et al.*, "Relation between the Widom line and the dynamic crossover in systems with a liquid–liquid phase transition", *Proc. Natl. Acad. Sci. U.S.A.* **102**, 16558 (2005)

(Yang 2012) Z Yang, "Birch Reduction of Graphite. Edge and Interior Functionalization by Hydrogen", *J Am. Chem. Soc.* **134**, 18689 (2012)

(Yang 2013) K Yang *et al.*, "Nano-graphene in biomedicine: theranostic applications", *Chem. Soc. Rev.* **42**, 530 (2013)

(Yang 2015) C Yang *et al.*, "Frenkel line and solubility maximum in supercritical fluids", *Phys. Rev. E* **91**, 012112 (2015)

(Zan 2012) R Zan *et al.*, "Scanning tunnelling microscopy of suspended graphene", *Nanoscale* **4**, 3065 (2012)

(Zhang 2006) G Zhang *et al.*, "Hydrogenation and Hydrocarbonation and Etching of Single-Walled Carbon Nanotubes", *J. Am. Chem. Soc.* **128**, 6026 (2006)

(Zhang 2015) C Zhang, *et al.*, "Direct growth of large-area graphene and boron nitride heterostructures by a co-segregation method", *Nat. Commun.* **6**, 6519 (2015)

(Zhao 1998) Y Zhao *et al.*, "Pressure measurement at high temperature using ten Sm:YAG fluorescence peaks", *J. Appl. Phys.* **84**, 4049 (1998)

(Zhou 2013) H Zhou *et al.*, "Chemical vapour deposition growth of large single crystals of monolayer and bilayer graphene", *Nat. Commun.* **4**, 2096 (2013)